Université de Montréal

Fonctionnalisation de transistors à effet de champ à base de graphène : vers l'assemblage d'une interface de détection biologique contrôlée

par

Anouk Béraud

Département de physique
Faculté des arts et des sciences

Mémoire présenté en vue de l'obtention du grade de
Maître ès sciences (M.Sc.)
en Physique

22 décembre 2021

Université de Montréal

Faculté des arts et des sciences

Ce mémoire intitulé

Fonctionnalisation de transistors à effet de champ à base de graphène : vers l'assemblage d'une interface de détection biologique contrôlée

présenté par

Anouk Béraud

a été évalué par un jury composé des personnes suivantes :

Normand Mousseau
(président-rapporteur)

Delphine Bouilly
(directeur de recherche)

Andrea Bianchi
(membre du jury)

Résumé

Les capteurs biologiques basés sur l'électronique nanométrique ont la propriété intéressante d'être à l'échelle des molécules étudiées. Plus spécifiquement, grâce à leurs propriétés électroniques exceptionnelles, les transistors à effet de champ à base de graphène (TECG) permettent des mesures électriques locales à grandes vitesses d'acquisition et sur de longues durées, offrant un cadre idéal pour la biodétection et l'étude de la cinétique moléculaire. Le présent mémoire traite de l'analyse, la mesure et la fonctionnalisation des TECG dans l'optique d'en faire des biocapteurs performants. En introduction, nous décrirons les propriétés électroniques du graphène ainsi que les principaux concepts reliés aux transistors de graphène et à la détection biologique. Puis, nous établirons les trois objectifs qui seront élaborés en autant de chapitres. Dans le premier chapitre, nous présenterons une revue de littérature critique qui cible l'analyse statistique et l'assemblage de l'interface de détection comme facteurs déterminants de la performance à l'aide d'analyses originales et d'une description approfondie de l'état du domaine. Dans le deuxième chapitre, nous présenterons des ajustements concrets aux sysèmes expérimentaux basés sur les recommandations émises dans la revue. D'abord, nous améliorons la productivité de la fabrication des transistors, puis développons une instrumentation permettant de mesurer plusieurs capteurs en parallèle. Dans le troisième chapitre, nous prendrons avantage de ces modifications pour présenter dans le deuxième article une méthode permettant une fonctionnalisation du graphène à la fois contrôlée et solide. En utilisant le voltage de grille, nous initions et suspendons la fonctionnalisation covalente du graphène aux sels de diazonium afin d'obtenir le taux de greffage désiré, tout en observant la réaction en temps-réel. Ainsi, par nos avancées méthodologiques et d'instrumentation, nous résolvons un enjeu critique du développement de la chimie de surface, centrale à la performance de biodétection.

Mots-clés : Nanotechnologie, transistors à effet de champ, graphène, biodétection

Abstract

Nanoscale electronics are a promising tool for biosensing as they fit their target's size and allow for local, fast-paced measurements over long time scales. Because of their exceptional electronic properties, graphene field-effect transistors (GFETs) are excellent candidates for biosensing and studying molecular kinetics. This work discusses the analysis, measurement, and functionalization of GFETs as optimized biosensors. In the introduction, we describe the electronic properties of graphene and the main concepts related to GFETs and biodetection. We also establish the three aims of the project, elaborated in three chapters. The first chapter contains a critical literature review that uses original analyses and a thorough state-of-the-field to target statistical analysis and the biorecognition interface assembly as determining factors in sensing performance. In the second chapter, we present the practical adjustments to the experimental systems based on the review's recommendations. First, we increase the productivity of device fabrication, then we develop a multiplexed electrical measurement setup. In the third chapter, we take advantage of these modifications to present in the second article a method for stable and controlled functionalization. Using the gate voltage, we start and stop the covalent functionalization of graphene with aryldiazonium salts to get the desired grafting level, while observing the reaction in real-time. Thus, with our advances in methodology and instrumentation, we solve a critical aspect of surface chemistry, central for biodetection performance.

Keywords: Nanotechnology, field-effect transistors, graphene, biosensing

Table des matières

Liste des tableaux

Table des figures

Liste des sigles et des abréviations

A	Amplitude du bruit
ADN	Acide désoxyribonucléique
AFM	*Atomic Force Microscopy*
AFP	*Alpha-fetoprotein*
AI	*Analog input*
AO	*Analog output*
AuNps	*Gold nanoparticles*
BBDT	4-bromobenzène diazonium tétrafluoroborate
bioFET	*Biological field-effect transistor*
BSA	*Bovine serum albumine*
CBDT	4-carboxybenzène diazonium tétrafluoroborate

CEA	*Carcoembryonic antigen*
C_g	Capacitance de la grille
CNP	*Charge neutrality point*
CNT	*Carbon nanotube*
CNTFET	*Carbon nanotube field-effect transistor*
C_q	Capacité quantique
CVD	*Chemical vapor deposition*
ΔN	Variation de la concentration d'analyte
ΔX	Variation d'une métrique électrique
D	Drain
DAQ	*Data acquisition module*
dCAS9	*Deactivated CRISPR associated protein 9*
DNA	*Desoxyribonucleic acid*

dsDNA	*Double-stranded DNA*
e	Charge de l'électron
ϵ	Permittivité électrique du médium
ϵ_{ox}	Permittivité électrique du diélectrique
EDL	*Electrical double layer*
f	Fréquence
FET	*Field-effect transistor*
γ	Paramètre expérimental
G	Grille/*Gate*
g_e	Transconductance des électrons
GFET	*Graphene field-effect transistor*
g_h	Transconductance des trous
g_m	Transconductance du graphène

hCG	*Human chorionic gonadotropin*
HCG	*Hepatocellular carcinoma*
HMDS	Hexaméthyldisilane
I	Force ionique de la solution
I_D	Courant moyen ou Intensité de la bande D du spectre Raman
I_{ds}/I_{sd}	Courant entre la source et le drain
IFN-γ	Cytokine Interféron-gamma
I_G	Intensité de la bande G du spectre Raman
IgE	*Human immunoglobulin*
I_{in}	Courant d'entrée
I_{PNC}/I_{CNP}	Courant au point de neutralité de charge
ISFET	*Ion sensitive field-effect transistor*
k_B	Constante de Boltzmann

L	Longueur de la chaine de conduction
λ_D	Longueur de Debye
LOD	*Limit of detection*
ME	*Mechanical exfoliation*
MEMS/NEMS	*Micro/nano-electrochemical systems*
MOSFET	*Metal oxide semiconductor field-effect transistor*
n	Densité des porteurs de charge
N_A	Nombre d'Avogadro
nt	Nucléotide
PA	*Protective antigen*
PB	*Phosphate buffer*
PBASE	*Pyrenebutanoic acid succinimidyl ester*
PBS	*Phosphate buffer saline*

PCR	*Polymerase chain reaction*
PDMS	Polydiméthylsiloxane
PEG	Polyéthylène glycol
PMMA	Poly (méthylméthacrylate)
PNA	*Peptide nucleic acid*
PNC	Point de neutralité de charge
PSA	*Prostate specific antigen*
PXI	*PCI extension for instrumentation*
q	Charge des porteurs de charge
QDs	*Quantum dots*
R_{ds}/R_{sd}	Résistance entre la source et le drain
R_f	Résistance finale d'amplification
rGO	*Reduced graphene oxide*

RNA	*Ribonucleic acid*
S	Source ou Sensitivité
SEM	*Scanning electron microscopy*
S_I	Densité spectrale de puissance
Si-NWFET	*Silicon nanowire field-effect transistor*
SMU	*Source measurement unit*
SNP	*Single nucleotide polymorphism*
ssDNA	*Single-stranded DNA*
STM	*Scanning tunneling microscopy*
t	Épaisseur de l'oxide
T	Température
TBAF	Tetrabutylammonium hexafluorophosphate
TEC	Transistor à effet de champ

TECG	Transistor à effet de champ à base de graphène
μ	Mobilité des porteurs de charge
v	Vitesse des porteurs de charge
V_G	Voltage à la grille
V_{out}	Voltage de sortie
V_{PNC}/V_{CNP}	Voltage au point de neutralité de charge
V_{sd}/V_{ds}	Voltage entre la source et le drain
W	Largeur de la chaine de conduction
XPS	*X-ray photoelectron spectrometry*

Remerciements

Je commence bien sûr par remercier ma directrice de recherche, Delphine Bouilly. Brillante et bienveillante, elle aura été pour moi une mentore et un modèle. Merci pour tout le temps dévoué à mes projets, pour toutes nos discussions, pour ce soucis du détail qui sait faire de nous des meilleures scientifiques. Surtout, merci d'avoir eu plus confiance en moi que moi, j'en avais besoin.

Je tiens également à remercier mes collègues : Claudia M. Bazán, Madline Sauvage et Amira Bencherif. Claudia, merci pour ta patience, ta douceur et tes habiletés à construire des PCB incroyables. Amira, merci pour tout le temps passé à me former en fab. Même si rien ne marchait à l'époque, on aura bien rigolé. Madline, merci pour les apéros, pour les grandes discussions et juste d'être toi en général. Merci du fond du coeur aussi à Christophe Clément et Marie-Hélène Bernier pour leur aide en salle de fabrication, j'ai adoré travailler avec vous.

Merci tout particulier à mes parents, Agnès Connat et Frank Béraud. Je suis vraiment fière d'être votre fille, merci pour votre support infini. Merci aussi à ma petite soeur Marie Béraud, que j'aime de tout mon coeur, qui m'a tellement aidée cette année.

Aucun merci ne semble suffisant pour mes amies-douces, Clémentine Barberger et Nadia Sanders. Vous êtes tout ce qu'il y a de plus beau et je vous aime au complet. Même chose pour Élisa Roy-Rivard, Raphaëlle Bélanger, Sophie Dallaire et Alana Thibodeau-Antonacci.

Introduction

Les transistors à effet de champ à base de graphène (TECG) se distinguent des transistors traditionnels, notamment par leur étroite interaction avec l'environnement [1]. Bien qu'elle compromette leur avenir dans l'électronique conventionnelle, cette propriété assure aux TECG une popularité grandissante comme capteurs biologiques.

Un capteur biologique est un dispositif pouvant convertir une réponse biologique en signal électrique, électrochimique, optique, gravimétrique ou acoustique par un processus de transduction [2]. Ce type de technologie fait l'objet de grands efforts de recherche grâce à son potentiel d'application dans plusieurs domaines tels la biomédecine [3], les sciences de l'environnement [4] ou la santé publique [5]. De tous les types de capteurs biologiques, les TECG attirent particulièrement l'attention pour la recherche sur le cancer [6-10], dont la détection de très faibles concentrations de biomarqueurs est un enjeu de taille [11]. En effet, les TECG peuvent être utilisés comme biocapteurs analytiques, où des molécules biologiques, dites sondes, interagissent spécifiquement avec une très faible quantité de molécules d'intérêt à la cancérologie, dites cibles. Grâce à la grande sensibilité du graphène aux fluctuations électrostatiques locales de son environnement immédiat et à la haute mobilité de ses porteurs de charge, son utilisation comme transducteur pourrait réduire la concentration de molécules cibles à des niveaux inégalés.

À l'interface entre le semi-conducteur et le métal, le graphène a été découvert expérimentalement par Geim et Novoselov en 2004 [12], ce qui leur méritera un prix Nobel en 2010. Ses propriétés électroniques hors du commun ont fait couler beaucoup d'encre, mais en font surtout un candidat prometteur dans la quête de détecteurs biologiques ultra-sensibles. Toutefois, il reste un certain nombre de défis à relever avant d'obtenir des TECG parfaitement fonctionnels. Entre autres, nommons la capture efficace des signaux de bioreconnaissance, l'augmentation de la performance de détection et la miniaturisation des dispositifs [2].

C'est dans ce contexte que le laboratoire de Delphine Bouilly se spécialise dans la conception, la fabrication et l'analyse de nanobiocapteurs au sein de l'Institut de recherche en immunologie et cancérologie (IRIC). La présente étude vise à établir les bases nécessaires à l'obtention de biocapteurs performants via l'assemblage contrôlé de l'interface de détection biologique. Plus précisément, le travail effectué dans ce mémoire propose une analyse approfondie et un développement expérimental menant à la maîtrise de la fonctionnalisation covalente de transistors à effet de champ à base de graphène. Nous commencerons par introduire les principaux concepts théoriques utiles à la compréhension des différents éléments du mémoire. Dans les chapitres subséquents, nous tenteront de répondre aux trois objectifs suivants :

Disséquer les éléments clés de la conception et de l'opération des transistors comme capteurs bioanalytiques afin d'en extraire les meilleures pratiques et d'en optimiser la performance. Au deuxième chapitre, nous présentons une revue de littérature critique dans laquelle nous soutenons que l'analyse statistique de tout résultat est une pratique nécessaire afin d'outrepasser les fréquentes fluctuations électroniques du graphène au contact de son environnement. Nous identifions grâce à des analyses originales et approfondies que la conception de l'interface de détection biologique, plus particulièrement la chimie de surface, est le paramètre le plus important dans l'optimisation de la performance des capteurs.

Créer des systèmes expérimentaux propice à l'étude des TECG. Afin de pouvoir présenter un ensemble statistique significatif lors de nos expériences, la première partie du troisième chapitre discute de la fabrication optimisée d'un grand nombre de capteurs. La deuxième partie aborde la conception, la construction et l'analyse de performance d'un système de mesures électriques permettant l'opération simultanée de plusieurs capteurs en parallèle. Cette instrumentation permet aussi de produire des séries temporelles de grande qualité.

Contrôler la fonctionnalisation covalente du graphène. La fonctionnalisation est un aspect critique du développement de la chimie de surface nécessaire à la biodétection, et la fonctionnalisation covalente est une approche prometteuse par sa solidité. Or, elle est à la fois peu comprise et peu contrôlée. L'article du quatrième chapitre présente une méthode innovatrice prenant avantage de nos outils et de notre méthodologie pour moduler et suivre la fonctionnalisation covalente du graphène aux sels de diazonium par électro-greffage.

Chapitre 1

Concepts théoriques

1.1. Propriétés électroniques du graphène

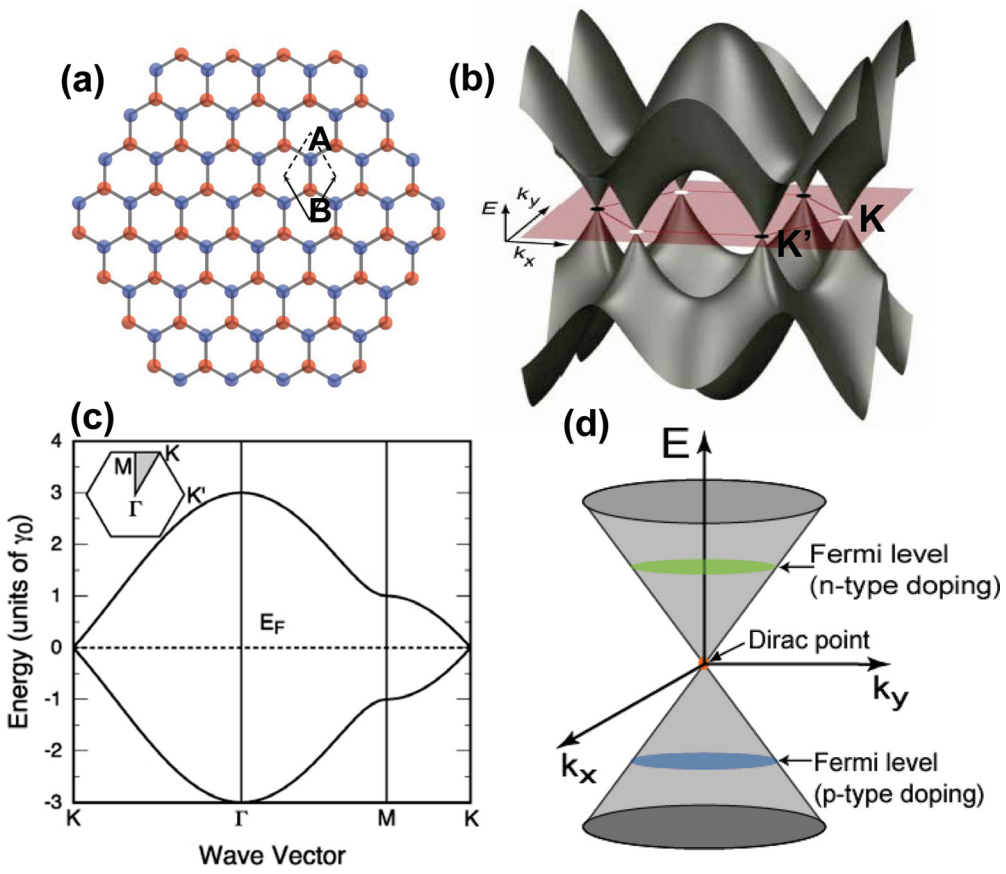

Figure 1.1 – (a) Structure hexagonale en alvéoles du graphène avec deux atomes par cellule unitaire. (b) Structure de bande en 3D. (c) Dispersion électronique du graphène. (d) Approximation de la structure de bandes à basse énergie comme deux cônes se touchant au point de Dirac. La position du niveau de Fermi détermine la nature du dopage et des porteurs de charge. Reproduit avec la permission de [13]. ©2010, American Chemical Society.

Le graphène est composé d'atomes de carbones disposés en une structure hexagonale dont la cellule primitive contient deux atomes, tel qu'illustré à la Figure 1.1a. Le carbone possède quatre électrons de valence répartis en une orbitale $2s$ et trois orbitales p ($2p_x$, $2p_y$ et $2p_z$). Dans la conformation alvéolaire du graphène, les orbitales $2s$, $2p_x$ et $2p_y$ s'hybrident avec les orbitales des atomes voisins pour former une structure sp^2 trigonale orientée dans le plan xy. Ces orbitales, aussi appelées σ, sont responsable de la robustesse du réseau [14]. Les quatrièmes électrons de valence (orbitales $2p_z$, perpendiculaires au plan) se délocalisent et forment avec les atomes avoisinants une orbitale nommée π autour de la monocouche d'atomes [13]. La flexibilité de la liaison π confère une plus grande mobilité aux électrons que ceux dans une liaison σ, ils sont donc responsables de la conduction électrique du graphène.

La structure cristalline extrêmement simple du graphène mène à une structure de bandes unique présentée à la Figure 1.1b, calculée pour la première fois en 1947 par Wallace grâce à un modèle de liaisons fortes [13, 15]. La bande de valence (ou bande π) touche ponctuellement la bande de conduction (ou bande π^*) aux six points K de la zone de Brillouin, appelés points de Dirac, ou points de neutralité de charge (PNC). La double propriété d'une densité d'états nulle à la surface de Fermi et d'une absence de bande interdite (voir Figure 1.1c) fait du graphène un intéressant intermédiaire entre semi-conducteur et métal, qu'on appelle souvent un semi-métal. Comme on peut le voir à la Figure 1.1c, la dispersion électronique au point K est linéaire dans un régime de basse énergie, auquel on se limitera dans les travaux présentés dans ce mémoire. À ce point, les bandes forment un cône caractéristique appelé cône de Dirac, dont l'approximation est présentée à la Figure 1.1d. Cette forme atypique résulte de l'interaction des électrons avec ce potentiel périodique à la structure si particulière. En effet, les porteurs de charge peuvent être décrits dans ce régime par l'équation de Dirac et interprétés comme des quasi-particules fermioniques relativistes sans masse de repos [16], dont la mobilité peut atteindre des vitesses dites balistiques pouvant aller jusqu'à 15 000 $\mathrm{cm^2V^{-1}s^{-1}}$ dans des conditions ambiantes [17]. Une autre qualité du graphène est l'ambipolarité de son effet de champ électrique due à la symétrie de sa dispersion [16]. Ceci implique que les porteurs de charges peuvent être modulés continuellement entre trous et électrons en contrôlant le niveau de Fermi, dont la position détermine à la fois le type de porteur de charge et sa concentration. Grâce à la faible densité d'état du graphène à l'énergie de Fermi, on peut facilement la modifier en appliquant un champ électrique externe au graphène [18]. La modulation du niveau de Fermi est appelée le dopage.

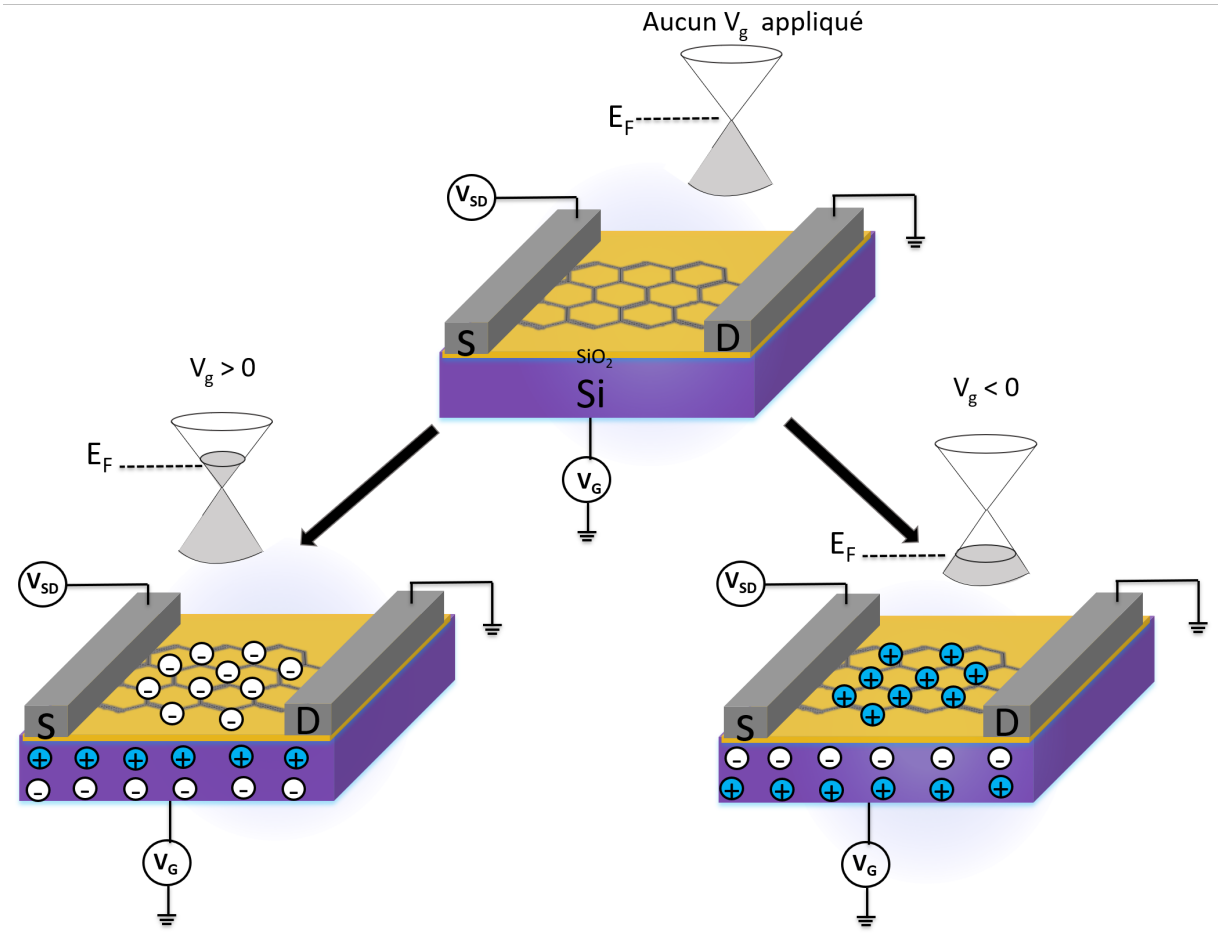

Figure 1.2 – Schématisation idéalisée du fonctionnement des transistors à effet de champ à base de graphène. Quand le voltage de grille est positif, le niveau de Fermi est dans la bande de conduction et les porteurs de charge majoritaires dans le graphène sont des électrons. Quand le voltage est négatif, le niveau de Fermi est dans la bande de valence et les porteurs de charge majoritaires sont des trous.

1.2. Transistors de graphène

Le dopage par l'application d'un champ électrique se retrouve au coeur des principes fondamentaux de l'utilisation des TECG. Notons que bien que certaines généralités de leur fonctionnement soient exposées dans ce chapitre, plus de détails ainsi que leur composition et leur utilisation seront donnés dans la revue de littérature du chapitre 2.

Un transistor est un dispositif électronique servant à amplifier ou à moduler du courant électrique [19]. Les transistors de graphène font partie d'une catégorie de transistors dits à effet de champ (TEC), découverte plus de dix ans après les premiers transistors bipolaires. De nos jours, les TEC dominent l'électronique moderne [20]. Plus particulièrement, les TECG ont une structure s'apparentant à une sous-catégorie appelée *MOSFET* (*Metal Oxide*

Semiconductor Field-Effect Transistors). Les *MOSFET* sont composés d'une électrode de grille (métal) en contact avec un diélectrique (oxide), d'électrodes de sources et de drain entre lesquelles se forme une chaine de conduction, ainsi que d'un substrat composé d'un semi-conducteur dopé (silicium) [20]. Dans le cas du TECG, la configuration varie légèrement, avec la chaine de conduction de graphène, déposé sur l'oxide et le silicium dopé positivement (voir Figure 1.2). La grille peut être le silicium lui-même, ou une autre grille métallique dont la configuration peut varier (voir le prochain chapitre).

Le principe général de fonctionnement des TECG est schématisé à la Figure 1.2. Deux différences de potentiel sont appliquées : une entre les électrodes de source et de drain (V_{ds}) qui permet au courant de circuler dans la chaine de conduction et une à la grille (V_g). Le V_{ds} est d'une petite amplitude ne suffisant pas à délocaliser les électrons π du graphène, mais crée une différence de potentiel entre les électrodes suffisante pour engendrer un courant lorsque les porteurs de charge sont libérés par la grille. En effet, dans sa configuration au repos (sans l'application d'un voltage de grille), le niveau de Fermi du graphène est localisé au point de Dirac, comme observé dans le transistor du haut du schéma. On n'a donc pas de charge libre, ni de courant. Lorsqu'on applique le voltage de grille, on modifie la concentration de porteurs de charge dans la chaine de conduction. Les charges se déplacent alors dans le sens de la différence de potentiel entre la source et le drain, ce qui crée le courant. On peut expliquer la libération des porteurs de charge dans le graphène de plusieurs façons. En utilisant un formalisme de transmission [21], on dit que les électrons sont libérés d'un réservoir thermique en équilibre à travers une barrière d'énergie potentielle dont la hauteur est modulée par le voltage de la grille et que les charges sont réorganisées par électrostatique afin de maintenir la neutralité dans le dispositif [22]. Avec un formalisme quantique, on dit plutôt que l'application d'un voltage de grille engendre un décalage du niveau de Fermi dépendant du voltage, de la différence entre les fonctions de travail de l'électrode et du graphène ainsi que du type et de l'épaisseur du diélectrique utilisé [18, 23]. Peu importe le formalisme choisi, on observera expérimentalement que le courant dans le graphène est modulé par le voltage de grille.

À la différence d'un transistor de silicium, les TECG ne possèdent pas de courant *ON/OFF* très défini. Lorsqu'il est balayé en fonction du voltage de grille, le courant exhibe plutôt un minimum de conductivité ponctuel lorsque le niveau de Fermi est aligné au point de neutralité de charge [1], ce qu'on illustre dans la Figure 1.3. Dans le panneau du haut, on montre la bande de valence en rouge et la bande de conduction en violet, avec le point de neutralité de charge à l'endroit où les deux bandes se touchent. Dans le panneau du bas, on présente une courbe de transfert caractéristique d'un TECG. Cette mesure caractéristique consiste à balayer le voltage de grille d'une valeur négative à positive et à mesurer le courant

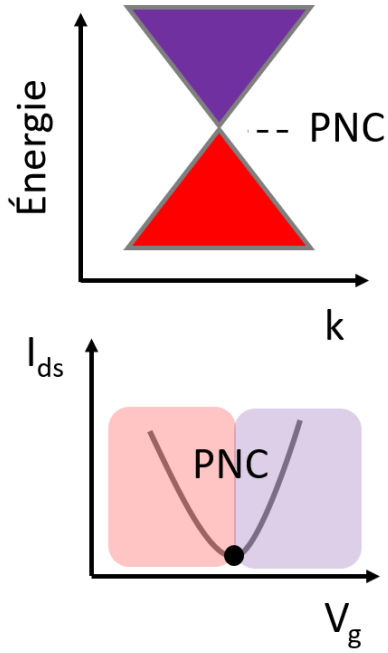

Figure 1.3 – Diagramme de bande schématisé et courbe de transfert caractéristique d'un TECG. La section rouge représente la bande de valence, la section violette la bande de conduction et PNC, le point de neutralité de charge.

entre la source et le drain. En modifiant le voltage de la grille, on module le niveau de Fermi selon le principe élaboré précédemment. À des voltages négatifs (en rouge), on se trouve dans la bande de conduction et les porteurs de charge majoritaires sont les trous. Quand le niveau de Fermi atteint le point de neutralité de charge, on arrive au minimum de conductivité, souvent appelé point de Dirac ou tout simplement PNC. À des voltages positifs (mauve), on entre dans la bande de conduction et le courant est porté par des électrons.

1.3. Détection biologique

L'absence de bande interdite du graphène est un enjeu pour l'utilisation des TECG dans l'électronique traditionnelle, mais ne l'est pas pour la détection biologique qui nous intéresse dans le présent mémoire. Au contraire, ce minimum de conductivité caractéristique sera d'une grande utilité puisqu'il sera utilisé comme métrique de détection (voir chapitre 2). La détection biologique avec des transistors de graphène consiste à étudier les interactions entre une molécule-cible et une molécule-sonde par l'entremise des modulations du courant électrique du transistor. Les cibles et les sondes sont des molécules biologiques interagissant

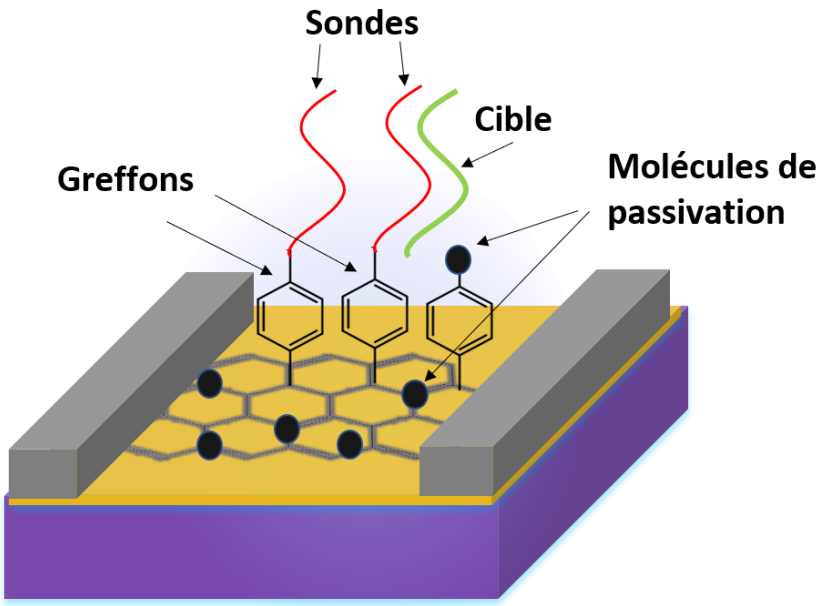

Figure 1.4 – Schématisation d'un transistor de graphène utilisé pour faire de la biodétection. Des molécules intermédiaires (greffons) relient des sondes au graphène afin qu'elles interagissent avec des cibles. Des molécules de passivation empêchent les cibles d'interagir non-spécifiquement avec le graphène ou les greffons.

spécifiquement ensemble, par exemple deux brins d'ADN complémentaires [24, 25] ou un anticorps et son antigène [26, 27]. Tel qu'établi à la section précédente, le graphène est sensible à son environnement électrique et l'interaction spécifique entre la cible et la sonde engendre une réorganisation des charges pouvant être détectée par diverses métriques qui seront établies au prochain chapitre.

L'interface de détection biologique est ce qui distingue le simple transistor du biocapteur. La Figure 1.4 en illustre les principales composantes : le graphène, les greffons de fonctionnalisation, les sondes, les cibles et les molécules de passivation. La fonctionnalisation permet d'attacher les sondes au graphène alors que les molécules de passivation empêchent les interactions non-spécifiques entre les cibles et le graphène ou entre les cibles et les greffons. La fonctionnalisation est un thème central de ce mémoire, c'est pourquoi nous nous y attarderons davantage ici.

La fonctionnalisation de la surface du graphène est la première étape de l'assemblage de l'interface. Le procédé consiste à ajouter des atomes ou des molécules à la structure du

graphène afin d'en modifier certaines propriétés. La fonctionnalisation a plusieurs utilités. Par exemple, on l'a utilisée pour ouvrir une bande d'énergie interdite au niveau de Fermi dans l'esprit de la quête vers l'électronique post-silicium [28]. Dans le cas qui nous intéresse, l'ajout de greffons permet l'immobilisation du graphène à des molécules biologiques, qui seront utilisées comme sondes lors de détections. Dans la Figure 1.4, les greffons fonctionnalisant le graphène sont des groupement aryles comme ceux qui seront étudiés au chapitre 4. Il existe deux types de fonctionnalisation du graphène :

- La fonctionnalisation non-covalente : cette voie est basée principalement sur des interactions π-π avec des molécules aromatiques possédant un système π assez fort ou sur des interactions de van der Walls avec des molécules organiques ou des polymères hydrophobes [29]. Bien que les greffons agissent comme des centres de diffusion pour les porteurs de charge, ce qui limite leur libre parcours moyen, et donc leur mobilité [30], ce type d'interaction ne perturbe pas la structure du graphène, qui préserve alors ses propriétés électroniques. Les désavantages principaux de la fonctionnalisation non-covalente sont qu'elle est difficile à caractériser, assez difficile à contrôler et moins stable que son analogue covalente.
- La fonctionnalisation covalente : cette approche requiert la formation de liens covalents entre les greffons et les atomes de carbone, ce qui change leur hybridation de sp^2 à sp^3. Ce processus est donc équivalent à une addition de défauts au réseau menant à la modification de la structure de bande et des propriétés électroniques du graphène [31]. La stabilité des orbitales π délocalisées assure une bonne stabilité chimique du plan basal du graphène, ce qui explique que la fonctionnalisation covalente soit généralement faite avec des espèces chimiques très réactives, comme les sels d'aryldiazonium [32]. Ce type de chimie et ses effets sur les propriétés du graphène seront expliqués plus en détails au chapitre 4. De manière générale, l'approche covalente est plus stable, plus reproductible et plus versatile que son homologue non-covalent. Toutefois, son plus grand désavantage réside dans la perte de conductivité associée au changement d'hybridation des carbones. De nombreux efforts sont déployés pour limiter les inconvénients de la méthode afin de pouvoir profiter des avantages, qui sont particulièrement attrayants pour la biodétection [33]. Un exemple concret sera présenté au chapitre 4.

Chapitre 2

Revue de littérature critique

La détection biologique avec des TECG est fondamentalement multidisciplinaire puisqu'elle se trouve à l'intersection de la physique, de la chimie, de l'électronique et de la biologie. Elle peut être étudiée sous l'angle de chacune de ces disciplines, ce qui en fait un sujet riche, mais dont le formalisme et les pratiques peuvent sembler désordonnés. Le présent chapitre propose une revue de littérature critique visant à la fois à décrire et à analyser les différents aspects de la conception, de l'opération et de la performance des biocapteurs. Ce travail particulièrement axé sur la mesure électrique initie une réflexion globale sur l'optimisation de l'utilisation des TECG comme biocapteurs analytiques.

Contributions d'Anouk Béraud (auteure principale) : recensement et analyse de 84 articles scientifiques, analyse de l'effet de différents paramètres sur la performance de détection des biocapteurs, formulation des grandes conclusions de l'analyse de littérature et construction la structure de l'article, rédaction des sections *Electrical measurements and metrics* et *Performance assessment* (à l'exception de la section *Spatial range of detection*, écrite par Monique Tie) et la conceptualisation des figures, réalisées en collaboration avec Claudia M. Bazán.

Contributions des co-auteures : Madline Sauvage, Claudia M. Bazán et Amira Bencherif ont participé à l'écriture de la section *Design and fabrication*. Madline Sauvage a contribué à l'identification de paramètres pertinents en lien avec la détection d'ADN, ainsi qu'à l'inventaire de ces paramètres dans plusieurs articles. Monique Tie a participé aux réflexions de la section *Performance assessment*. Delphine Bouilly est responsable de la supervision globale de l'article. Elle a participé activement à l'élaboration du contenu, a effectué la relecture, ainsi que la réécriture finale de toutes les sections.

Note : Les informations supplémentaires de cet article (*Electronic Supporting Information*) sont présentées à l'Annexe A.

Graphene Field-Effect Transistors as Bioanalytical Sensors : Design, Operation and Performance

Anouk Béraud[1,2], Madline Sauvage[1,3], Claudia M. Bazán[1], Monique Tie[1,3], Amira Bencherif[1,4] et Delphine Bouilly[1,2]

1- Institut de recherche en immunologie et cancérologie, Université de Montréal, Montréal, Canada.
2- Département de Physique, Faculté des arts et des sciences, Université de Montréal, Montréal, Canada.
3- Département de chimie, Faculté des arts et des sciences, Université de Montréal, Montréal, Canada.
4- Institut d'ingénierie biomédicale, Faculté de médecine, Université de Montréal, Montréal, Canada.

RÉSUMÉ. Les transistors à effet de champ à base de graphène émergent dans le paysage technologique comme de prometteurs capteurs bioanalytiques. La variation de leur conductance électrique est utilisée pour performer l'analyses de biomolécules pertinentes, comme de l'ADN, des protéines, des ions et des petites molécules. Cette revue de littérature propose une évaluation détaillée des approches rapportées à la conception, l'opération et la performance des transistors de graphène utilisés comme biosenseurs. Nous commençons par disséquer les éléments clés de la conception de ces dispositifs, parallèlement aux approches les plus communes pour sa fabrication. Nous comparons les modes possibles d'opération, incluant les courbes de transfert, les courbes de sortie et les séries temporelles, en plus de l'intégration en temps-réel, ou dans des protocoles *a posteriori*. Finalement, nous révisons les métriques de performance rapportées pour la détection et la quantification d'analytes biologiques et discutons des limites et des meilleures pratiques pour optimiser l'utilisation des transistors à effet de champ à base de graphène comme des senseurs bioanalytiques.
Mots-clés : Biosenseur, bioanalytique, nanotechnologie, graphène, transistors à effet de champ

ABSTRACT. Graphene field-effect transistors (GFETs) are emerging as bioanalytical sensors, in which their responsive electrical conductance is used to perform quantitative analyses of biologically-relevant molecules such as DNA, proteins, ions and small molecules. This review provides a detailed evaluation of reported approaches in the design, operation and performance assessment of GFET biosensors. We first dissect key design elements of these devices, along with most common approaches for their fabrication. We compare possible modes of operation of GFETs as sensors, including transfer curves, output curves and time series as well as their integration in real-time or *a posteriori* protocols. Finally, we review performance metrics reported for the detection and quantification of bioanalytes, and discuss limitations and best practices to optimize the use of GFETs as bioanalytical sensors.
Keywords : Biosensor, bioanalytics, nanotechnology, graphene, field-effect transistors

Cet article a été publié dans Analyst, Royal Society of Chemistry et sélectionné dans la catégorie *Analyst Hot Articles* [34].

2.1. Introduction

Bioanalytical sensors, engineered at the interface between physics, chemistry, biology and nanotechnology, are a class of instruments designed for quantitative analyses of biologically-relevant molecules (ex. nucleic acids, proteins, metabolites, drugs, etc.). Such biosensors have numerous applications in a variety of areas including biomedicine [3, 35], environmental monitoring [4, 36] and public health [5, 37]. Analyte detection and transduction into signal can be mediated by different mechanisms, including optical, electrochemical, electrical or mechanical. In the past decades, advances in the field of nanotechnology have catalyzed remarkable innovation in these different subclasses of bioanalytics sensors, especially through the discovery and production of new nanomaterials. For example, gold nanoparticles (AuNPs) and inorganic quantum dots (QDs) have been used in the design of ultrasensitive electrochemical [38] and optical [39] biosensors. Materials engineering at the nanoscale has enabled artificial nanopores in solid-state membranes (e.g. Si_3N_4 membrane, SiO_2, SiC and Al_2O_3 films) capable of registering the translocation of individual DNA molecules [40]. Nanocarbon materials such as carbon nanotubes (CNTs) and graphene have also stimulated improvements in optical [41, 42], electrochemical [43, 44] as well as in MEMS/NEMS (micro/nanoelectromechanical systems) bioanalytical sensors [45].

A specific class of nanomaterial-enabled bioanalytical sensors are field-effect transistors (FETs). In FET biosensors, or bioFETs, the interaction with biological analytes is transduced as a change in the electrical conductance of the sensor. The use of FETs for bioanalytical sensing purposes first appeared around 1980, usually adapted from ion-sensitive field-effect transistors (ISFETs) made for pH sensing [46]. For example, Caras and Janata [47] introduced a penicilin-sensitive bioFET assembled by immobilizing specific enzymes on the surface of an ISFET. Early FET sensors were made using traditional semiconductors (e.g. Si) and oxides (e.g. Ta_2O_5 or Al_2O_3), and were often limited in sensitivity due to their low surface-to-bulk ratio. The discovery of low-dimensional semiconductors with extremely high surface-to-bulk ratios prompted the design of various highly-sensitive FET sensors for the detection of ions and molecules [48, 49]. Among these, silicon nanowire FETs (Si-NWFETs) and carbon nanotube FETs (CNTFETs) have both been extensively demonstrated as bioanalytical sensors [50-52] and even ultimately miniaturized into single-molecule FETs with biomolecules [53-55]. Despite good sensing performance, the development of 1D-FETs remains hindered today by practical challenges in the synthesis, manipulation and scalable integration of 1D nanomaterials. On the other hand, 2D semiconductor nanomaterials also benefit from extreme surface-to-bulk ratio but are much more compatible with established microfabrication processes. While a plethora of van der Waals materials have been discovered in the past few years [56, 57], graphene is by far the most available and well-studied specimen among them. Since the isolation of individual graphene sheets from graphite by Novoselov and Geim in 2004 [12], graphene has received much attention for its exciting mechanical, thermal and optoelectronic properties [58]. In particular, graphene was found to exhibit extremely high charge carrier mobility, as well as remarkable sensitivity to electrostatic changes in its near environment [59, 60], making it a promising material for sensing applications.

In this review, we focus specifically on graphene field-effect transistors (GFETs) as bioanalytical sensor. GFETs have been demonstrated as sensors in physics and chemistry, for instance as photodetectors [61], gas sensors (e.g. NO_2, NH_3, H_2O) [62, 63] or pH sensors [64, 65]. More recently, GFETs have been introduced as biosensors : for instance, Mohanty *et al.*[66] reported in 2008 a GFET biosensor able to detect the hybridization between a tethered single strand of DNA and its complementary sequence. Since then, intensive research has been focused on developing GFETs for biomolecular detection. In the bioanalytical field, GFETs have generated interest as ion sensitive field-effect transistors (ISFETs), especially for the detection of toxicology-relevant ions such as heavy metal ions (e.g. Hg^{2+}, Pb^{2+}) [67, 68]. They have also been shown to detect multiple biologically-relevant molecules such as glucose [69], various biomarkers for diseases including cancer [10, 70], DNA sequences with single-nucleotide mismatch specificity [71, 72], pathogens such as bacteria [73, 74] and viruses [75, 76], or drugs like opioids [77] or antibiotics [78]. GFETs are often described as having key advantages for biosensing applications, including easy operation, fast response [79], real-time monitoring [80-82], high specificity and sensitivity with detection limits down to the femtomolar [83, 84] and sub-femtomolar range [85-87], microfluidic integration [88-90] and multiplexing capability [25, 91, 92].

In recent years, there has been several reviews discussing the latest research on graphene and its applications as biosensors [93-98]. However, there is still a lack of a comprehensive review about GFETs focusing on key parameters for assessing their design, operation and performance, which is essential to progress towards the standardization of this technology and its uptake in industrial, commercial and/or clinical applications. Here we present a critical review of these three aspects of bioanalytical GFET sensors. We cover specifically experiments focusing on the detection of proteins, nucleic acids, bacteria, viruses, small molecules such as glucose, antibiotics or drugs, and heavy ions such as lead, mercury or potassium. We did not investigate pH sensors as they represent a whole field of study by themselves [99]. In the first part of this review, we briefly explain the fundamentals of GFET operation and review reported approaches for the design and fabrication of such devices. In the second part, we discuss and compare the possible modes of operation of GFETs for the detection and quantitation of bioanalytes. Finally, we review the state of performance metrics reported for this technology and discuss limitations and best practices to optimize the design and performance of GFETs as bioanalytical sensors.

The design of GFET sensors includes four key components : (1) a graphene layer responsible for the transport of electrical current and the transduction of biosensing events, (2) a set of at least three electrodes as required to operate a transistor, (3) a delivery system allowing tested samples to reach the graphene layer, and (4) a layer of biorecognition elements on the graphene surface allowing for the specific capture of targeted analytes. Figure 2.1a illustrates a typical layout for these elements. In the following, we review the role and design principles for each of them.

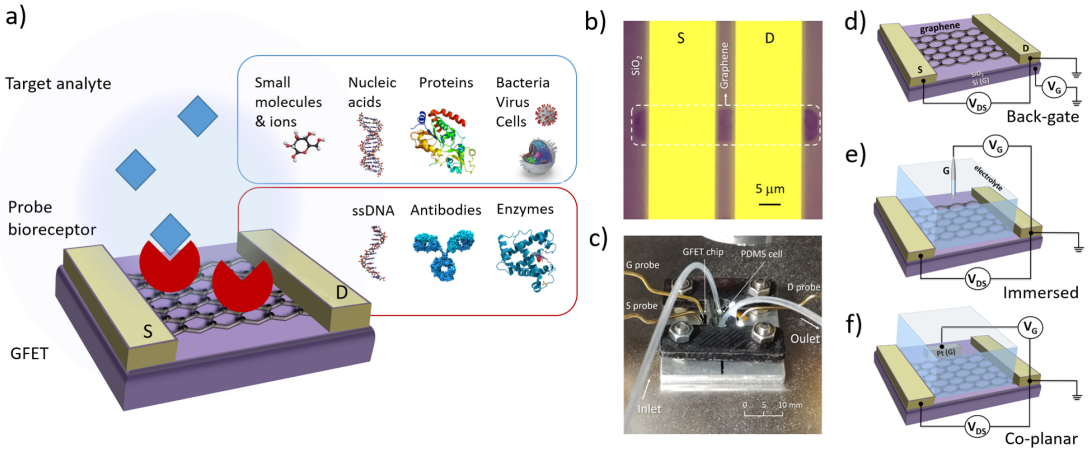

Figure 2.1 – Design elements of a GFET bioanalytical sensor. (a) Typical layout of a GFET sensor, showing a graphene layer functionalized with biorecognition elements (red) and immersed in a media containing the target analyte (blue). (b) The graphene is connected with source (S) and drain (D) electrodes to generate electrical current along the atomically-thin layer. (c) Example of packaging with electrical connections to the electrodes and a flow cell with inlet/outlet for sample delivery. The gate (G) electrode, which modulates the electrical conductance of graphene, can be assembled in a (b) back-gate, (c) immersed or (d) co-planar configuration.

2.2. Design and Fabrication

2.2.1. Graphene material

Graphene is an atomically-thin material made of a two-dimensional hexagonal lattice of carbon atoms. This structure, with each carbon atom sharing three of its four electrons in covalent bonds with its nearest neighbors (sp^2 bonds), is at the root of the robust mechanical properties of graphene [100]. At the same time, the remaining fourth electrons are delocalized over the two-dimensional lattice in a Π orbital responsible for most of the material's optoelectronic properties [101]. In the context of GFET sensors, we focus on the electrical and electrostatic properties of the material. Graphene is known for its extremely high mobility surpassing that of excellent metals [12, 102]. Being a semi-metal, its electrical conductance is moderately modulated by local electrostatic fields, allowing to operate the material in a field-effect transistor configuration. Because of this moderate ON-OFF modulation, graphene FETs are typically not considered competitive in pure electronics, compared to state-of-the-art 3D semiconductors such as silicon, or even to its 1D counterpart carbon nanotubes. However, their sensitive electrical conductance combined with their extremely high surface-to-bulk ratio provides them with significant advantages for chemical and biochemical sensing.

Graphene can be produced by several different methods before integration in a FET device. First, graphene can be exfoliated from graphite, a material formed of multiple stacked atomic

layers of graphene : the process consists in carefully extracting one monoatomic layer from the bulk graphite. Exfoliation can be achieved by various techniques, including chemical exfoliation[103], ball milling method [104], or more commonly micromechanical exfoliation, often referred as the "scotch-tape method" [104]. The scotch tape method was the first reported to isolate graphene [12], and typically provides the best electrical properties, including the highest mobilities and least density of defects [105]. However, it is difficult to obtain large-area flakes with exfoliation, which makes this approach less suitable for large-scale fabrication of devices [92]. Graphene can also be grown by chemical vapor deposition (CVD), most commonly on metallic substrates like Cu or Ni [106]. In this approach, a hydrocarbon precursor is introduced at high temperature, leading to graphene nucleation on the metal surface. Epitaxial growth on insulating SiC is also possible, in which case graphene nucleates following sublimation of the Si atoms [107]. Graphene grown by CVD is often favored in recent works [24, 85] because it is practical to generate large-area graphene layers, making it the best candidate for scalable GFET production. On the other hand, the mobility may be lower than in mechanically exfoliated graphene [108] and the transfer process following growth (see next Sec. 2.2.2) can damage the graphene and leave impurities [109]. Finally, another form of graphene is reduced graphene oxide (rGO), often used for its low cost and solution-processability [110]. To produce rGO, a strong oxidation solution is used to separate graphite layers into suspended graphene oxide flakes, which are then chemically reduced back into graphene [111]. The oxidation/reduction process tends to leave a high density of defects, which typically causes lower mobilities than in other types of graphene [112]. Independently of the type of graphene used, most GFET sensor studies report working with a single layer of graphene. Some specifically confirm the presence of a single layer with Raman spectroscopy [25, 109], as single-layer and few-layer graphene can be difficult to distinguish. Others use few-layers graphene [113], but single-layer has been reported to enhance the sensing performance [113].

2.2.2. Substrate and electrodes

In order to form a GFET device, graphene must be transferred on a planar substrate that provides physical support to the thin nanomaterial as well as to the electrodes and sample delivery system. The substrate, or at least its top layer, is normally made of a dielectric or other insulating material to avoid unwanted electrical connections between the different electrodes placed on its surface. The most popular substrate for GFETs is degenerately-doped Si covered with a layer of SiO_2 dielectric [9, 26, 77, 80, 84, 114], which is common in the field of electronics and enables the use of the lower layer as a gate electrode (see Fig. 2.1b). However, SiO_2 surfaces tend to trap charges and impurities, especially during the transfer process [115]. Other materials are investigated as substrates, for example sapphire on which graphene can be grown directly, leading to enhanced mobilities [109]. Research on more flexible and low-cost substrates is ongoing, for example with materials like flexible polyethylene terephthalate [76], silk fibroin [116] or paper [117].

Multiple techniques are used to place graphene on its operating substrate, depending on the graphene source. Graphene flakes obtained by mechanical exfoliation can be directly transferred on the substrate from the adhesive tape used for extraction, by stamping the tape on the target

substrate [118]. This straightforward method provides clean, uncontaminated graphene, but is typically incompatible with large-scale FET production. Graphene growth by CVD is done on metal substrates [106], then the graphene is transferred onto a dielectric substrate using either wet or dry transfer methods. In wet transfer, graphene is protected on one side with a soft polymer layer, typically polymetylmetacrylate (PMMA), and the metal substrate on the other side is dissolved in an etching solution. The protected graphene is then rinsed and picked up onto the target substrate [119]. Alternatively, protected graphene can be separated from the metal by electrochemical delamination [120, 121]. Dry transfer techniques include hot pressing and roll-to-roll methods based on thermal release tape (TRT) applied on the graphene [119]. Pick-up and stamping with PDMS can also be used for dry transfer of graphene [122]. In the case of rGO, the flakes can be transferred from solution onto the substrate of choice *via* a number of methods, such as drop-casting [71], dip coating [123] or vacuum filtration on a membrane which is then stamped on the substrate [124]. Graphene oxide flakes are either reduced before transfer, or first transferred and then reduced to rGO.

GFET design includes at least three electrodes, in order to operate as a field-effect transistor. The first two electrodes, called source (S) and drain (D), make direct contact with the graphene and enable the flow of electrical current in the graphene through the application of a difference of electrical potential between them. Source and drain electrodes are made of conductive material, typically a metal : most studies report using Au evaporated on top of a thin adhesion layer of Ti [113], Cr [125] or Ni [126]. Conductive silver paint can sometimes be used as the electrode material, especially on large area graphene [127]. The third electrode, called the gate (G), is placed in close proximity to the graphene but not in direct contact. A potential difference is applied between the gate and the drain (or source) to modulate the density and polarity of charge carriers in the graphene ; this mechanism is detailed in Sec. 2.3.1 on electrical transfer curves.

Multiple configurations have been used for the shape and position of the gate electrode : these can be classified in three main categories illustrated in Fig. 2.1b-d. The choice of gate configuration depends on the experimental protocol selected for analyte delivery and detection. When the sensor is operated in air or other gaseous atmosphere, a back-gate configuration is usually favored (Fig. 2.1b). In this layout, the conductive lower layer of the substrate acts as the gate electrode, separated from the graphene and drain-source electrodes by a dielectric layer. Most often, this configuration is achieved using degenerately-doped silicon covered by a layer of thermal silicon oxide. The dielectric thickness determines the capacitance of the gate electrode, as discussed in Sec. 2.3.1. In the case of SiO_2, its thickness can be as large as the order of a micrometer, or as thin as approximately $\sim$10-100 nm, this lower bound being to limit the occurrence of pinholes between the backgate and graphene. However, in biosensing experiments, GFETs are most often directly operated in an electrolyte solution. In such configuration, the gate voltage is applied using either a reference electrode immersed in the medium (Fig. 2.1c) or a coplanar electrode patterned on the substrate (Fig. 2.1d). Reference electrodes made of Ag/AgCl represent a common choice since their use in electrolyte buffer is well calibrated [128]. Others have reported immersed gate electrodes made of silver [71, 129, 130] or platinum [131] wires. Coplanar gate electrodes are patterned on the substrate in a similar approach as for source and drain electrodes, using deposition of metals such

as platinum [83], silver [132] or gold [76, 133, 134]. In both cases, the gate electrode is coupled with the graphene *via* an electrical double layer formed by the redistribution of ions in the electrolyte medium [135] ; this is discussed in more depth in Secs. 2.3.1 and 2.4.1. These gate configurations are frequently referred to as "top-gate" or "liquid-gate", but such terminology can be confused with solid-state planar electrodes placed on top of the graphene [136] and with gating using an ionic liquid [137], respectively. For configurations described here as in Figs. 2.1c-d, we recommend using "electrolytic" or "electrochemical" to qualify the gate electrode.

2.2.3. Analyte media and delivery

Biological analytes (nucleic acids, proteins, ions, drugs) are normally found in physiological samples (blood, serum, plasma, urine), *i.e.* complex solutions containing multiple species and specific salinity and pH conditions. In calibration and detection experiments using bioanalytical GFETs, a variety of media types are reported, with different levels of similarity with actual physiological conditions. The choice of media also influences GFET sensitivity and signal strength, especially by its degree of screening of electrostatic charges : this property of the medium is characterized by the Debye length, which is discussed in more details in Secs. 2.3.1 and 2.4.1. In the following, we review different media types used in GFET experiments, as well as delivery methods used to expose the graphene surface to analyte-containing samples.

The majority of reported GFET experiments are done in saline buffer, in which the purified target molecule is diluted at known concentrations [9, 71, 89, 127, 129]. This approach allows to calibrate quantitation curves over a controlled range of analyte concentrations, and the saline environment is necessary to maintain the proper conformation of macromolecules (nucleic acids and proteins). However, high salinity environments create increased screening, which can make detection by GFETs more challenging (see Sec. 2.4.1). In DNA detection, different saline buffers are reported ; the most common is phosphate buffer saline (PBS) either at its physiologically-equivalent 1X ionic strength (137 mM NaCl, 2.7 mM KCl, 4.3 mM Na_2HPO_4, 1.47 mM KH_2PO_4) [71, 134], or diluted at 0.1X [129] or 0.01X [81, 109]. Lower salinity enables longer screening distances, allowing to detect hybridization in parts of the sequence furthest from graphene, but if the ionic concentration is too low (for example in water), strand repulsion can destabilize the double helix conformation [72]. Other studies report using other buffers such as hybridization buffer (10 mM PB, 150 mM NaCl, 50 mM $MgCl_2$) [24], or 12.5 mM $MgCl_2$ and 30 mM Tris buffer, known to be equivalent to PBS 1X for DNA helix stabilization[72, 138]. Protein detection experiments also commonly use PBS [26, 89, 127, 133, 139, 140], and some groups have reported using 50 mM of PB [141] or 5 mM MES buffer [92]. Detection of *E. coli* bacteria was also shown in PBS buffer [110]. For the detection of ionic species, target ions are generally diluted with or without competing ions, either in aqueous solution [142-144], HEPES buffer [68], Tris-HCl buffer [126, 145], or PBS buffer [146].

Some GFET experiments have reported the detection of analytes in more complex biological samples. For example, An *et al.* [147] achieved the detection of mercury ions in real samples derived from mussels, and Weng *et al.* [145] tested blood samples from children for lead ions. Thakur *et al.* [74] detected the pathogen *E.coli* in river water samples. For proteins, Kim *et al.* [148]

captured the alpha-fetoprotein biomarker on the surface of GFETs by immersing directly in patient plasma, followed by electrical characterization in PBS after washing steps. Recently, Hajian *et al.* [83] demonstrated DNA detection directly in genomic DNA extracted and purified from cell culture and in human genomic samples, whereas Ganguli *et al.* [149] used loop-mediated isothermal amplification (LAMP) followed by detection of primer (ssDNA) on gFET sensors.

A few experiments completely evacuate the medium before electrical characterization. For example, Ping *et al.* [25] exposed GFETs with solutions of DNA before drying and performing electrical measurement. Similarly, Islam *et al.* [26] reported a back-gated GFET immunosensor for the detection of the human chorionic gonadotrophin (hCG) protein, in which the devices were exposed to probe and target in buffer solution followed by vacuum dry before characterization. In most experiments, however, measurements with GFETs are done directly in the analyte solution, which requires a method to contain the sample over graphene. The minimalist way to achieve this is by placing a droplet of sample on the GFET substrate to cover the graphene areas [150]. Most often, a reaction cell is secured on the GFET substrate, enabling containment and delivery of the sample. Due to the small sensing area of GFETs, such cells are frequently made to contain low sample volumes of the order of tens of microliters [69, 82, 89, 127, 134]. Because of their size, these are often referred to as microfluidic cells, although they do not necessarily use microscale flow control capabilities characteristic of microfluidic systems [151]. Polydimethylsiloxane (PDMS) is one of the most popular materials for cell fabrication due to its chemical inertness, mechanical flexibility, transparency, easy processing and low cost [151, 152]. GFETs integrated with a PDMS cell have been used for the detection of various targets such as proteins [89, 127, 148], DNA [91, 130, 134], viruses [27, 75, 76] and small molecules [69, 78]. Other cell materials have been reported, for example poly(methyl methacrylate) (PMMA) [81, 109] and silicon rubber [9]. The two most common cell designs used with GFET biosensors are the open cell and the flow cell : the first one consists of a simple top-open reservoir in which samples can be pipetted in and out [10, 69, 82, 93, 114, 130, 134, 148]. Flow cells generally consist of a small enclosed channel with tubing for sample inlet and outlet [78, 81, 89, 91, 92, 153], allowing minimized evaporation and mixing between samples, lower sample volumes (few μL) as well as controlled fluid flow. This minimizes the consumption of reagents and samples, and lessens signal perturbations such as commonly observed during the loading/emptying of open cells.

In recent years, integration of GFETs into advanced microfluidic systems has been proposed to create versatile lab-on-a-chip miniaturized platforms. In particular, integration of GFETs in multichannel microfluidics enables multiplexing, *i.e.* the ability to parallelize the detection of multiple targets in the same sample. Several studies have demonstrated multiplexed GFET analysis for protein [153] and DNA [81, 91, 134]. Microfluidics integration can also enable GFET measurements under stable flow, instead of in static media. For example, Xu *et al.* [81] quantified the kinetics and affinity of DNA hybridization using a high flow rate of 60 ml/min through the PMMA microfluidic channel. Similarly, Wang *et al.* [89] presented a GFET integrated with a PDMS microfluidic flow cell to study the binding kinetics and thermodynamic properties of human immunoglobulin E (IgE)

by means of time-resolved measurements performed under a flow rate of 5 μL/min. Temperature-dependent binding kinetics measurements were possible due to the closed flow cell enabling minimal sample evaporation. Measurements in flow mode also ensured a steady concentration of analyte available for binding, thus decreasing detection times [81, 88].

2.2.4. Surface functionalization and passivation

GFETs can be used as sensors because the electrical conductance of graphene is sensitive to electrostatic changes in its environment ; however the affinity between graphene and other molecules is not specific. For instance, graphene is known to interact with most proteins and nucleic acids, especially through hydrophobic domains of proteins [154] and either the backbone [155] or aromatic bases of nucleic acid [156]. To engineer specificity in GFET sensors, it is necessary to functionalize the graphene surface with molecules able to specifically recognize and capture the target analyte ; these biorecognition molecules are henceforward referred to as probe molecules. The coverage of graphene with probe molecules is often incomplete, in which case passivation strategies can be used to block non-specific interactions with graphene. In the following, we discuss the choice of probe molecules as well as strategies for probe immobilization and for passivation.

2.2.4.1. Probe molecules for biorecognition. Nucleic acid targets are typically detected via hybridization with their complementary sequence immobilized on the graphene surface. Most DNA hybridization studies directly use single-stranded DNA (ssDNA) as probes, with a nucleotide sequence complementary to that of the targeted DNA [24, 25, 85, 86, 93, 109, 129, 130, 134, 157, 158]. The length of ssDNA probes is generally comprised between 12 nt and 50 nt, in order to achieve sequence specificity while avoiding folding and formation of secondary structures in the probe. More complex probe designs have also been explored to improve sensitivity and sequence specificity, in particular to distinguish between single nucleotide polymorphisms (SNPs). For example, Cai *et al.* [71] reported high sensitivity using probes made of single-stranded peptide nucleic acid (PNA) which has a neutral backbone, in opposition to the negatively-charged backbone of DNA, thus enabling the minimization of electrostatic repulsion with the target DNA strand. Hwang *et al.* [72] demonstrated the detection of SNPs using probes based on strand displacement. In this design, probes were made of double-stranded DNA (dsDNA), with the tethered strand perfectly complementary to the target and the other weakly hybridized to the first ; the target sequence, when present in the sample, was shown to bind to the probe by displacing the weaker strand. Similarly, Gao *et al.* [85] demonstrated the use of hairpin-folded ssDNA as probe : unfolding of the hairpin was detected when binding the target. Finally, a recent study by Hajian *et al.* [83] used a single-guide RNA inserted in a deactivated CRISPR associated protein 9 (dCas9) to detect a target sequence in amplicons or within intact genomic DNA.

For protein detection, the most common strategy is the use of antibodies as probes, due to their high specificity and affinity for their antigen. For instance, GFETs functionalized with antibodies have been used to detect proteins identified as cancer biomarkers : Kim *et al.* [70] immobilized monoclonal antibodies against the prostate specific antigen (PSA) on a GFET biosensor, demonstrating highly sensitive detection of this biomarker of prostate cancer. In a similar way, monoclonal

antibodies on GFETs were used to detect alpha-fetoprotein (AFP), a biomarker of hepatocellular carcinoma (HCC), in patient plasma [148]. Other studies have used GFETs with antibody probes for biomarkers to other conditions, such as human Chorionic Gonadotrophin (hCG), a common pregnancy indicator [26]. Antibodies on GFETs have also been shown to detect surface proteins of bacteria [9, 74, 110] or viruses [75, 76, 159, 160]. For example, Chang *et al.* [110] and Thakur *et al.* [74] used anti-*E. coli* antibodies in order to detect the bacteria, and more recently Ono *et al.* [9] used IgG to immobilize the gastric pathogen *H. pylori* on GFETs. Similarly, Liu *et al.* [75] used specific antibodies to achieve rotavirus detection. Recently, GFETs with antibodies were also used to detect the SARS-CoV-2 virus responsible for COVID-19[159]. Antibody probes were also used for the detection of larger complexes such as exosomes [10] as well as small molecules such as the pesticide chlorpyrifos [84].

Aptamers are another type of probe molecules used in GFETs ; these are folded single-stranded DNA or RNA oligonucleotides that can bind a target protein or small molecule with high affinity and specificity. Saltzgaber *et al.* [92] functionalized graphene with aptamers designed to bind specifically to human thrombin proteins. Farid *et al.* [127] reported a GFET functionalized with aptamers for detection of the cytokine interferon-gamma (IFN-γ) associated with tuberculosis susceptibility. Recently, Wang *et al.* [89] studied the binding kinetics of human immunoglobulin E (IgE) to its specific aptamer, allowing the determination of thermodynamic properties of their interaction. In addition, the use of RNA aptamers has been reported for the detection of small molecules, such as the antibiotic tobramycin [78].

2.2.4.2. Strategies for probe immobilization. By far the most popular approach to immobilize probe molecules is through graphene functionalization with the linker molecule 1-pyrenebutanoic acid succinimidyl ester (PBASE) [9, 10, 24, 25, 71, 72, 76, 81, 85, 89, 92, 109, 114, 148, 150]. On one end, this molecule contains an aromatic pyrene group that binds to the graphene surface through non-covalent π-π interactions. The other end is made of a succinimidyl ester group, which is prone to form a covalent bond with amine groups via nucleophilic substitution [161]. Probes made of DNA are often immobilized with PBASE, usually *via* an amine-terminated modifier attached at the 3' or 5' extremity of the strand. This approach has been reported for simple ssDNA probes [25, 81, 109, 162], and also for more complex ssPNA probes [71, 150], hairpin-ssDNA probes [85] and dsDNA probes based on strand displacement [72], as described in the previous section. Aptamers can also be immobilized with the same approach [89, 92]. It should be noted that Kim *et al.* [133] reported the immobilization of ssDNA without terminal modifier via covalent coupling of the PBASE directly with the amine of nucleobases (adenine, cytosine, and guanine), and of dsDNA via non-covalent interactions between the phosphate groups in the DNA backbone and the succinimidyl ester moiety of PBASE. Instead of directly using PBASE, graphene can be functionalized with 1-pyrenebutyric acid, which is then activated using EDC/NHS chemistry into an NHS-ester [163]. In a different approach leading to the same construct, the pyrene moiety is sometimes directly functionalized to the ssDNA as a modifier to the 3' or 5' termination, and the pyrene-DNA complex is then linked to the graphene ; this approach was used in Farid *et al.* [127] to immobilize aptamer probes, and in Fu *et al.* [93] to immobilize ssDNA probe .

The PBASE approach is also frequently used to immobilize proteins, by covalently reacting the succinimidyl ester group with the amine-terminated residue of an amino acid (e.g. lysine) available at the surface of the protein. For instance, this approach was successfully applied to immobilize various antibodies [9, 148] as well as the dCas9 enzyme used for detection in genomic DNA in Hajian *et al.* [83]. Some groups use biotin-streptavidin as an intermediary to immobilize protein probes [9, 91] : for example in Ono *et al.* [9], amine sites on the urease probes are functionalized with biotin linkers which are then coupled to streptavidin molecules immobilized on graphene with PBASE. A common aspect of these approaches with proteins is that there are frequently multiple available amine sites on a protein, and thus targeting these provides little control on the orientation of the probe on the sensor surface. This distribution can actually be an advantage for sensing by positioning part of the target-binding sites closer to the graphene surface below the screening limit (see Sec. 2.4.1) [164].

Graphene can also be functionalized with covalent moieties, which can then be conjugated with biomolecules. A common reaction to do so is through the use of aryldiazonium salts, in which highly reactive radicals formed from reduced diazonium can directly bind to the carbon lattice of graphene[165]. The functionality of the aryl group is chosen for further bioconjugation with biomolecule probes : for instance, 4-carboxybenzenediazonium tetrafluoroborate (CBDT) creates stable carboxyphenyl anchor groups on the graphene surface. These –COOH moieties can then be activated using EDC-NHS chemistry into a stabilized NHS-ester ready for coupling to an amine group on the probe, as described with PBASE above. Lerner *et al.* [77] used this approach based on CBDT covalent functionalization followed by EDC-NHS reaction to immobilize an opioid receptor protein for naltrexone detection. Others have reported using the EDC-NHS reaction directly on carboxylated defects spontaneously present on the graphene material [141]. In a reverse configuration, the functionalization of graphene with primary amines ($–NH_2$) was shown using electron beam-generated plasmas produced in Ar/NH_3 ; amine-terminated ssDNA were coupled with the amine-functionalized graphene using glutaraldehyde as a bifunctional linker [166].

Covalent and non-covalent immobilization approaches have different impacts on GFET sensors. Covalent functionalization causes a significant structural change in graphene : it transforms the hybridization of carbon atoms at the functionalization site from sp^2 to sp^3. These point defects disrupt the conjugation of π electrons, and are known to alter the electronic properties of graphene, including its electrical conductance [167]. However, covalent moieties are extremely stable on the graphene surface [165], which can be useful for sensors used repeatedly or with high flow rates. On the other hand, non-covalent functionalization such as PBASE does not alter the structural integrity of graphene and therefore its electrical properties [29]. Hence, non-covalent functionalization, usually with PBASE, is largely favored for the immobilization of probe molecules on GFETs. Occasionally, some reports on GFET sensors use no graphene functionalization to immobilize the probes, for example by relying on non-specific interactions between DNA and the graphene [129, 134]. Other works have reported using metallic nanoparticles (such as Pt, Au) as intermediary between graphene and probes[74, 132, 168].

2.2.4.3. Strategies for passivation. Passivation of exposed surfaces of the sensor is important to avoid non-specific interactions with species other than the targeted analyte, particularly in complex biological samples such as clinical serum or plasma. One strategy broadly employed is the adsorption of a blocking agent during or after immobilization of the probes [169]. These molecules fill spaces between probe molecules, thus preventing other molecules to make contact with exposed graphene. Different blocking agents have been employed for such purpose, such as bovine serum albumin (BSA) [26, 84, 141, 148], polyethylene glycol (PEG) [85], or mixtures of BSA with Tween20, *i.e.* a nonionic surfactant made of polyoxyethylene (20) sorbitan monolaurate [169]. Following the coupling of probes with functionalized graphene, some functional groups of the linkers may also remain uncoupled, which can lead to undesirable coupling with non-targeted species. To avoid this, passive adsorption of glycine has been reported to terminate unreacted NHS groups on PBASE molecules [10]. Similarly, ethanolamine has been used to deactivate and block unbound carboxylic acid reactive groups on the graphene surface [81, 89]. In some sensor designs, the graphene is physically separated from the probes or sensing layer by a thin layer of dielectric, such as Al_2O_3 [74] or parylene [64]. This protects the graphene and its electrical characteristics, and prevents its direct contact with the sample media and the various molecules contained in it. Finally, GFET electrodes can also be passivated with dielectric films (e.g. SiO_2/SiN_X) either to block interaction with biomolecules and buffer solution, or to eliminate parasitic current [24].

2.3. Electrical measurements and metrics

FET-based sensors rely constitutively on electrical measurements, specifically measurements of the electrical current in the device channel – here the graphene layer (see Fig. 2.1). The general working principle of FET sensors is that the density of charge carriers in the channel (and hence the current) is modulated by the local electrostatic field, which is itself altered by physical or chemical changes in the environment around the channel. Alternate mechanisms to the field effect can include the generation of charge carriers (e.g. in photosensors) or changes in the scattering rates of charge carriers in the channel (e.g. due to increased disorder). In all cases, the detection principle of FET sensors is based on a change in electrical metrics induced by changes in the environment of the sensor. In FET biosensors, this principle is used to detect the capture of biomolecular species at the surface of the sensor. Graphene is a particularly good choice for FET sensors because its atomically-thin geometry makes its electrical conductance remarkably responsive to environmental effects, such as the capture or accumulation of biological analytes near the surface.

In practice, the electrical current of FETs is also controlled by voltages applied to the source, drain and gate electrodes (see Fig. 2.1). The potential applied between source and drain generates the flow of charge carriers along the channel, while the gate voltage modulates the electric field across the channel – and thus the charge carrier density contributing to the current. FET devices are characterized using three standard curves : transfer curves (current *vs.* gate bias), output curves (current *vs.* drain-source bias) and time series (current *vs.* time with fixed drain and gate voltages. In sensing applications, the effect of the analyte on such electrical curves can be monitored either

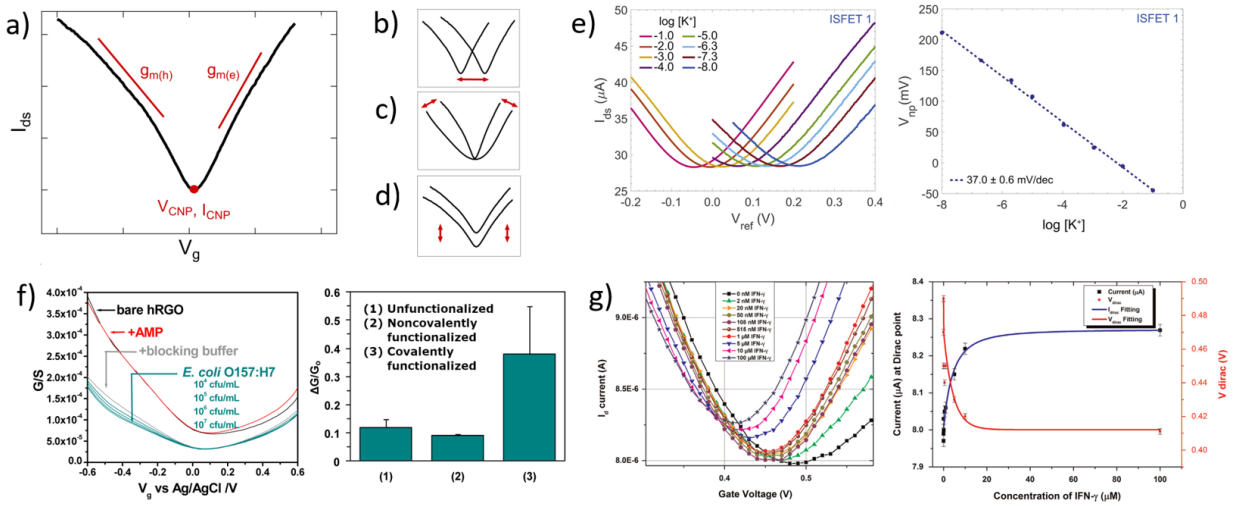

Figure 2.2 – Transfer curves in GFET bionalytical sensors. (a) Typical transfer curve $I_{ds}(V_g)$ of a GFET, illustrating key metrics in its use as a sensor : (b) change in the voltage of the charge neutrality point V_{CNP}, (c) change in the transconductance of electrons $g_{m(e)}$ or holes $g_{m(h)}$, and (d) change in the current amplitude, including at the charge neutrality point I_{CNP}. (e) Left : GFET experiment showing a lateral shift of the transfer curve upon exposure to increasing concentrations of its target analyte, here potassium cations. Right : Corresponding shift of V_{CNP} as a function of K^+ concentration. Reprinted with permission from Fakih *et al.* [143] © 2019 Elsevier B.V. (f) Left : Experiment with a GFET sensor for *E. coli*, showing a change of transconductance in the p-branch of the transfer curve upon increasing bacteria concentration. Right : Corresponding relative conductance change at fixed bias for different surface functionalization of the sensor. Adapted with permission from Chen *et al.* [105] © 2014 American Chemical Society. (g) Left : GFET experiment for detecting interferon-gamma protein (IFN-γ), showing a change in all three metrics with exposure to the protein. Right : Response of V_{CNP} and I_{CNP} as function of IFN-γ concentration. Reprinted with permission from Farid *et al.* [127] © 2015 Elsevier B.V.

a posteriori, by comparing a given metric before and after exposure to the sample, or in real-time by recording dynamic time series of the electrical current.

In this section, we examine specifically how GFET devices are electrically operated for bioanalytical sensing purposes. First, we review the characteristics of operating curves (transfer curves, output curves and time series) and the associated electrical metrics in GFETs. We then compare and discuss the use of these metrics for before-after or real-time detection of biological analytes.

2.3.1. Transfer curves

Transfer curves of transistors are obtained by sweeping the gate voltage V_g while maintaining a fixed bias V_{ds} between the source and drain electrodes. The resulting current I_{ds} (or resistance $R_{ds} = V_{ds}/I_{ds}$, or conductance $G_{ds} = I_{ds}/V_{ds}$) is plotted as a function of the gate bias. In GFETs, this plot typically results in a V-shaped curve, as illustrated in Fig. 2.2a. This shape translates an exchange in the polarity of the majority charge carriers in the graphene layer when sweeping the gate voltage : the left branch (or p-branch) represents an increasing density of positive charge carriers

(holes), while the right branch (or n-branch) represents negative charge carriers (electrons). Between the two branches, the density of charger carriers – and thus the current – reaches a minimum with equal populations of both positive and negative carriers, referred to as the Dirac point or charge neutrality point (CNP). The p- and n-branches extend linearly from the charge neutrality point such that

$$I_{ds} = g_m(V_g - V_{CNP}) \tag{2.1}$$

where V_{CNP} is the gate voltage at the charge neutrality point. The slope g_m is called the transconductance

$$g_m = \frac{W}{L}\mu C_g V_{ds} \tag{2.2}$$

which depends on the width W and length L of the graphene, μ the mobility of charge carriers and C_g the gate capacitance [170]. Transconductances for holes and electrons are not necessarily the same, in which case the transfer curve is asymmetrical.

Transfer curves can be obtained using any of the three gate electrode configurations described in Sec. 2.2.2 and illustrated in Fig. 2.1. The gate capacitance – and thus the transconductance – is highly dependent on this layout. In a back-gate configuration, the gate capacitance is dominated by that of the insulating layer separating graphene from the planar gate electrode, typically an oxide with a thickness t ranging from ∼10 nm to a few μm. The capacitance of this insulating layer is inversely proportional to its thickness : $C_g \approx C_{ox} = \epsilon_{ox}/t$, with ϵ_{ox} the electric permeability of the dielectric. In the case of immersed or co-planar gate configurations, the shape and position of the gate electrode can vary considerably, but the capacitance is mostly determined by the electrical double layer (EDL) formed at the graphene surface by the reorganization of ions in the electrolyte media. This EDL acts similarly as a very thin dielectric layer – in the range of angstroms to a few nanometers [171]. The resulting gate capacitance is much larger than that of back-gate dielectrics, and can reach levels comparable to the quantum capacitance C_Q [172]. The gate capacitance is then determined by combining the quantum and EDL capacitances in series : $C_g = [C_q^{-1} + C_{EDL}^{-1}]^{-1}$ [115]. Gate potentials applied across the EDL can be over two orders of magnitude more efficient than through the back gate : consequently, the sweeping range of gate voltage required to capture the linear p- and n-branches is much smaller for immersed or coplanar gates, typically in the order of ±1 V [172], compared to ±10 V for thin oxides going up to ±100 V for thick insulators in the back-gate. In electrolyte media, the range of gate bias sweep must also be restricted to avoid unwanted hydrolysis reactions and other electrochemically-driven reactions at the electrodes [115].

The choice of gate configuration for a GFET sensor depends on the application. The capture of biomolecular analytes (nucleic acids and proteins) normally occurs during immersion of the probe-functionalized graphene layer in the sample, either an analyte-enriched buffer or a biological sample, such as biomedical (blood, serum, urine, etc.), food or environmental. Analyte detection by electrical measurements, though, can occur directly in the same media or after its removal. Immersed or co-planar gate configurations allow electrical measurements directly in electrolytic samples, and are thus usually favored in GFET bioanalytical experiments. The back-gate configuration is generally not used when the GFET interface is immersed with electrolytes, because screening by the EDL can lessen the back-gate voltage. Back-gated GFET sensors are more frequently used

for the detection of volatile analytes in gaseous media, for example for applications such as the detection of pollutants [139, 173]. Nevertheless, back-gated GFETs have been recently reported to detect exosomes directly in buffer using the back-gate by exposing only part of the graphene surface to the sample [10], and they also have been used to detect DNA or naltrexone by immersing the device for exposure followed by drying before measurement [77, 155]. Drying the sample is limited to *a posteriori* detection and can result in non-specific adhesion of various species on the sensor surface, so particular attention to specificity should be exerted in this approach. Finally, let's note that the electrical interaction between analyte and graphene could also differ between dry and immersed conditions, as difference in environment are expected to alter screening effects as well as intramolecular charge transport properties [174].

From transfer curves, several electrical metrics can be used for sensing, as illustrated in Fig. 2.2b-d and discussed in the following :

2.3.1.1. Change in CNP voltage. The most commonly used electrical metric in GFET sensing is a change in the CNP voltage value, *i.e.* the gate voltage associated with the minimum of the transfer curve, as illutrated in Fig. 2.2b. The CNP voltage depends on the doping level of the graphene : for intrinsic graphene at low drain-source bias, it is expected at values close to 0 V, but in reality, it can be either positive if the graphene is p-doped (indicating a larger density of holes) or negative if n-doped (larger density of electrons). The doping level depends on many factors, including the nature of the interface between graphene and other materials (substrate, electrodes, media) and the distribution of charged species and impurities in these materials [175]. Consequently, the choice of materials in device design, their quality and the different processing steps during fabrication of the GFETs have influence on the initial doping state of the graphene layer. In particular, for GFETs made from CVD-grown graphene, the quality of the fabrication process is sometimes associated with the magnitude of the doping [176], as it can reflect the quantity of impurities located between graphene and the substrate following the transfer process (see Sec. 2.2.2) [109, 133]. Efforts in reducing contaminants in the transfer process has been shown to bring the V_{CNP} closer to 0 V [155]. Biosensing experiments based on the change in V_{CNP} can be carried out regardless of the initial doping of the graphene, as long as it is moderate enough to have the CNP visible in the gate voltage sweep at every step of the experiment ; otherwise another metric must be used [78].

In biosensing experiments, the interaction between biological targets and biorecognition elements at the surface of graphene can alter the doping state of graphene, thus creating a shift in the CNP voltage from its initial value. This CNP shift is by far the most common metric for biosensing using GFETs [10, 70, 77]. For example, Fakih *et al.* [143] used the shift in CNP voltage as the sensing metric for K^+ ions : they measured transfer curves for a wide range of concentrations of the target ion, as illustrated in Fig. 2.2e, showing a systematic shift of the curve with analyte concentration. In this experiment, the detection appears to be purely mediated by a doping mechanism, since the whole transfer curve is shifted without altering its amplitude and slope between measurements. From these transfer curves, a clear linear correlation between the CNP voltage and the log of analyte concentration was demonstrated, also shown in Fig. 2.2e. The change in V_{CNP} is also used as a detection metric for complex macromolecular analytes such as DNA oligomers.

For example, Gao *et al.* [85] used the shift of the CNP as a sensing metric for 22nt single-stranded DNA targets binding to hairpin DNA probes. They reported high sensitivity and specificity with this metric, using it to detect single nucleotide mismatches in the target. Finally, the change in CNP voltage is also frequently used to monitor intermediary steps in the assembly of the biorecognition layer, such as graphene chemistry or immobilization of biomolecular probes [74, 85, 129].

Tableau 2.1 – Polarity of reported changes in CNP voltage for different analytes in published studies.

Target	Doping polarity	References
Cations (K^+, Hg^{2+}, Pb^{2+})	n-	[113, 126, 143-145, 177-180]
Glucose	p+	[69, 116, 117]
	n-	[181]
DNA	p+	[24, 25, 85, 109, 117]
	n-	[71, 72, 87, 88, 91, 129, 130, 132, 134, 150, 182-184]

The polarity of the CNP voltage shift raises interesting questions. Polarity represents the direction of the change on the voltage axis : p-doping when the CNP shifts to more positive voltage, n-doping when it shifts to more negative voltage. The polarity depends on the interaction between analyte molecules and the functionalized graphene layer. Polarities of the change in CNP voltage are reported in Table 2.1 for different types of analytes : cations, glucose and DNA. All cation sensors report a negative doping, which is consistent with an electrostatic gating model : the capture of positively-charged targets attracts negative charge carriers in the graphene, generating n-doping and a negative shift of the V_{CNP} [115]. Oppositely, negatively-charged target molecules would increase the density of holes in graphene and generate a positive shift. This electrostatic gating effect is usually postulated as the mechanism also involved in the detection of molecules ; however observations are often inconsistent with this model. For instance, various experiments of GFET sensors for DNA and glucose present opposite polarities in the change of CNP voltage, as compiled in Table 2.1. For DNA sensors, this discrepancy is associated with at least two opposite effects. Studies observing a p-shift often attribute it to a chemical gating effect, in which the deprotonation of the phosphate backbone of the captured target DNA leaves it negatively charged in buffer, leading to the positive shift [86]. On the other hand, observations of n-doping are explained by non-electrostatic stacking interactions between nucleotides and graphene [71, 130], or donor effect [184], which is supported by DFT calculations [185, 186]. These differences may arise from experiment-specific differences in the graphene-analyte-solution interactions when immersed in electrolyte solution, including differences in DNA adsorption, DNA conformation and distribution of counter ions [187]. In the case of glucose sensing, the mechanisms explaining the inconsistencies between experiments exposed in Table 2.1 have not investigated in literature. The case of proteins is more complex, as their polarity changes with the pH of solution. In their work, Kim *et al.* [70] observed the effect of pH on the V_{CNP} shift for a PSA-ACT complex with an isoelectric point of 6.8 : a negative shift of the V_{CNP} was observed at pH 7.4 when the protein is negatively charged, and oppositely at pH 6.2 when the protein is positively charged. Considering that the density of proteins on graphene is typically too small to generate such a shift via direct charge transfer [136],

the observed shift in V_{CNP} was explained in this case by asymetrical scattering by charged impurity [70]. To summarize, the mechanisms behind the polarity of the V_{CNP} shift seem to depend not only on the nature of the target, but also on design or environmental factors considering diverging responses reported from similar targets. Competing mechanisms have been suggested for DNA to explain those discrepancies and a mechanism has been suggested for proteins, but this topic calls for further investigation.

2.3.1.2. Change in transconductance. A second type of metric in sensing with transfer curves is a change in the transconductance $g_m = \partial I_{ds}/\partial V_g$, which is the slope of the linear part of the p- or n-branch of the transfer curve [188, 189]. This metric is illustrated in Fig. 2.2c. The transconductance is an important indicator of transistor performance, *i.e.* its ability to convert a small change in voltage in a large change in current. For a given device geometry (graphene surface and gate electrode), the transconductance is mainly dependent on the mobility μ of charge carriers, as described in Eq. 2.2. The mobility of charge carriers in graphene is usually an indicator of its structural and electronic quality [115] since it is considered to be inversely proportional to the number of impurities in the sample [175, 190]. In a biosensing experiment, the introduction of analytes can alter the transconductance by introducing additional scattering sites and hence increasing disorder, which results in a change in the transfer curve slope as illustrated in Fig. 2.2c. A limited number of studies explicitly use the change in transconductance as a metric for biosensing, although many experiments show a variation of the slope in at least one of the branches, as can be observed for instance in experiments by Chen *et al.* [105] shown in Fig. 2.2f and by Farid *et al.* [127] shown in Fig. 2.2g. The polarity of the added scattering sites influences which charge carrier is affected and the slopes often vary asymmetrically, as seen in Figs. 2.2f-g.

Using the change in transconductance directly as a metric requires a linear fit of the p/n branches ; the required postprocessing for such analysis and the subjectivity involved in determining the lower and upper limits of the linear range can be considered as limitations of this method. Some groups use this metric indirectly by measuring the change in current at a fixed gate bias [105, 191]. This is robust in cases where the change of transconductance is the only observed variation. For example in Fig. 2.2f by Chen *et al.* [105], exposure to the analyte changes only the transconductance of the p-branch without affecting the CNP voltage ; authors thus calibrated the current variation at $V_g = -0.5$ V against analyte concentration, as shown in Fig. 2.2f. In cases where the CNP voltage changes simultaneously to the transconductance, this indirect method would be problematic because it would then aggregate both variations, as discussed further in the following section. Finally, in other cases, the absence of change in the transconductance is explicitely reported and used to interpret the underlying mechanism of the biosensor. For example, Okamoto *et al.* [114] observed positive doping without any variation in transconductance after the binding of negative antigen fragments, allowing them to hypothesize that antigen capture only changed the negative carrier density without introducing scattering effects.

2.3.1.3. Change in current. The last type of reported electrical metric with transfer curves is a change in the amplitude of the electrical current, either in the p/n branches or at the CNP, or both, as illustrated in Fig. 2.2d. For example, Chen *et al.* [105] observed a change of current only in the

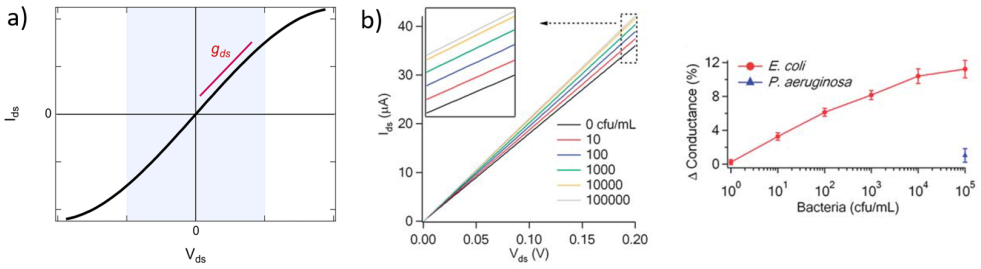

Figure 2.3 – Output curves in GFET biosensors. (a) Typical output curve $I_{ds}(V_{ds})$ of a GFET : the shaded area indicates the low-bias regime, expected linear, which slope corresponds to the output conductance g_{ds}. (b) Left : Experiment with a GFET functionalized with *E. coli* antibodies, showing a change in output conductance after incubation with the bacteria. Right : Corresponding change in the relative conductance as a function of *E. coli* concentration. Reprinted with permission from Huang *et al.* [73] © 2011 The Royal Society of Chemistry.

p-branch (see Fig. 2.2f), while Farid *et al.* [127] reported a change in the electrical current at the CNP (see Fig. 2.2g). Electrical current being determined by the product of carrier charge, density and velocity ($I = qnv$), a change in current indicates either a change in the density of charge carriers, or in scattering processes, or a combination of both. As discussed in the two previous sections, interactions of biological analytes with the sensor can indeed result in both these effects : a lateral shift of the CNP results from a modification in charge carrier density, and a decrease in transconductance in one or both the branches reflect an increase of scattering. A change of current at a given gate voltage, although easiest to measure, is thus difficult to interpret as it may add or subtract contributions from two different mechanisms. Following the current amplitude at the CNP should in principle control for any shift in the doping state, but even this can be convoluted with an asymmetrical change in transconductance. For example, in Fig. 2.2g, Farid *et al.* [127] report a shift of V_{CNP} accompanied with a decrease of the CNP current, but the latter may actually be driven by the asymetrical change in transconductance. In addition, the current minimum of the transfer curve can be affected by the rate of the gate sweep, which can vary with changes in current amplitude unless constant integration time is specified. Overall, the change in the CNP current is an experimentally-practical metrics to be used empirically, but one should keep in mind that it is co-dependent on both the two other metrics.

2.3.2. Output curves

Apart from transfer curves, GFETs can be operated to measure output curves, in which the drain-source current I_{ds} is recorded as a function of drain-source voltage V_{ds} for a fixed gate voltage V_g. The typical output curve of a GFET is represented in Fig. 2.3a : as the applied bias increases from zero, the amplitude of the current increases with the same polarity as the applied bias. The curvature of the output curve is generally considered a good indicator of the quality of the contacts between graphene and source/drain electrodes, and of charge transport along the graphene. With good graphene and electrical contacts, a linear ohmic regime is usually expected at low bias [192,

193]. In practice though, a positive curvature or superlinear regime is sometimes observed due to potential barriers created by non-ideal contacts or defect sites [169]. The output conductance g_{ds} is defined as the slope of the output curve. Its amplitude is evidently function of the gate voltage, which modifies the carrier density, as seen in Tsang *et al.* [10].

A change in the output conductance is occasionally used as a detection metric in GFET sensing experiments. For example, this is done by Huang *et al.* [73] in Fig. 2.3b : on the left, they show output curves taken at $V_g = 0$ V after a fixed incubation time in increasing concentrations of bacteria . On the right, the variation in current at $V_{ds} = 100$ mV is used for quantitation of the bacteria. The increase in output conductance with increasing concentrations suggests either p-doping or an increase of the transconductance (decrease of disorder). To disambiguate between the two, transfer curves were acquired at concentrations 0 cfu/mL and 100 cfu/mL, showing showed a p-shift and no transconductance change. This allowed the authors to attribute the variation of output curves to an increase of negative carriers in the system, due to the negatively charged bacteria through electrochemical gating. As this example demonstrates, output curves as a sensing metric should be paired with at least a pair of transfer curves in order to distinguish a change in carrier concentration from a change in disorder.

2.3.3. Time series

In time series, the evolution of the drain-source current (or conductance, or resistance) is collected as a function of time at fixed drain-source and gate voltages. Time series typically start recording before the introduction of reagents and follow the evolution of biochemical interactions between analyte and the sensor. These interactions induce variations in current as a function of time, due to changes in charge carrier concentration or scattering effects *via* mechanisms discussed in earlier sections. Detection of the analyte, and sometimes its quantitation, is assessed from the change in electrical current after injection of the analyzed sample. Since the gate voltage is fixed, this curve is akin to following the evolution of a single point of the transfer curve in time. The choice of gate voltage has a direct influence on the amplitude and the polarity of the signal. It is generally expected for the signal amplitude to be maximized when choosing a gate voltage corresponding to a high transconductance region of the transfer curve [92]. Actually, the interplay between gate voltage and signal amplitude can be quite complex, as illustrated in subsets a to e of Fig. 2.4. Subset a represents a system undergoing a p-doping shift between times t_1 and t_2, and subsets c to e schematize the resulting times series taken at three different gate voltages (V_A, V_B and V_C). Even though they result from the same analyte-sensor interaction, time series obtained at gate voltages V_A, V_B and V_C exhibit current changes of different amplitudes ($\Delta I_A > \Delta I_B$) or even different polarities ($\Delta I_B < 0$ and $\Delta I_C > 0$). We see here how a slight change of gate voltage, especially close to the CNP, can result in a significantly different profile of the time series. This was experimentally demonstrated by Sudibya *et al.* [67], who observed both an increase and a decrease of current with increasing concentration of Ca^{2+} ions, depending on the chosen V_g. These results highlight the fact that a variation in electrical current cannot be associated to a specific doping polarity without characterization of the transfer curve profiles before and after interaction with the

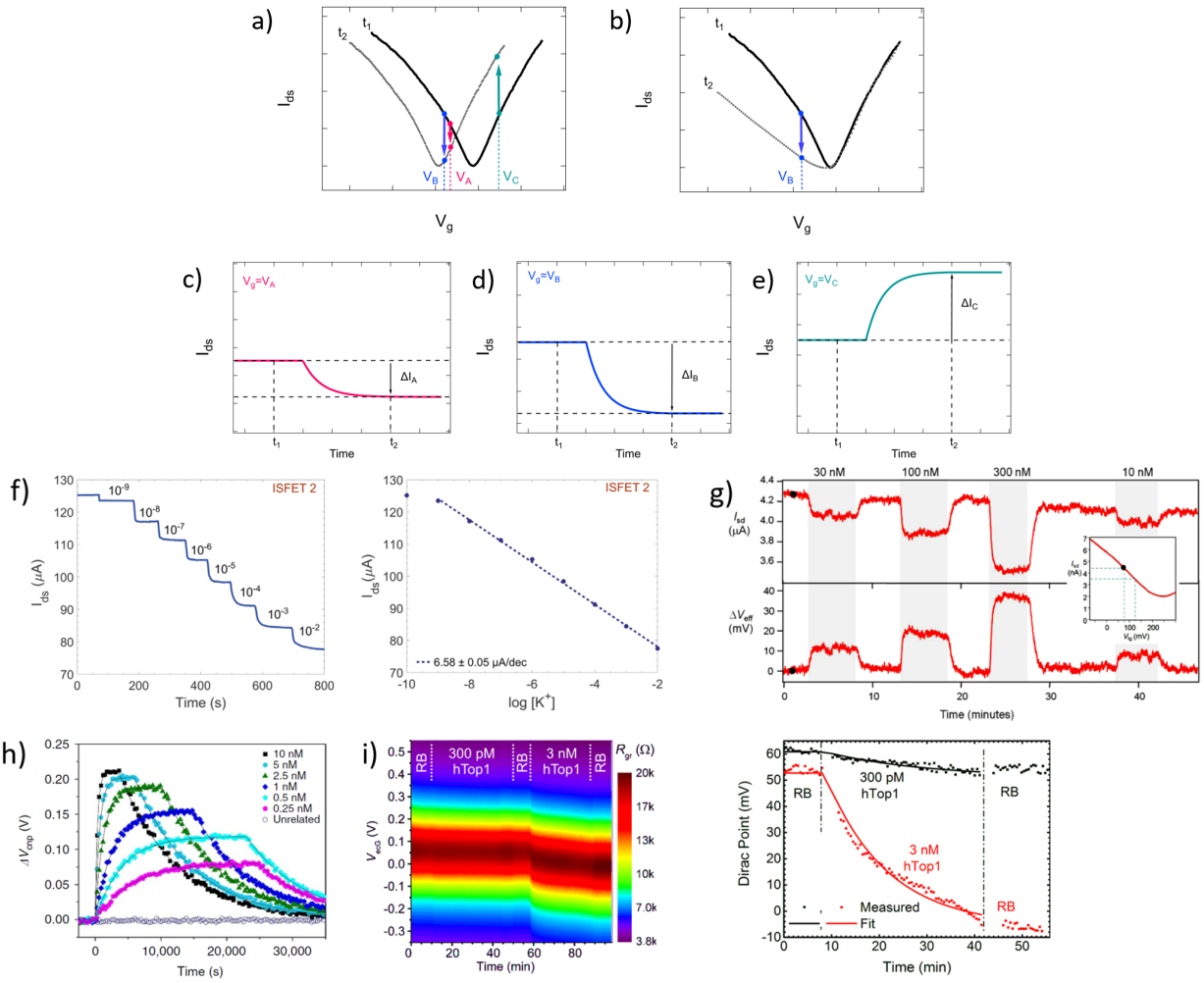

Figure 2.4 – Time series in GFET biosensors. (a) GFET sensor detecting a left-shift of the CNP voltage, captured in two transfer curves at time points t_1 and t_2. (b) Same for a system undergoing a change in p-branch transconductance. (c)-(e) Corresponding time series of current $I(t)$ at specific gate voltages V_A, V_B and V_C. (f) Left : Time series of current in a GFET sensor for K^+ ions, recording the exposure to increasing concentrations of analyte. Right : Corresponding change in current as function of K^+ concentration. Reprinted with permission from Fakih *et al.* [143] © 2019 Elsevier B.V. (g) Time series of a GFET sensor for thrombin, recording the introduction of various concentration of analyte separated by washing cycles. Top series shows the current as a function of time, and bottom series the corresponding change in CNP voltage using the conversion described in the inset. Reprinted with permission from Saltzgaber *et al.* [92] © 2013 IOP Publishing, Ltd. (h) Time series of the change in CNP voltage, also obtained by conversion, showing hybridization and dissociation kinetics between ssDNA probes immobilized on a GFET and different concentrations of the complementary ssDNA. Reprinted with permission from Xu *et al.* [81] © 2017 Springer Nature. (i) Left : Two-dimensional time series showing electrical current as a function of both gate voltage and time, here for a GFET sensor targeting the hTop1 enzyme. Right : Time series of the CNP voltage, extracted from the 2D plot, during introduction of hTop1 at two concentrations (right). Reprinted with permission from Zuccaro *et al.* [82] © 2015 American Chemical Society.

analyte. Moreover, current variation in time series cannot be interpreted as a specific mechanism by itself : for example, the time series represented in Fig. 2.4d could equivalently be generated by p-doping (Fig. 2.4a at V_B) or by a decrease of transconductance in the p-branch (Fig. 2.4b at V_B). Insight from transfer curves is thus also necessary in order to correctly identify the mechanism generating current variations in time series.

Time series most often directly present the value of the current as a function of time, as in experiments of Fakih *et al.*[143] in Fig. 2.4f and of Saltzgaber *et al.* [92] in Fig. 2.4g (top part). Sometimes, the current is converted as a change in voltage such as in Saltzgaber *et al.* [92] in Fig. 2.4g (bottom part). An effective voltage shift representation was also used by Xu *et al.* [81] to study the kinetics of DNA hybridization events and extract binding constants for several concentrations of target (Fig. 2.4h). In this approach, the current change ΔI_{ds} is converted to a voltage change with the relation $\Delta V_{CNP} = \Delta I_{ds}/g_m$. It's important to note that this approach is only valid if the transconductance remains constant before and after the addition of targets. As previously mentioned, transfer curves should be provided to confirm that doping is the only mechanism at play. Signal in time series is sometimes normalized as a relative change from a baseline current. Use of normalization can help in assessing signal strength despite sensor-to-sensor variations and effects associated to the medium [83]. For example, Chen *et al.* [78] used a simple normalization I_{ds}/I_0 with I_0 the initial current in deionized water and Liu *et al.* [75] showed a relative current $(I_{ds} - I_0)/I_0$ with I_0 the stabilized current after immobilization of the probe molecules. When normalized signal is presented, the conditions used for the baseline should be specified and it is good practice to make available the original time series of the baseline and of the experiment before normalization.

It is possible to avoid the limitations of time series following a constant gate voltage, by implementing a more sophisticated acquisition protocol based on an oscillating gate voltage. In this approach, the gate voltage is continuously swept back and forth over a defined range while the drain-source current is recorded. This results in a two-dimensional mapping of the electrical current as a function of both gate voltage and time. Ideally, the range of the gate voltage sweep is chosen to cover the CNP, which allows to follow the doping state of the graphene at each time point. For example, Zuccaro *et al.* [82] applied this approach of continuous gate sweeps to produce 2D maps of the low-bias resistance as a function of gate voltage and time, as shown in Fig. 2.4i (left). This approach allows to extract a time series of the V_{CNP}, as illustrated in Fig. 2.4i (right), which is a powerful way to quantify the kinetics of the change in doping state.

2.3.4. Comparison of electrical metrics in "before-after" *vs* "real-time" protocols

An important consideration when designing a biosensing experiment with GFET sensors is deciding which type of electrical measurements and metrics to use, and in which sequence to collect them. The design of the acquisition protocol depends on the nature of the scientific question or application for which the biosensor is used. We can divide protocols into two categories : "before-after" and "real-time". The former refer to experiments comparing the value of a metric, at a specific time point after exposure to the sample, to its baseline value before exposure. This is

suitable if the goal is to assess the presence of a target (yes/no type of result). It is also relevant for applications requiring quantification of an analyte : the amplitude of the change in the chosen metric is then compared to a previous calibration of the sensor. However if the application or the scientific question requires information about the kinetics of the biochemical interaction, then a "real-time" protocol recording the evolution of a metric over an relevant period of time is necessary. Among the previously described metrics, some focus on the state of the system at a specific time point, while others allow to monitor the evolution of the system, which makes them naturally more or less convenient for each protocol type.

Transfer curves are especially suitable for before-after measurements, as they provide an informative picture of the electronic state of the sensor at a fixed point in time. Indeed, this type of curve provides information on the doping level, through the CNP position, as well as on both carrier mobilities (electrons and holes), through the transconductance of each branch. Transfer curves can be used to assess completion of different steps of sensor assembly, functionalization and biochemical interactions, by collecting a gate sweep after each step and comparing the resulting electrical metrics to the initial curve. Even in experiments focused on real-time measurements for reaction kinetics, it is recommended to collect at least initial transfer curves to assess the performance of the sensors, as done by Cohen-Karni *et al.* [194]. In general, before-after analysis of transfer curves is useful for events that have clear before and after states, which are typically before exposure to a reagent and after the reaction with this reagent is considered completed. This type of measurements is commonly used to verify the impact of a passivation layer [74], to confirm the presence of functionalization adducts [85], to assess the linking of the probes [145] or the linking of the target to the probes [72]. In sensing experiments, this method is most frequently used for quantitation with various types of analytes including ions [145, 146, 180], proteins [127, 153], glucose [69, 181] and DNA [25, 91, 109]. It is also used for simple yes/no detection, like to assess the presence of a single-mismatched DNA [71, 72, 85] or a specific ion [180]. Output curves can be used in the same way as transfer curves in before-after detection schemes, such as in Huang *et al.* [73], but they provide less information on the electrostatic state of the graphene and on physical mechanisms occurring in the system (e.g. change in doping or diffusion). The analysis of transfer or output curves usually requires post-processing, because the extraction of the CNP voltage, transconductances or output conductance can be performed only after completion of the relevant voltage sweep. From the transfer curve, the CNP voltage is often estimated using the point of the transfer curve with the minimum of current [156]. Other studies use curve-fitting to extract the voltage associated with the minimum, usually with a quadratic function [91] or with more sophisticated models [25]. Curve fitting is a more precise method since it is not limited by the width of the gate voltage steps during the measurement. The postprocessing required to determine the transconductance of each branch (g_h and g_e) involves subjectivity in determining the lower and upper limits of the linear range, which can be considered a limitation of this method. Real-time measurements are usually performed via unidimensional or bidimensional time series as described in Sec. 2.3.3. Real-time measurements are of course essential to study the kinetics of a dynamical reaction [69, 81-83, 114, 195]. In such experiments, like the study of DNA hybridization by Xu *et al.* [81] illustrated in Fig. 2.4h, the electrical

current is monitored during the introduction of analytes and during washing steps as well. Time series covering washing steps enable to monitor either the removal of non-specific species and unbound analytes or, in the case of weak probe :target affinities, to observe the dissociation of the analyte from the sensor. Time series can be adjusted with a Langmuir binding kinetics model or similar model to estimate adsorption and dissociation constants [81, 133]. Time-resolved measurements can also be used for quantification purposes. For example, Fakih *et al.* [143] studied the influence of K^+ concentration with both transfer curves (Fig. 2.2e) and time series (Fig. 2.4f), and observed similar correlations with analyte concentration. This type of experiment is especially conclusive when the signal reaches a clean plateau during target exposure, like in Fig. 2.4f : such stabilization of the signal facilitated its quantification, which is critical for analyte quantitation. A combination of the two purposes, kinetics and quantification, can be done simultaneously, like in Saltzgaber *et al.* [92] in Fig. 2.4g, where the successive introductions of different target concentrations, separated by washing steps, are analyzed to gain insight on the effect of concentration on the kinetics of the reaction. Real-time experiments also allow to assess the reaction rate and the time required to stabilize the interaction between the analyte and the target, which can then be used to determine how to time transfer curves for before-after measurements. For real-time biosensing, experiments need to be done in a saline environment with a coplanar or immersed gate configuration, which require a flow cell or microfluidic circuitry. Measurements can be done in a static or continuous flow setting. Faster reaction times have been reported for DNA sensing in such settings [81, 157], but continuous flow was reported to lead to noisier signals because of vibrations due to the water pump [78]. The choice of flow configuration thus depends on the priorities in the experiment.

For most experiment purposes, both types of measurements are best used together. Standard time series are very instructive about the kinetics of the analyte-sensor interactions, but since they only measure the current at fixed biases, they provide little insight on the physical mechanism underlying these interactions. When time series are coupled with transfer curves, either at specific time points or, even better, continuously in two-dimensional time series [82], then the mechanisms behind the evolution of the current can be further investigated. In addition, quantitative analyses based on current changes (either for quantitation or kinetics) often rely on the assumption that the change in current is proportional to the change in graphene doping state, but this is only true in the linear regime of p/n branches and if there is no change of the charge carrier mobilities during the reaction ; this needs to be confirmed with transfer curves. Finally, when using before-after experiments without any time series, it is difficult to assess whether the interaction with analytes is stabilized or not ; consequently, incubation times are often chosen very long in order to make sure the reaction has occurred. The use of time series, at least during calibration assays, could help optimize the incubation time used in detection assays.

2.4. Performance assessment

The experiments considered in the scope of this review aim at developing GFETs as a bioanalytical technology, *i.e.* for the detection or quantitation of molecules relevant in biology. In this section, we review the criteria used to evaluate the performance of GFETs as biosensors. In this context,

performance include two aspects : quality and reliability [196]. Quality criteria are established by the performance of the sensor itself with respect to several detection metrics. In the following, we discuss four of these metrics : spatial range of detection, limit of detection, sensitivity to target concentration and response time. Reliability criteria can be assessed by the experimental design ; here we will discuss appropriate statistical sampling and analysis, as well as controls experiments.

2.4.1. Spatial range of detection

For electrolyte-gated GFETs, it is important to take into account charge screening by mobile ions in the medium. According to the Debye-Hückel model, charged molecules in solution are screened by mobile counter-ions such that their electric potential is dampen exponentially with distance, with a decay constant λ_D called the Debye length. This constant represents the screening length and is given by

$$\lambda_D = \sqrt{\frac{\epsilon k_B T}{2 N_A e^2 I}}, \tag{2.3}$$

where ϵ is the permittivity of the medium, k_B the Boltzmann constant, T the temperature, N_A the Avogadro's number, e the electron charge and I the ionic strength of the solution. The ionic strength is given by $I = \frac{1}{2}\sum_i \rho_i z_i$ where ρ_i and z_i are respectively the density and valence of ion species i. Generally speaking, the Debye length represents the distance at which charges are screened ; thus, charges located farther than the Debye length are usually considered out of range for electrostatic detection by a FET sensor. [197-199] For an aqueous solution at room temperature, this length becomes $\lambda_D(\text{nm}) = 0.304/\sqrt{I}$ where I is in mol/L. For 1X PBS buffer, it is as short as $\sim$0.7 nm. Therefore, one must take λ_D into consideration when designing specific probe molecules, as too-long a distance between target binding events and the FET surface may significantly reduce the signal [168, 199-201] or completely screen it out [168, 197]. Such limitations due to Debye length on the spatial range of detection in FET sensors have been experimentally observed in different types of FETs. For example, Sorgenfrei *et al.* [199] used an ssDNA probe tethered to a CNTFET to study the effects of shortening the Debye length, via changing PBS concentration, on the detection of probe hybridization with a target complimentary DNA (cDNA). They found the resistance to decrease significantly (resistance change $\Delta R/R$ dropping from 80% to 10%) when increasing buffer salinity from 0.1X to 5X PBS (corresponding to a decrease of λ_D from 2.3 nm to 0.3 nm). They also showed that moving the target cDNA further from the surface, by removing two base pairs from the target cDNA ($\sim$0.66 nm distance increase), reduced $\Delta R/R \sim$ from 80% to 20%. This was performed in 1X PBS and, notably, a signal was still detectable, although greatly reduced, even though hybridization occurred at distance of $\sim$1.36 nm, exceeding the estimated λ_D of 0.7 nm.

This proximity requirement between the captured analyte and graphene presents a challenge in designing the interface of GFETs, especially in biomedical applications targeting detection in physiological samples. Saline buffers such as 1X PBS or 1X PB, commonly used to emulate physiological environments (e.g. human blood), have a very short Debye length of 0.7 nm. In comparison, common probe molecules such as antibodies for protein detection can be upwards of 10 nm in size. To circumvent this issue, some groups have opted to use solutions with low ionic concentration in

order to achieve λ_D above 10 nm. [70, 92, 202] Others have designed smaller probe molecules such as antibody fragments [114, 203] or aptamers [89, 168, 204, 205], allowing to reduce probe length from 10-15 nm to < 5 nm, in order to improve device sensitivity. For instance, Kim *et al.* [168] found that replacing a typical antibody probe ($\sim$ 10 nm) with an aptamer probe ($\sim$ 4 nm) on otherwise similar GFET sensors improved sensitivity to the target protective antigen (PA) by 1000 times (12 aM to 12 fM) in 10 μM PBS ($\lambda_D \sim 23.6$ nm). They also found that signal of PA binding was completely screened out in 1 mM PBS ($\lambda_D \sim 2.3$ nm), even using small aptamer probes, whereas using 10 μM and 100 μM PBS (7.3 nm and 23.6 nm, respectively) showed similar signal intensity (determined by the shift in the charge neutrality point) and limit of detection (smallest concentration detected). Interestingly, the range of PA concentration covered before reaching signal saturation was narrower in 100 μM PBS, indicating lower salt concentration solutions to yield a wider range of detection.

In the case of DNA hybridization experiments, however, many groups have reported detection at very high salt concentrations[24, 71, 129] and even for very long DNA sequences[72]. This reduced limitation to the screening length is likely enabled by the capture of charges close to the FET surface by the first nucleotides of the probe DNA, regardless of its total length. Although high salt concentrations are preferred for stabilizing double-strand DNA, signal and sensitivity can still be improved by decreasing lower salt concentrations[72, 81, 91, 129]. Additionally, single nucleotide polymorphism have been detected [24, 71, 81, 150], even if located further along the DNA strand than the Debye length. This is explained by the decreased hybridization stability of single mismatched DNA [24, 71], leading to partial or complete dissociation of the duplex near the graphene surface.

Many strategies for overcoming Debye length limitations while maintaining physiological environmental conditions have been proposed : such as displacing the screening range away from graphene by covering it with a polymer layer permeable to biomolecules [206] or with charged macromolecules to create a fixed-ion region. [83, 207] Similarly, Chen et al. reported extending the screening length by adding an MoS_2 layer on graphene [184]. Other strategies include indirect detection of a target via the products of its reaction on an enzyme, produced outside of the screening length and diffused to the surface of the GFET [9] and using a solution containing 12.5 mM of $MgCl_2$ in a 30 mM tris buffer, known to provide similar dsDNA stability as in 1X PBS, to increase λ_D to 1.6 nm. [72] Finally, issues related to electrolyte screening can be circumvented all together using a backgate and measuring in air conditions. [26]

2.4.2. Limit of detection and sensitivity

The performance of GFETs as biological transducers is commonly referred to as their sensitivity [71, 84, 150]. Formally, analytical sensitivity describes the ability of the sensor to distinguish between small differences of analyte concentration [208]. Interestingly, this property is actually rarely assessed in bioanalytical GFET studies ; rather, the most widely reported performance metric is the limit of detection (LOD) [24, 70, 76, 86], which indicates the lowest concentration at which

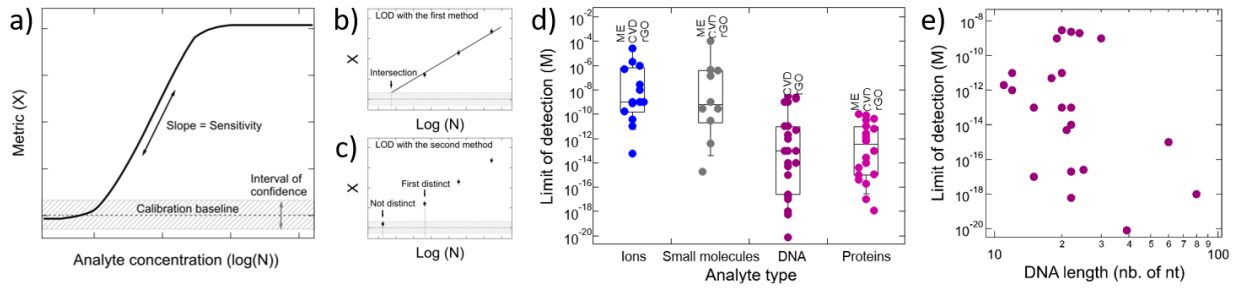

Figure 2.5 – Sensitivity and limit of detection (LOD) in GFET biosensors. (a) Typical calibration curve for a GFET sensor, showing the change in a given electrical metric as a function of analyte concentration. Sensitivity represents the slope of the linear regime, while the LOD is the concentration at which the change in the metric exceeds a chosen confidence interval. (b-c) Methods for the experimental determination of the LOD based on extrapolation and direct measurement, respectively. (d) LODs reported in the literature for GFETs, classified by analyte type : ions, small molecules, DNA and proteins. Data points are also separated as function of the type of graphene used in GFET fabrication (ME=mechanical exfoliation, CVD=chemical vapor deposition, rGO=reduced graphene oxide). (e) Reported LODs for DNA detection represented as function of the length of the targeted DNA sequence.

an analyte can be confidently detected by the sensor. Both of these metrics, sensitivity and LOD, are often conflated, yet they represent distinct standards.

Sensitivity is a crucial performance metric for quantitation applications, in particular when it's required to identify analyte concentration with great precision. Sensitivity can be assessed from the calibration curve of the sensor, *i.e.* the evolution of a chosen electrical metric (ex. CNP voltage, current, see Sec. 2.3) as function of analyte concentration, as illustrated in Fig. 2.5a. Sensitivity is generally quantified as the slope S of the linear regime of the curve, given by

$$S = \frac{\Delta X}{\Delta N}, \tag{2.4}$$

where ΔX is the variation of the electrical metric corresponding to a change ΔN in analyte concentration. As discussed in Sec. 2.3, analyte-sensor interactions in GFETs are often transduced as a change in CNP voltage, yet the exact relation between ΔV_{CNP} and analyte concentration is complex and depends on the precise layout of the functionalized graphene interface and of its coupling to analyte and media. Sensitivity can however be assessed empirically. This is straightforward when the CNP voltage is directly measured as the metric, for instance in before-after experiments with transfer curves : Fakih *et al.* [143] used this approach to assess the sensitivity of their ion sensor in mV/decade. Most often, the measured electrical metric is the drain-source current, especially in real-time experiments, in which case the sensitivity should also be proportional to the transconductance g_m (per Eq. 2.1). This explains why conventionally, the gate voltage for time series is chosen at the place in the curve with the highest transconductance value [92, 93]. Transconductance itself is proportional to the mobility μ of the graphene, the gate capacitance C_g and the width-to-length ratio W/L of the graphene surface (Eq. 2.2). In addition, it is generally understood that the sensitivity of a GFET is also limited by noise [209] : the larger the variance in the signal, and thus in

the calibration curve, the more difficult it is to distinguish between close concentrations of analyte. Along this line, Fakih *et al.* [64] argue that maximizing material mobility, sensor active area and capacitive coupling allows to minimize noise and improve sensitivity. In general however, the sensitivity of GFETs as biosensors has not been extensively studied or reported. A deeper understanding of its underlying factors and of their relative importance would be valuable to better design GFETs, especially for applications requiring precise quantitation of the analyte.

The limit of detection is a different important performance metric, that determines the minimal concentration of analyte that can be detected by the sensor. The LOD is determined as the concentration at which signal exceeds the baseline by an interval of confidence, as illustrated in Fig. 2.5a. A low LOD depends positively on signal strength and is limited by noise and other sources of variance in the measurements. Although distinct, the LOD and sensitivity can be correlated. For instance, in Fig. 2.5a, we can see that improving the sensitivity or the slope in the calibration curve is likely to lower the LOD. The LOD is relevant for detection and also for quantitation of analytes : it determines the lower bound of the dynamic range of the sensor, the upper end being limited by the saturation of the signal. In practice, the required LOD depends on the purpose of the sensor : for some applications, a predefined LOD needs to be achieved as prescribed by norms or regulations, for example safe Pb^{2+} levels in childen's blood [145] or glucose levels associated with diabetes [181]. In the development of GFET biosensors, the LOD is the most frequently reported indicator of performance, and is often benchmarked against other detection techniques, such as PCR-based techniques for DNA detection [24], or ELISA tests for immunoassays [195]. We surveyed the literature on GFETs used as bioanalytical sensors and retrieved 61 studies reporting a value for the LOD (see the Electronic supporting information, Annexe A for a list of the studies). An interesting observation from that compilation is that the reported LODs cover a very wide range of concentrations, from 0.1 mM [116] to 8 zM [149], which represents a remarkable spread of 16 orders of magnitude. In the following, we discuss the different factors that can influence the LOD in GFETs.

First, we note that methodologies to determine the LOD vary between studies. They can usually be classified in one of two categories : extrapolation [81, 157, 210, 211] or direct measurement [25, 26, 70, 77, 144, 145, 195], illustrated in Fig. 2.5b and c respectively. Both approaches first require precise characterization of the sensor baseline, *i.e.* the value and standard deviation of the chosen electrical metric (ex. CNP voltage, current) in absence of the targeted analyte. The LOD differs from the baseline of the sensor by an interval of confidence, defined as a chosen multiple of the standard deviation. The International Union of Pure and Applied Chemistry defines the LOD to be at three times the standard deviation [212] and the number of replicas for baseline measurement is recommended at $n = 20$ [213]. In the first approach, the electrical metric is measured in presence of different concentrations of analyte and the resulting response is extrapolated towards lower concentrations : the LOD is then identified as the concentration value at which the extrapolation function intersects with the upper bound of the interval of confidence. For example, Chen *et al.* [78] used a linear fit to extract a correlation between the relative current change observed in time series and the logarithm of analyte concentration. From data taken in a range of 10 nM to 100

μM, they extrapolated this linear fit until reaching a signal-to-noise ratio of 3, and obtained an LOD value of 0.3 nM. More complex non-linear fits can be used as well for extrapolation, such as a Hill-Langmuir equation as used by Li *et al.* [68]. The second approach consists in actually making measurements at decreasing concentrations, with replicas, until the observed change in the electrical metric is no longer statistically different from the interval of confidence. For instance, Cai *et al.* [71] measured the sensor response for concentrations down to 10 fM of complementary DNA. However, after assessing the noise level with a blank control test, the LOD was established at 100 fM, corresponding to a signal exceeding three times the background level. This underlines the importance of assessing the baseline value and its variance. In some specific cases, it is more relevant to use another threshold than the baseline signal to determine the LOD. For example, in Campos *et al.* [24], the LOD of perfectly-matched DNA is determined as the concentration sharing the same signal value as the highest signal obtained with single-mismatched DNA. In general, the LOD assessment method should be detailed in order to enable proper benchmarking between studies. In our literature survey (see Electronic supporting information, Annexe A), the LOD values were taken as reported, without adjustment for the determination method. Extrapolation methods tend to require less measurements, but the extracted LOD can be off the mark if analyte signal deviates from the extrapolation model at low concentrations. In this case the second type of approach is the most reliable as it ensures that concentrations above the LOD can really be distinguished from the baseline. When used properly, *i.e.* with robust statistical analysis and with the right extrapolation function, the two methods should provide equivalent results for the LOD. In studies, the lower concentrations measured and the extrapolated values vary by usually less than an order of magnitude [81, 157] and at most, by two [181]. The data may also include underestimations of the LOD, if the interval of confidence associated with the variance of the baseline is not properly assessed. All things considered, we estimate that discrepancies from the LOD evaluation methods add some variance to the dataset, but are not sufficient to explain the wide spread of LODs across all experiments.

To analyze the distribution of LODs in the literature, we first classified the data by type of analyte, namely ions, small molecules, DNA and proteins. Figure 2.5d compiles individual data points and the corresponding box plots characterizing their distribution for each type of analyte. Interestingly, we observe differences in the distributions with analyte type. Ions sensors show the most compact distribution, with a geometric mean and standard deviation of the LOD = $10^{(-8.5\pm2.3)}$ M (n = 14). This is consistent with ions being the most homogeneous category, almost entirely consisting of monoatomic species. Small molecules present a distribution of $10^{(-8.9\pm3.2)}$ M (n = 10), which is not significantly different from that of ions (p-value = 0.7 for a two-tailed two-sample Student's t-test assuming non-equal variances). The variance for small molecules is larger than for ions, which may reflect a higher heterogeneity in this category regrouping glucose and various other organic molecules. We note that the charge of the analyte does not appear as a dominant factor in determining the LOD of GFETs : ions present a net charge whereas small molecules don't - yet they present similar LOD averages. On the other hand, nucleic acids and proteins present LOD distributions with much lower averages, respectively $10^{(-13.2\pm3.4)}$ M (n = 23) and $10^{(-13.1\pm2.4)}$ M (n = 20). These distributions are very similar to each other, and both significantly different from

that of ions ($p < 1e\text{-}4$ and $p < 1e\text{-}5$, respectively). It appears that there is a distinct segregation between small species (ions, small molecules) and large macromolecules (DNA, proteins). This is likely due to the size difference : macromolecules contain hundreds to thousands of atoms arranged in complex higher-order tri-dimensional structures. Consequently, they are individually more perturbative of the electrostatic environment near the GFET graphene layer, either by carrying more charged sites, by covering a larger area on the graphene and/or by displacing their volume in the saline media. In the same direction, the few GFET studies on the detection of cell-sized analytes such as bacteria and viruses also tend to report very low LODs for these very large analytes [74-76].

Within macromolecules, the size of analytes can also vary significantly, depending on the length of the DNA sequence or the mass of the protein. Size effects at this scale have been reported in other techniques, for instance improved detection metrics with longer DNA sequences in surface plasmon resonance [214] or DNA microarrays [118]. In the GFET literature, we looked for a distribution of LODs with size in macromolecules, but observed no significant trend in the available data. For instance, Fig. 2.5e maps the reported LODs of the 23 DNA studies as function of the length of the target sequence, which reveals no observable correlation. We obtained a similar scattering with protein data points as a function of protein mass (not shown). This suggests that eventual size effects within macromolecules, if they exist, are not dominant compared to variations in sensor and experimental design between studies (discussed below). It should be noted that a series of studies from the Johnson group, using a consistent GFET design, reported lower LODs when increasing the length of the DNA oligomer [25, 85, 86]. In this specific set of experiments, GFETs were rinsed and dried after immersion in the DNA solution, so that detection was performed using back-gated transfer curves. In contrast, most GFET DNA studies use electrolyte-gated designs, in which detection is limited by Debye screening and thus dominated by nucleotides tethered near the graphene surface. This could explain the lack of dependence with DNA length observed overall in the literature data.

Once classified by the type of analyte, LOD values in the literature data still spread over 8 to 12 orders of magnitude per analyte type ; this remaining variance must come from differences between studies in the design of GFET sensors (e.g. materials, geometry, surface chemistry, ...). In particular, it is often suggested that the quality of the graphene is important to produce an efficient FET sensor [77, 109, 147, 150]. The underlying rationale is that LOD is limited by noise, and that high-quality graphene presents higher mobilities and lower noise spectral density [209]. We looked into the type of graphene used in GFET assembly (exfoliated, CVD or rGO) as a proxy for graphene quality : it is commonly expected for mechanically exfoliated graphene to present high mobility, and for rGO to present a high density of detects, due to their respective fabrication and transfer methods (see Sec.2.2.1-2.2.2). In the data we collected from the literature, reported mobilities for exfoliated graphene are between 200 $cm^2/(V.s)$ [9] and 4400 $cm^2/(V.s)$ [215], and in a similar range for CVD from 605 $cm^2/(V.s)$ [150] to 5000 $cm^2/(V.s)$ [143]. For rGO, they are between 6 $cm^2/(V.s)$ [216] and 23 $cm^2/(V.s)$ [70], so indeed lower by 2-3 orders of magnitude. In Fig. 2.5d, individual LOD data points in each analyte type were separated in three columns, corresponding to the type of graphene used in the fabrication of the GFETs. From this dataset, we observe no significant correlation between graphene type and LOD values. In particular, LODs

from low-mobility rGO-GFETs are not systematically lower than those obtained with exfoliated or CVD graphene with higher mobilities. In protein sensors, we also note that very low LODs (∼fM or lower) were obtained with all types of graphene. When keeping all other design parameters constant, some groups have reported a small improvement (one order of magnitude) in the LOD due to graphene type, for instance by changing from rGO to CVD [150] or from few-layer to monolayer graphene [129] ; yet such an effect appears eclipsed across multiple studies in which other design parameters are varied. Similarly, the area of the graphene surface has been mentioned as a potential influential parameter with respect to the LOD [1, 84, 109, 180], yet we could not observe a conclusive trend across the reported data.

Rather than graphene properties (type or area), we estimate that variations in the design and assembly of the bio-recognition interface are more likely to explain the large disparity in LOD between studies. As described in Sec. 2.2.4, there is a wide diversity in the probe molecules used for analyte capture, even for the same type of analyte, in their immobilization chemistry, as well as in blocking agents used to passivate sites around the probes. Additional strategies in the design of the interface have also been reported to enhance signal strength, such as the addition of protective layers [184] or addition of gold nanoparticles [7, 144]. Importantly, the detailed structure of the interface is often weakly characterized : in particular, the density of probe molecules on graphene is usually poorly controlled and often unknown, in large part because it is difficult to measure experimentally. In consequence, there is little quantitative knowledge on the correlation between interface design and the resulting LOD (or any other performance metrics). Better modeling of the interface properties (e.g. density and orientation of probes and blocking molecules, surface defects and impurities, distribution of surrounding ions in the media, analyte docking conformations and probabilities) and especially of their coupling with GFET electrical properties would be highly beneficial to optimize GFET sensors for analytical applications.

2.4.3. Replicas and Controls

In sensor experiments, the proper use of replicas and controls is essential to ensure the reliability of the results. The required number of replicas depends on two types of variability : intra- and inter-device variability. Intra-device variability represents the variation between repeated measurements on the same device. In particular, GFET electrical measurements often drift over time, especially until the equilibration of analyte-probe interactions and of ionic distributions after a change in media or applied electrical potentials. To take account of this, Campos *et al.* [24] repeated each measurement ten times to reach a stable state, and then kept the tenth curve as representative of the stabilized system. In a similar manner, Xu *et al.* [91] repeated five times each of their transfer curve measurements and used the average. Moreover, they repeated their experiments on 5 and 8 different devices to account for inter-device variability [217], allowing to assess of the reproducibility of results between sensors. Inter-device variability is inconsistently assessed in the literature, and when reported it's often with a limited number of devices, likely due to limitations in the scalability of fabrication and measurements. Some groups implemented fabrication methods to characterize GFET properties over hundreds of devices, enabling sensor experiments with ensembles of 15-30

active devices and 12-20 control devices [25, 77]. Such approaches based on large arrays of GFET sensors enable statistically-robust analyses of GFET performance, which is essential towards clinical and commercial applications. In general, methods for the characterization of both types of variability (intra- and inter-device) should be explicitely reported in GFET studies.

Another important aspect in experimental design is the use of proper positive and negative controls. Negative controls verify that the sensor gives no signal in absence of the specific probe :target pairing, which is important to validate the specificity of the assay to the targeted analyte. Oppositely, positive controls serve to validate that the sensor functions as expected, *i.e.* that a signal is detected in presence of the targeted analyte.

A common class of negative control consists in exposing probe-functionalized GFETs to non-specific analytes, *i.e.* species that are not the targeted analyte [26, 73, 77, 105, 142, 143, 145, 148]. It is particularly informative for specificity assessment to test sensors against molecules that are either similar to the targeted analyte (ex. DNA sequences with a few mismatches for DNA sensors) or expected to be present alongside the target in real biological samples. As examples, Kim *et al.* [148] exposed GFETs prepared with antibodies against Alpha-fetoprotein (AFP) to other protein biomarkers, specifically human chorionic gonadotropin (hCG) and carcinoembryonic antigen (CEA), and Islam *et al.* [26] exposed GFETs with anti-hCG probes to BSA proteins and small molecules glucose, uric acid and ascorbic acid. For the detection of small molecules such as the opioid naltrexone, authors used flumazenil as negative control, which is a similar compound known not to bind the immobilized receptors [77]. The same idea holds for bacteria : as control for *E. coli* detection, Huang *et al.* [73] used the unrelated specie *P. aeruginosa*, whereas Chen *et al.* [105] used *Listeria*. In the case of ion sensing, other ions are most of the time favored as negative controls [142, 143, 145], for example using Na^+, Ca^{2+}, Mg^{2+} and NH_4^+ as controls against K^+ ions [143]. In GFETs targeting DNA hybridization, the most common negative control is to test the sensors with DNA sequences non-complementary to the probe [24, 25, 71, 72, 81, 91, 184]. There are many possible variations of non-complementary sequences derived from the targeted sequence, going from a fully-non-complementary sequence to a very similar single-nucleotide mismatched sequence. Cai *et al.* [71] validated the specificity of their PNA-functionalized GFETs using both non-complementary and single-nucleotide mismatched sequences. Campos *et al.* [24] also used a single-mismatched sequence as negative control, and tested the response of their sensors to different concentrations of this control sequence. Other groups tested random one- and two-base mismatched DNA and studied how the position of mismatches affected the sensor response [25, 81].

In addition to non-specific analytes, it is also relevant to measure the response of the sensor to injection of blank media, in order to assess and eliminate signal due to solution exchange and related perturbations in ion distributions [78, 82, 83, 210]. For example, Zuccaro *et al.* [82] explicitly measured time series while injecting blank reaction buffer, to compare with injection of the same buffer containing the analyte : the first showed a small short-lived bump due to solution exchange, while the second showed a large, stable shift that can thus be assigned specifically to the analyte.

Another class of negative controls is to test the sensors against the targeted analyte, but without the appropriate probe, to ensure that the response is due to analyte :probe binding and not to

non-specific adsorption of the analyte on the sensor. Several groups have reported on the non-specific interaction of their targeted analyte with pristine graphene without probes [105, 145, 150]. A limitation of such experiments is that non-specific interactions of the analyte with the sensor surface are likely to be very different between pristine and probe-functionalized graphene. A strategy to better simulate the actual sensor surface is to prepare sensors with alternative probes having no affinity for the targeted analyte [10, 77, 83]. For instance, Lerner *et al.* [77] functionalized the surface of control sensors with scFv fragments of anti-HER2 antibodies, unspecific to the target nalodextrone, instead of the specific MUR μ-receptor. Similarly, Hajian *et al.* [83] prepared control sensors by loading a non-complementary single-guide RNA sequence in the dCas9 protein (instead of the complementary sequence). Such approaches enable control experiments with a sensor interface very similar to the regular experiment.

Positive controls are meant to validate that the sensor generates a signal if the analyte is present in the sample. The most common approach is to prepare calibration samples containing a known concentration of the targeted analyte. Most studies look for a dependence with analyte concentration to demonstrate that the measured signal is indeed due to the analyte. In such assays, target molecules are most commonly diluted in blank saline buffer [9, 10, 114, 141], sometimes with a calibrated mix of interfering species[81, 83, 109, 116, 142]. These calibration assays are usually presented as a proof of concept for the sensors, and they are sometimes used as positive controls before assays on cell culture samples [79, 84], clinical samples [7, 83, 145, 148, 159] or other environmental samples[74, 147], in which the concentration is either unknown or measured with another detection technique to compare results. For instance, Wang *et al.* [145] were the first group to measure the concentration of lead ions in real blood samples with GFET sensors, using a calibration with positive controls in buffer. GFETs results were found in good agreement with measurements by ICP-MS, confirming the potential of GFET technology for medical applications. For large analytes, some studies use imaging strategies to confirm by visualization the immobilization of the analyte on the GFET surface. As examples, Chen *et al.* [105] performed fluorescence microscopy, scanning electron microscopy (SEM), and atomic force microscopy (AFM) to visualize the capture of *E. coli* bacterial cells onto the surface of functionalized GFET devices, and Xu *et al.* [180] used DNA probes labelled with Cy3 or Cy5 fluorophores to correlate the electrical response of GFETs with fluorescence measurements.

2.4.4. Response time

An important practical aspect of sensor performance is the test duration, *i.e.* the time required to obtain the result of an analysis. For a given sensor technology, estimating this metric is critical to identify potential applications and to determine how the sensors will be packaged, deployed and used. GFETs are often praised as fast detection tools [81, 82, 144, 218], however there is often a lack of clarity as to which steps of their operating protocol are included in this assessment. Specifically, the process of analyte detection or quantitation using GFETs usually require several steps : sample injection, incubation, washing, all repeated for a number of replica and controls. The duration of each of these steps can be informed by real-time measurements with time series. In particular, the

response time, *i.e.* the time required for the signal to stabilize after injection of the sample, or after its washing away, can be extracted from time series. Independently of analyte binding kinetics, part of the response time comes from the basal response of the sensor to perturbations in the medium when injecting/washing the sample or changing applied electric potentials. It is possible to assess this contribution to the response time by changing abruptly the gate voltage and measuring the response of electrical metrics in time series [89].

Response times reported for GFETs in the literature vary significantly between experiments, even for similar analytes. For ions, response times are usually small, from almost instantaneous [79, 146, 147] to approximately 100 seconds [68]. For proteins, there is a wider variability : for example, Lei *et al.* [195] recorded signal reaching a plateau 10 s after insertion of the analyte brain natriuretic peptide, whereas Kim *et al.* [70] assessed a response time to the prostate antigen PSA of approximately 10 minutes. For DNA hybridization, most studies focus on quantitation experiments using before/after measurements. Incubation times between the two are typically long to maximize hybridization density : from 30 minutes [25, 183] to many hours [72]. Outside that range, Hajian *et al.* [83] reported a detection of 1.7 fM in 15 minutes, due to the dCas9 system which actively improves the processing of DNA strands in the sample. The experimental process used to determine these incubation times is seldom described and likely to be based on trial and error, although a few real-time experiments have looked specifically at hybridization and denaturation kinetics [81, 85]. Some groups notice a significant variation of the response time with target concentration [81, 85], such as observed by Xu *et al.* [81] in Fig. 2.2h. Others define the response time as the time required to reach current saturation in all tested concentrations, in order to determine an incubation time independent of target concentrations [10, 70]. Finally, continuous flow settings appear a promising solution to minimize incubation times, as they report faster response times than standard configurations based on injection followed by static incubation periods. With a 30 μL/min flow, Stine *et al.* [157] reported a saturation of signal in less than 800 seconds for the hybridization of fully complementary ssDNA targets at 1μM concentration. Xu *et al.* [81] obtained a stabilized hybridization signal in less than a minute for the same target concentration at 60 μL/min flow.

2.4.5. Other considerations

Depending on which applications are targeted for the GFET biosensors, numerous practical issues are important to consider in assessing their suitability and potential performance. Here, we merely raise some of the considerations that have been explored in the development of GFET sensor technology. Scalable production is an important aspect towards commercialization, in order to achieve competitive production rates and costs : scalable processes for GFET assembly have been developed, usually based on CVD synthesis techniques [25, 219]. Reusability, *i.e.* the possibility to make successive analyses on the same device, as well as shelf life of the sensors are other important parameters in technology maturation, and have been tested in some recent studies. For example, reusability has been tested by Wu et al. [7] by performing successive binding-unbinding cycles with the target and measuring the evolution in the strength of signal, finding a conservation of signal

of 94% when comparing the first to the last cycle. Some groups also made assessments of shelf-life by measuring the drift of current over time for multiple concentrations of target [143] or by repeating experiments after storage time [92]. Reported shelf-life values vary from one week [77] to a few months [143, 178]. The use of flexible substrates is also an ongoing area of investigation for wearable or skin-implanted devices, for example to detect glucose levels in sweat directly on the skin [181] or for other health-monitoring purposes [220]. Silk fibroin [116], paper substrates [117, 220] or polymide [181] have been successfully tested as flexible substrates.

2.5. Conclusion

Graphene field-effect transistors have demonstrated promising performance as bioanalytical sensors, including low limits of detection and fast response times in a miniature footprint. Their core feature is the use of graphene conductance as transducer, which provides high sensitivity to the capture of biomolecular species at its surface due to its extreme monoatomic thinness. For the past decade, GFET sensors have been prototyped for a wide variety of biologically-relevant analytes : ions, small molecules, nucleic acids and proteins. We reviewed this literature to discuss best practices in sensor assembly, experimental design and performance assessment, in particular towards the detection, quantitation and kinetic analysis of biomolecules.

In sensor design, the type of graphene (exfoliation, CVD, rGO) does not appear as a dominant factor for performance : very low LODs have been reported for high- and low-quality graphene. Two more critical features are the configuration of the gate electrode and the assembly of the biorecognition interface : both would benefit from better modeling of their effect on graphene conductance transduction. In particular, the specifics of the surface chemistry (e.g. coverage, orientation, stability of immobilized probes, blocking species and captures analytes, and their respective interactions) are often not well known or controlled. On the other hand, limitations due to media screening appear well-understood and modeled by the Debye length, and strategies have been successfully proposed to increase the range of detection. The transduction of analyte capture in electrical conductance can appear as a change in the density of charge carriers by doping (*i.e.* shift of the charge neutrality point), in the scattering processes (*i.e.* change in the transconductance), or a combination of them. Transfer curves, alone or combined with time series, are the most appropriate way of studying the physics of this interaction. Some interrogations remain about the coupling mechanism between analyte capture and the graphene, as shown by the diverging CNP shift polarities reported for similar analytes. Time series of electrical current alone are not sufficient to interpret interactions mechanisms, but they can provide a robust empirical assessment of target presence or quantification, and they are essential for kinetic studies. Two-dimensional time series combining gate voltage and time sweeps provide both mechanistic and kinetic information in the same measurement. In all cases, in order to produce a reliable and reproducible experiment, intra- and inter-device variabilities need to be assessed and managed using sufficient replicas and appropriate controls. Finally, scalability and cost of fabrication, electronics and fluidics packaging for practical use with samples, as well as

reproducibility and stability of the sensor response are important aspects to optimize in order to move the technology forward.

Chapitre 3

Optimisation des systèmes expérimentaux

Dans la revue de littérature précédente, nous avons établi ce qui compose un bon protocole de détection : une caractérisation adéquate de la variabilité intra- et inter-dispositifs, des contrôles appropriés et une bonne combinaison des différentes mesures électriques (courbes de transfert, courbes de sortie, séries temporelles). Dans ce chapitre, nous développons les outils nécessaires à l'exécution d'un tel protocole. En première partie, nous aborderons le problème de la fabrication des dispositifs, dont le faible rendement limite la quantité de réplicats disponibles. Le protocole de fabrication ainsi que les modifications menant à une amélioration du rendement seront détaillés. Deuxièmement, nous nous pencherons sur les limitations du système de mesure, ne permettant de mesurer qu'un dispositif à la fois. Nous décrirons le développement et la performance d'un nouveau système de mesures électriques permettant l'acquisition de données en parallèle pour plusieurs transistors.

3.1. Fabrication des dispositifs

Les transistors, aussi appelés dispositifs ou capteurs dans ce mémoire, sont répartis sur des puces, dont une image est présentée à la Fig. 3.1a. Une puce mesure 1 cm^2 et est composée d'un substrat de silicium dopé dégénérativement couvert par 300 nm de dioxyde de silicium (SiO_2). Le substrat de Si et l'épaisseur de SiO_2 ont été choisis afin de favoriser l'effet d'interférence permettant d'observer le graphène par microscopie optique sur de tels substrats [221]. Sur la puce, on trouve seize paires d'électrodes (① de la figure 3.1b), terminées par des patins de mesure, où seront déposées les sondes électriques de source et de drain lors des mesures électriques (② de la figure 3.1b). Les paires d'électrodes sont reliées en leur centre par un ruban de graphène dont la partie active agissant comme la chaine de conduction du transistor est de 6 μm de largeur par 4 μm de hauteur. Leur emplacement est montré au ③ de la figure 3.1b et une image optique est présentée à la figure 3.1d. Comme illustré dans la partie ④ de la figure 3.1b, une grille coplanaire encercle les transistors (en violet). On appliquera un voltage sur cette grille lors des expériences en solution, ce qui permettra de moduler le courant comme expliqué dans la section 1.2. La configuration des puces présentée ici a été conçue par Amira Bencherif, Claudia M.Bazán et Monique Tie. Le protocole de fabrication présenté dans ce chapitre a été développé conjointement

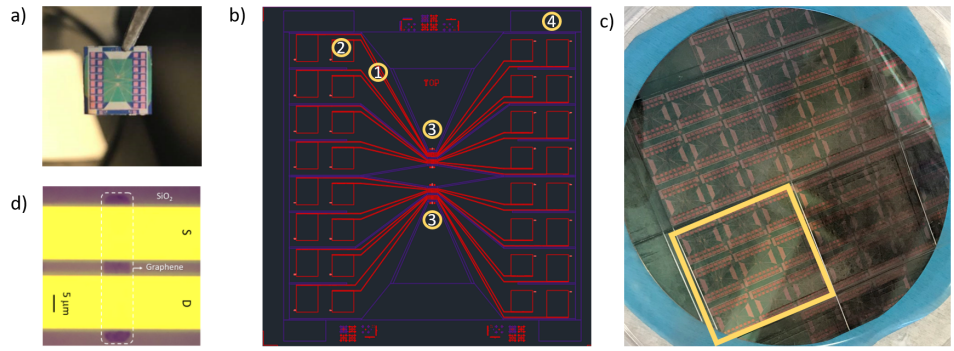

Figure 3.1 – a) Photographie d'une puce à 16 transistors. b) Plan de conception d'une puce à 16 transistor. Les parties en rouge sont ① Les électrodes. ② Les patins de mesure. ③ L'emplacement des électrodes où se trouvent les rubans de graphène. Les lignes violettes représentent ④ la grille coplanaire. c) Photographie d'une gaufre de silicium circulaire. Elle est divisée en quatre plaquettes de 9 puces chacune (encadrée en jaune), pour un total de 36 puces individuelles. d) Image au microscope optique d'un transistor. Au milieu se trouve le ruban de graphène, faisant le pont entre l'électrode de source (S) et l'électrode de drain (D).

par Delphine Bouilly, Amira Bencherif, Claudia M. Bazán et moi-même au cours des dernières années, à l'exception du montage de transfert développé par Monique Tie. La croissance du graphène utilisé pour les travaux de ce mémoire a été faite par Amira Bencherif ou Claudia M. Bazán. Une partie du graphène a également été achetée chez Graphenea. En janvier 2020, j'ai pris en charge la fabrication des puces avec l'objectif de régler les deux plus grands problèmes de notre processus : le faible rendement de dispositifs fonctionnels par puce (qui était à 32,5% de dispositifs fonctionnels par puce, évalué sur 17 puces fabriquées par Claudia M. Bazán) et le manque d'uniformité et de suivi de la fabrication. Dans les prochains paragraphes, je présenterai le protocole de fabrication ainsi que les principales modifications et mesures de suivi que j'y ai apporté. Je tiens à remercier Christophe Clément et Marie-Hélène Bernier pour leur précieux conseils à ce sujet.

Avant toute chose, j'ai implanté une convention d'appellation permettant de connaître la provenance des puces tel qu'illustré à la figure 3.2a (le X suivant le WAF_ indique le numéro de la gaufre circulaire). Chaque sous-plaquette de neuf puces est numérotée et est suivie tout au long du processus pour faciliter le traçage des puces tout au long des expériences. Pour systématiser les rapports de fabrication, j'ai développé un gabarit de protocole facile d'utilisation pouvant être rempli en ligne. Ce modèle établit clairement quels paramètres doivent être rapportés et quelles vérifications doivent être menées. Ce gabarit permet aussi de rapporter tout évènement anormal.

La fabrication suit le flux de travail présenté à la Figure 3.3. Nous commencerons par décrire la préparation du substrat, puis celle du graphène, pour finir par le transfert et les étapes subséquentes.

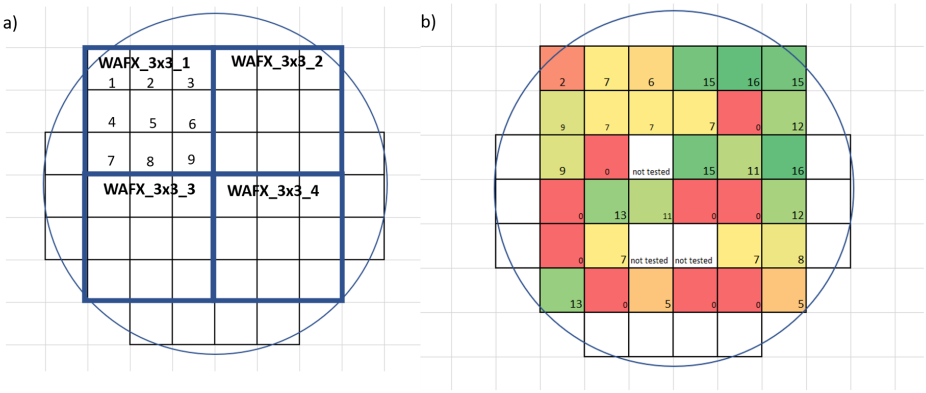

Figure 3.2 – a) Schématisation de la gaufre circulaire de silicium avec la convention de nomenclature. b) Représentation visuelle du rendement des puces en fonction de leur emplacement dans la gaufre de silicium à l'aide d'une carte thermique.

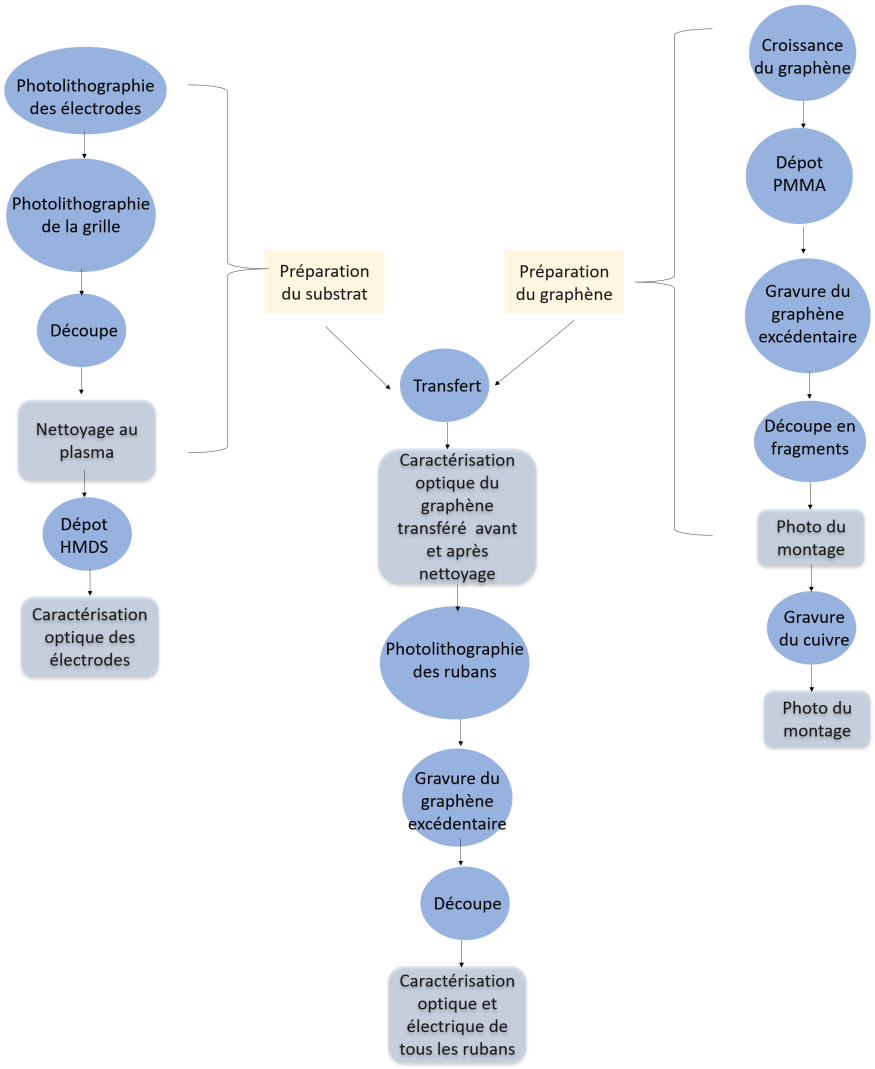

Figure 3.3 – Flux de travail pour la fabrication des transistors de graphène produits et utilisés dans ce mémoire. Les étapes dénotées par un rectangle gris ont été ajoutées au protocole initial suite à mon travail d'optimisation.

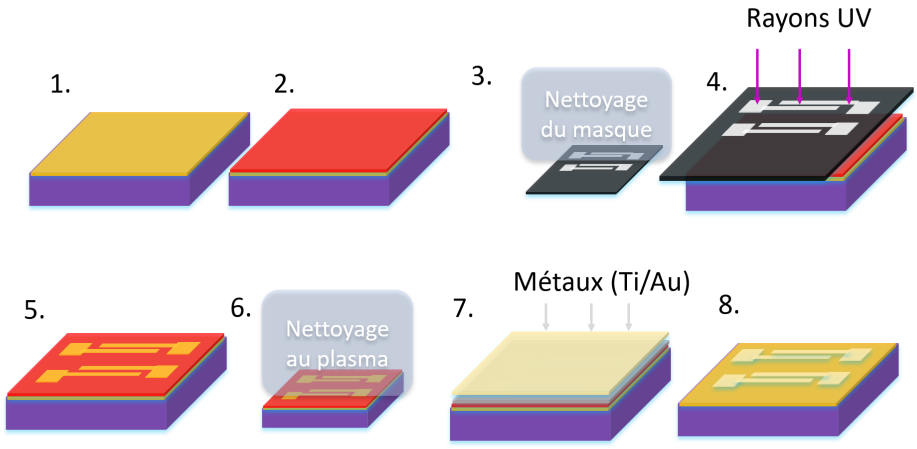

Figure 3.4 – Fabrication des électrodes par photolithographie et métallisation. La grille est fabriquée suivant les mêmes étapes. Les rubans de graphène sont formés suivant les étapes 1-6. (1) Le substrat est vierge. (2) Le substrat est couvert d'une résine photosensible à la tournette. (3) Le masque est nettoyé. (4) Le substrat est exposé aux rayons UV au travers du masque. (5) La résine exposée est dissoute par procédé chimique. (6) Le substrat est nettoyé au plasma. (7) Le métal est évaporé sur le substrat. (8) La résine est dissoute chimiquement, emportant avec elle le métal n'étant pas en contact direct avec le substrat.

Les étapes reliées à la préparation du substrat de silicium sont faites en salle de microfabrication et à l'échelle de la gaufre circulaire de silicium (voir figure 3.1c). La première étape est la fabrication des électrodes par procédé de photolithographie et de métallisation. Ceci est illustré à la Figure 3.4. Le métal adhérant très bien sur le SiO_2, la photolithographie, par un principe analogue à celui du dessin au pochoir, permet grâce à un masque de chrome et à une résine photosensible d'exposer le substrat uniquement à l'emplacement des électrodes. Le substrat est d'abord vierge (1). Il est ensuite couvert de résine par un procédé à la tournette (2). Le masque de chrome est nettoyé (3) pour empêcher la saleté d'entraver les rayons UV qui passeront au travers, ce qui altérerait les formes qui seront imprimées sur le substrat. Les étapes notées par un rectangle gris dans les Figures 3.3 et 3.4 ont ajoutées au protocole par mes soins. Lorsque la résine est exposée aux rayons UV aux endroits ouverts dans le masque de chrome (4), elle devient solvable par une solution chimique, qui expose le substrat à ces endroits stratégiques (5). On nettoie assidûment la surface (6) avant d'évaporer le métal des électrodes par faisceaux d'électrons (7) pour assurer une adhésion optimale du métal au substrat. Le métal est évaporé sur l'entièreté de la gaufre, puis la résine est dissoute par un procédé chimique, ne laissant du métal qu'aux endroits où il a été déposé directement sur le Si/SiO_2 (8). Les électrodes sont composées d'une fine couche d'adhésion de titane suivie d'or, un métal noble choisi pour son insensibilité à l'oxydation [222]. Une fois les électrodes terminées, les mêmes étapes sont répétées pour la grille avec une couche d'adhésion de titane, puis une couche de platine. Les deux

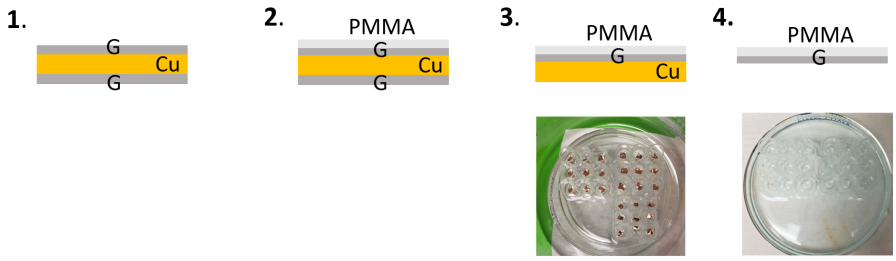

Figure 3.5 – Procédé de préparation du graphène au transfert. (1) Le graphène est cru sur cuivre, la croissance a lieu des deux côtés de l'échantillon. (2) De la résine PMMA est appliquée à la tournette sur un coté du cuivre. (3) Le cuivre est gravé du côté opposé au PMMA, puis découpé en fragments et posés du côté cuivre dans de l'ammonium persulfate, alignés dans des tubes en verre (photo). Les fragments sont incubés une nuit. (4) Le cuivre est complètement gravé par le persulfate d'ammonium. Les fragments sont prêts à être transférés (photo). Photographies par Monique Tie.

structures sont construites séparément principalement à cause de leur différence d'épaisseur. La différence d'épaisseur est importante car celle des électrodes doit être minimisée afin de limiter la déformation des rubans, qui seront posés directement dessus, alors que la grille doit être épaisse pour s'assurer de sa robustesse. Le graphène n'est pas disposé en-dessous des électrodes, bien que cela permettrait des rubans parfaitement plats, à cause de problèmes d'adhésion des rubans au substrat lors des étapes suivant la métallisation. Une fois la grille et les électrodes complétées, la gaufre circulaire est découpée en quatre plaquettes de 9 puces à l'aide d'une scie de découpe (encadré en jaune à la Fig. 3.1c). La découpe étant un processus salissant, la surface des plaquettes est nettoyée chimiquement et par plasma d'oxygène. Il est très important que la surface du substrat soit parfaitement propre avant le transfert, puisque des saletés en dessous des rubans de graphène pourraient en altérer les propriétés, voir en empêcher le bon fonctionnement. Une fois les plaquettes propres, une couche d'hexaméthyldisilane (HMDS), un composé chimique permettant d'augmenter l'adhérence du graphène au substrat, est évaporée. Une étape de caractérisation optique individuelle de toutes les électrodes a également été ajoutée afin d'identifier facilement si la fabrication mérite d'être poursuivie (un transistor ne peut fonctionner si une électrode est sectionnée). Je note aussi que toutes les étapes de nettoyage ont été révisées pour terminer par un rinçage à l'eau et éviter la contamination fréquente des dispositifs mal séchés à l'isopropanol.

La préparation du graphène est schématisée à la Figure 3.5. La croissance du graphène utilisé dans le présent mémoire est faite par déposition chimique en phase vapeur, ou *CVD*. Cette méthode a été choisie car elle est peu coûteuse, le graphène est transférable sur un autre substrat suite à la croissance et elle génère du graphène de qualité suffisante sur de grandes surfaces [106]. Pour ce faire, du méthane est évaporé dans une chambre de quartz chauffée à $\sim 1000°C$, entraînant la dissociation des atomes de carbone, puis leur recombinaison suivant la forme alvéolée caractéristique du graphène sur des substrats de cuivre préalablement nettoyés [223, 224]. L'objectif de cette préparation est d'obtenir le graphène directement posé sur les puces, sans

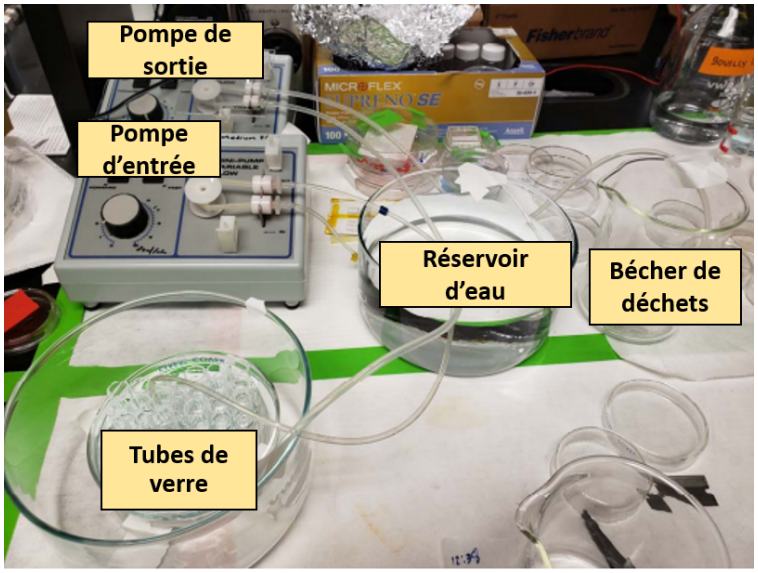

Figure 3.6 – a) Photographie du montage de transfert. De l'eau est pompée du réservoir d'eau jusqu'au plat où se trouvent les tubes de verre. Simultanément, le persulfate d'ammonium est pompé à l'extérieur du plat au même rythme pour être envoyé dans le bécher de déchets. Photographies par Monique Tie.

la couche de cuivre. Lors de la croissance, les atomes de carbone se réorganisent des deux côtés de l'échantillon de cuivre (1). On commence par appliquer une couche de résine PMMA d'un côté (2), puis on grave le graphène résiduel du côté opposé par plasma d'oxygène (3). Ainsi, le cuivre est exposé d'un côté, et nous pourrons le dissoudre en l'incubant au persulfate d'ammonium, qui n'attaque pas le graphène. Pour ce faire, le cuivre est coupé en fragments de quelques millimètres carré, disposés dans des tubes en verre et incubés du côté du cuivre exposé (voir la photographie de l'étape 3). Ainsi, après l'incubation, nous possédons des fragments de graphène couverts de résine, prêts à être déposés sur des plaquettes de neuf puces (4). On passe ensuite à l'étape la plus délicate du processus : le transfert.

Pour transférer les petits morceaux de graphène sur les puces, les plaquettes de neuf puces sont disposées en dessous des tubes de verre. Puis nous procédons au rinçage du persulfate d'ammonium à l'aide d'un système de pompage le remplaçant par de l'eau pure (voir 3.6). Une fois les morceaux de graphène rincés, l'eau est retirée par ce même système de pompage, s'assurant que les morceaux de graphène soient alignés avec le centre des dispositifs sur les puces. Les fragments sont déposés dans des tubes en verre pour favoriser l'alignement avec les neuf puces des plaquettes. Une fois les morceaux de graphène et de PMMA déposés sur les puces, la couche de résine est dissoute chimiquement. Le graphène est caractérisé optiquement avant et après cette étape pour en vérifier l'alignement et la propreté. Le transfert est l'étape la plus sensible de la fabrication car en plus d'être une forte source potentielle de contamination, il est très délicat de manipuler le graphène car la tension mécanique en affecte les propriétés [225, 226]. Plusieurs problèmes compromettent fréquemment l'exécution du transfert : les petits morceaux

de graphène peuvent être pliés lors du découpage, résultant en une gravure inhomogène du cuivre, ils peuvent se retourner lorsqu'on les dépose dans les tubes (mettant le PMMA en contact avec le persulfate d'ammonium au lieu du cuivre, ce qui empêche la gravure du cuivre), se dissoudre complètement si le PMMA n'est pas uniforme, se coller sur les parois des tubes et se déchirer lorsque l'eau est vidée, ou encore ils peuvent se déposer ailleurs que sur la partie des électrodes supposée accueillir les rubans. Afin d'améliorer le rendement du transfert, la première étape est de bien le documenter. C'est pourquoi plusieurs étapes de référence ont été ajoutées.

Une fois le graphène transféré, nous passons à la troisième étape de photolithographie qui permet de donner la forme aux rubans de graphène, comme on les voit dans la figure 3.1d. Une fois que les rubans ont été protégés par la résine avec la forme désirée, on passe les échantillons en gravure au plasma d'oxygène pour retirer tout le graphène excédentaire. La résine est retirée des rubans par procédé chimique, suite à quoi les rubans de graphène sont caractérisés visuellement afin d'en assurer la propreté. La dernière étape consiste à découper les plaquettes en puces individuelles et à les nettoyer. J'ai finalement ajouté une caractérisation optique et électrique complète de chaque dispositif. Ces protocoles de caractérisation permettent d'avoir une vision d'ensemble du rendement des puces en fonction de leur positionnement dans la gaufre de silicium. Le rendement des puces est ensuite répertorié avec un carte thermique comme à la figure 3.2b.

Au total, suivant le protocole modifié, 250 dispositifs fonctionnels ont été produits, avec un rendement à 60% de dispositifs fonctionnels par puce et à 76% de puces fonctionnelles par plaquette de 9 puces. Le rendement initial de 32,5% de dispositifs fonctionnels par puce est presque doublé, ce qui représente un bon point de départ et démontre une amélioration significative, mais notons qu'il laisse encore place à l'amélioration. L'optimisation du protocole de fabrication est un processus itératif et continu qui continuera d'être peaufiné dans les années à venir. Les détails expérimentaux de la version actuelle du protocole sont donnés dans les premières sous-sections de la section B, le *Supporting Information* du deuxième article. Les modifications principales apportées au protocole sont axées sur le nettoyage des surfaces, qui permettent à la fois d'éviter la contamination et d'augmenter la précision de fabrication. Afin d'améliorer le suivi de la fabrication (qui permet d'augmenter la performance et qui favorise la transmission des connaissances), des gabarits indiquant les paramètres pertinents à répertorier et incluant de nombreuses étapes de caractérisation ont été développés et sont utilisés à ce jour par les membres du laboratoire.

3.2. Développement d'instrumentation

3.2.1. Ancienne instrumentation

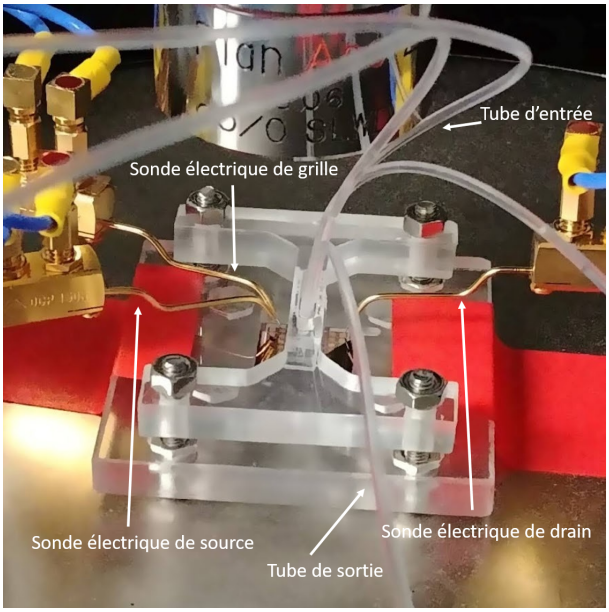

Figure 3.7 – Photographie de l'ancien montage de mesure. Des sondes électriques de source, de drain et de grille sont alignées manuellement avec les électrodes de source, de drain et la grille respectivement. Une cellule de flux est fixée en place à l'aide d'un support conçu et imprimé avec une imprimante à trois dimensions. Un système de tubes d'entrée et de sortie avec une seringue permet l'insertion de solutions. Adaptation d'une image par Claudia M.Bazán.

L'instrument de mesure le plus largement utilisé dans le domaine des TECG est la station de mesures sous pointes, où de fines pointes métalliques sont manuellement alignées aux patins de mesures associés des électrodes de source et de drain du dispositif à mesurer (voir la figure 3.7). On utilise un système de mesures à deux pointes pour la simplicité du montage. Un système de mesures à quatre pointes serait approprié pour détecter de plus petits changements de résistivité en s'affranchissant de la résistance de contact [227], ce qui n'est pas nécessaire pour la mesure des TECG bioanalytiques. Ces pointes étant reliées à une unité de mesure et de source (*SMU*) : un voltage est appliqué à chaque extrémité, créant une tension entre la source et le drain du transistor, et le courant résultant est simultanément mesuré et enregistré. Une autre pointe métallique est alignée avec la grille, à laquelle on applique un voltage qui sera le voltage de grille. La puce est posée sur un support métallique, ce qui permet également d'appliquer un voltage de grille arrière. Une cellule de flux peut également être fixée vis-à-vis les capteurs grâce à un support, conçu et fabriqué par Claudia M. Bazán. Une cellule de flux est un petit réceptacle en polymère dans lequel sont moulés des canaux qui permettent d'exposer les capteurs à de très petits volumes de solution (quelques microlitres dans notre cas). C'est dans ces canaux qu'ont lieu les différentes réactions chimiques et biologiques. On y insère les solutions avec un système de seringues. Cette plateforme de mesures

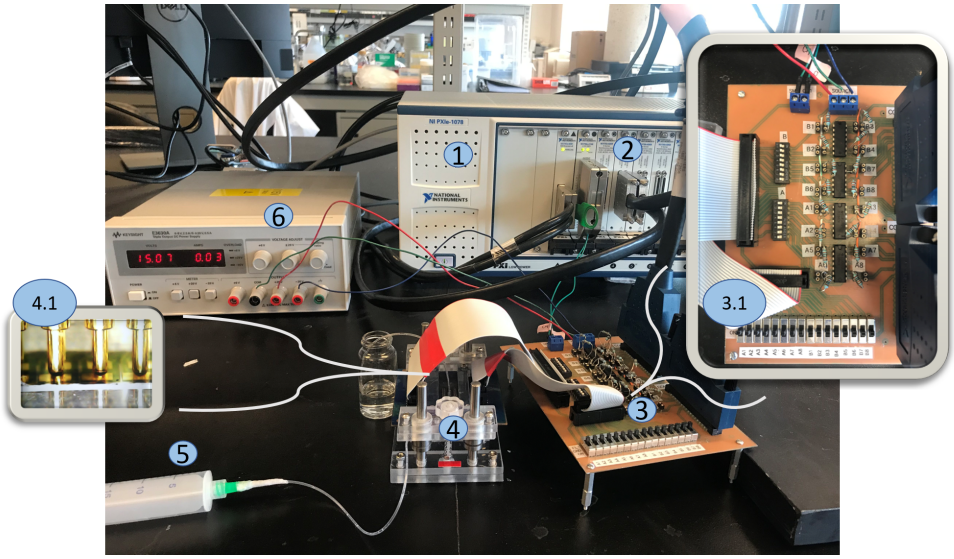

Figure 3.8 – Montage expérimental complet. ① : chassis du PXI. ② : différents modules du PXI. ③ : circuit intermédiaire, avec un agrandissement du circuit imprimé en 3.1. ④ : porte échantillon qui contient la puce. En 4.1 se trouve une agrandissement des sondes à broches. ⑤ : système de seringues qui permet d'injecter du liquide dans la cellule de flux. ⑥ : source d'alimentation en courant continu.

électriques, bien que fonctionnelle, est problématique à plusieurs niveaux de productivité. En effet, puisque les réactions chimiques et biologiques se déroulent dans la cellule de flux couvrant toute la puce, les capteurs sont soumis à la réaction simultanément. Mais puisqu'il n'y a que trois sondes sur l'appareil, dont une pour la grille, la mesure est limitée à un dispositif à la fois. Il est possible de passer automatiquement d'un dispositif à l'autre, mais cela prend un certain temps. Ceci pose une série de problèmes : 1- Cela limite drastiquement le nombre de réplicats possibles puisque le délai de mesure entre le premier et le dernier sera obligatoirement de plusieurs minutes. 2- Cela empêche de prendre des mesures en temps-réel sur plus d'un dispositif à la fois. 3- Il n'est pas possible de connecter les dispositifs non-mesurés à la masse, ce qui peut être un enjeu dans certains types d'expérience de détection. D'autres problèmes sont posés par ce montage expérimental. Premièrement, un enjeu de qualité se pose dans les séries temporelles : la quantité d'information extraite est limitée par la mémoire de l'instrument, il n'est pas possible de mesurer l'évolution temporelle du courant avec une grande vitesse d'acquisition pendant une longue période de temps. Finalement, on ajoute des considération ergonomiques et pratiques. En effet, la disposition du montage complique certaines manipulation comme l'injection de solutions et ne favorise pas l'innovation des protocoles par l'ajout d'instrumentation pour contrôler différents paramètres (injection, température de la solution, etc.) Malgré ses désavantages, précisons que ce montage demeure approprié pour certaines utilisations, par exemple celles nécessitant de grandes résolutions, mais qu'un nouveau système de mesure électrique s'impose pour le type d'expériences qui sont présentées dans ce mémoire.

3.2.2. Nouvelle instrumentation

Les besoins scientifiques à combler par le nouvel appareillage de mesures électriques sont les suivants :

(1) Qualité des trois mesures électriques essentielles : capacité de prendre des courbes de sortie mesurant adéquatement la résistance aux contacts, des courbes de transfert stables et des séries temporelles peu bruitées.

(2) Parallélisation et contrôle des mesures : permet de mesurer tous les dispositifs d'une puce (16) simultanément afin d'obtenir un plus grand nombre de données rapidement et de caractériser plus fidèlement la variabilité entre les capteurs en fixant le temps comme paramètre. Le contrôle des mesures réfère à la possibilité de mesurer ou non un dispositif.

(3) Résolution et longueur des séries temporelles : une meilleur vitesse d'échantillonnage permet de faire des expériences plus précises afin d'étudier des événements très rapides et une grande mémoire d'entreposage permet de prendre des mesures de longue durée sans compromettre la qualité de l'acquisition.

(4) Synchronisation de la prise de données et de l'application des voltages : permet de mener des expériences de plus grande précision, particulièrement lorsqu'on tente de comprendre des mécanismes dynamiques.

(5) Montage modulaire : permet d'ajouter des éléments d'instrumentation supplémentaires en fonction des besoins. Nous visons un montage maniable, pratique et facilement adaptable.

Le système identifié comme répondant à tous ces critères se nomme le *PXI* (PCI eXtensions for Instrumentation), produit par *National Instruments*. L'instrument est constitué d'un châssis (① dans Fig. 3.8) synchronisant plusieurs modules de haute-performance (identifiés par ② dans la figure 3.8). Le *PXI* est relié à un ordinateur ultra-performant, ce qui permet à la fois d'écrire des codes contrôlant les modules et d'entreposer les données récoltées par ces derniers. Le langage de programmation utilisé par le *PXI* est *LabView*, un langage graphique facilitant la programmation d'interfaces conviviales. Les modules disponibles sont variés et adaptables aux besoins. Notre laboratoire possède six modules : quatre modules d'acquisition de données multifonction (DAQ, PXI-6358), un module de mesure et de source 4 chaines (SMU, PXI-4140) et une matrice de multiplexage (PXI-2530B). Le module d'acquisition de données lit et produit des voltages. Chaque module possède 16 chaines d'entrée, donc a le potentiel de lire une puce. Le montage présent n'en lit qu'une seule, mais il serait facile d'en lire quatre à la fois. Le SMU peut lire et produire des voltages simultanément. La matrice de multiplexage peut rediriger plusieurs entrées de signal à une seule sortie, mais n'est pas utilisée dans le montage actuel.

La première étape fut d'interfacer l'ordinateur avec les modules du PXI. La deuxième, d'interfacer nos puces. L'idée originale est venue de Monique Tie : la puce est fixée sur un support et le courant est lu par des sondes à broches qui sont pressées sur les patins de mesure à l'aide de vis. Un prototype a été d'abord construit par cette dernière, puis une version plus définitive a été

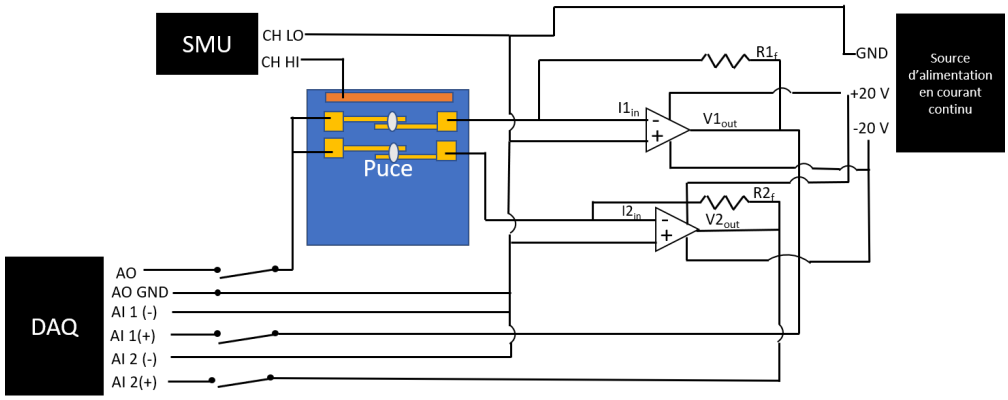

Figure 3.9 – Schéma du circuit complet pour deux dispositifs sur une puce. Le circuit réel en comporte 16. L'entrée positive du SMU est connectée à la grille de la puce, son entrée négative à la masse du système. Le DAQ produit le voltage de drain avec sa sortie analogue. Le courant provenant du dispositif est inversé et amplifié par un amplificateur opérationnel et une résistance parallèle externe. Le volage résultant est lu par les entrées analogues du DAQ. Des interrupteurs permettent de connecter le dispositif à la masse ou de le déconnecter complètement, le rendant flottant.

construite par Claudia M. Bazán (voir ④ dans Fig. 3.8 et (4.1) pour un agrandissement du système de sondes à broches). Cette version comporte un porte-échantillon en acrylique gravé pour soutenir la puce et un circuit imprimé où des sondes à broches sont soudées et connectées par le circuit à des connecteurs de cables plats. Pour la conception globale du montage, particulièrement pour le circuit ③ relayant le courant lu sur la puce au *PXI*, je remercie Jean-Pierre Martin et Monique Tie pour les précieux échanges. Toutes les étapes de tests des modules, de développement du circuit, interface avec le *PXI* et d'écriture des codes de courbes de sortie, de courbes de transfert et de séries temporelles ont été menées par mes soins, sur des plaques sans soudures connectées par des fils individuels. Une fois arrivée à une configuration optimisée, une version définitive du circuit d'amplification a été construite par Claudia M. Bazán et est présentée en ③ et (3.1) de la figure 3.8.

Une schématisation du circuit est illustrée à la figure 3.9. Le carré bleu représente la puce avec en jaune, les électrodes de source/drain et en orange, de grille. Les rubans gris représentent le graphène. Ce schéma présente deux dispositifs à titre d'exemple, mais le circuit réel est composé de 16 capteurs. Le voltage de grille est fourni par une des quatre chaines du SMU entre le côté positif (CH HI) connecté directement à la grille de la puce et le côté négatif (CH LO) connecté à la masse du système, située sur la source d'alimentation de courant continu. La différence de potentiel entre la source et le drain est maintenue d'un coté par un voltage généré par la sortie analogue du DAQ (AO) et de l'autre par une connexion à la masse du système. Tous les dispositifs sont soumis au même voltage du même AO. Pour la lecture du courant des dispositifs, le module d'acquisition de données possède 16 entrées analogues (AI). La différence de potentiel entre l'entrée positive (AI+) et l'entrée négative (AI-) est convertie en une valeur digitale. Le courant sortant des dispositifs doit

donc être converti en voltage. Afin de pouvoir être lu par les AI, le voltage doit également être amplifié. C'est ce qui est fait par le circuit d'amplification renversée, composé d'un amplificateur opérationnel et d'une résistance parallèle externe (R_f). Le AI- est connecté à la masse et le AI+ est connecté à la sortie de l'amplificateur. Sachant les deux règles d'or d'un amplificateur opérationnel (aucun courant ne circule dans son entrée positive et le voltage différentiel entre les entrées positives et négatives est nul [19]), on peut facilement calculer que le courant entrant est amplifié par R_f selon l'équation suivante :

$$I_{in} = -V_{out}/R_f \tag{3.1}$$

où V_{out} est le voltage de sortie mesuré par le DAQ et I_{in} est le courant entrant dans l'amplificateur. Ainsi, en mesurant la différence de potentiel entre AI+ et AI-, on peut calculer quel courant a été produit par le dispositif. Notre montage nous permet aussi de connecter les dispositifs à la masse ou de les rendre complètement flottants (en déconnectant les interrupteurs). La valeur de la résistance R_f doit être choisie pour amplifier le signal produit par la puce tel qu'il soit détectable, sans qu'il ne dépasse la valeur maximale pouvant être lue par le DAQ. Pour la choisir, il est donc nécessaire de connaître la gamme de courant généré par nos transistors et le voltage maximal permis par le DAQ. Nos TECG produisent des courant généralement entre 1×10^{-6} A et 1×10^{-4} A. Le DAQ peut être configuré pour lire des courants entre ± 1 V, ± 2 V, ± 5 V ou ± 10 V. La résolution du module (plus petit changement de voltage générant un signal) est déterminée par le choix de cette gamme. La valeur fixe de résolution de l'appareil est de 16 bits, qui divise la gamme de voltage choisie en $2^{16} = 65536$ étapes. La plus petite résolution possible est alors de $2V/65536 = 30{,}5\ muV$ et la plus grande $20V/65536 = 305\ muV$. Pour nos besoins, la plus grande nous suffisait. Conséquemment, la résistance choisie est de $R_f = \frac{V_{max}}{I_{max}} = \frac{10V}{1 \times 10^{-4} A} = 100$ kΩ. Celle-ci peut être ajustée en fonction des besoins.

3.2.3. Performance

Nous évaluons la performance du montage par la qualité des mesures qu'il produit. En étudiant les trois mesures possibles (courbes de sortie, courbes de transfert et séries temporelles), nous caractérisons à la fois certaines propriétés de l'instrumentation et des dispositifs fabriqués à la section 3.1.

Les courbes de sortie permettent d'évaluer la qualité des contacts entre les sondes de mesure, les électrodes et le graphène [192, 193]. La figure 3.10 présente trois courbes de sortie ainsi que la valeur de la résistance extraite par ajustement de courbe. Un comportement linéaire stable (sans bruit apparent) tel qu'observé dans la figure témoigne de contacts ohmiques de bonne qualité dont la mesure de la pente permet d'obtenir la résistance de contact (en série avec celle du graphène) par la loi d'Ohm. Les résistances obtenues de moins de 10 kΩ, confirmées par mesure manuelle au multimètre à $0{,}01 k\Omega$ près, indiquent un montage de bonne qualité sachant qu'une bonne résistance de contact est de l'ordre de 1 kΩ, mais peut aller jusqu'à ~ 100 kΩ [228, 229].

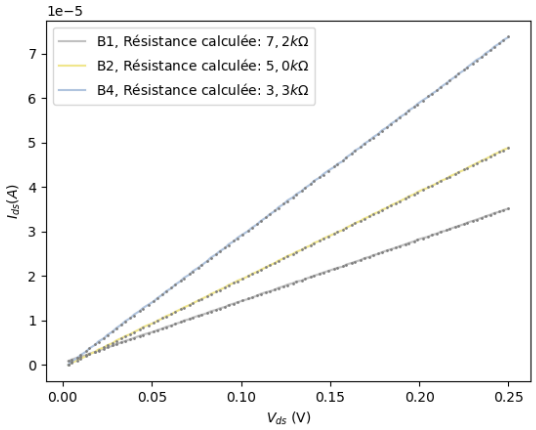

Figure 3.10 – Courbes de sortie des dispositifs B1, B2 et B4 prises sur la puce AB02 avec V_{ds} de 0 à 0,25 V par incréments de 0,003 V. Les ajustements de courbe et la pente extraite (équivalente à la résistance de contact) sont également données dans la légende.

La Figure 3.11a montre une courbe de transfert acquise par le système. On note tout d'abord la propreté du signal, ce qui indique une bonne optimisation des circuits. On peut aussi souligner la forte intensité du signal atteignant l'ordre de 10^{-5} A, une valeur dans le haut de la gamme habituelle pour ce type de dispositif. Lors d'une mesure de courbe de transfert, le voltage est d'abord balayé de manière croissante, puis décroissante. Ceci explique la présence de deux courbes. Un avantage notable de la parallélisation des mesures électriques est la possibilité de produire des études statistique pour une métrique choisie afin d'avoir un portrait global de notre production. À la Figure 3.11b et c, nous pouvons observer l'évolution du voltage au point de neutralité de charge des parties croissantes (balayage croissant) et décroissantes (balayage décroissant) de trois courbes de transfert prises à cinq minutes d'intervalle pour 64 dispositifs répartis sur neuf puces. Le voltage au PNC est une métrique informative car il mesure l'état de dopage du graphène. Le voltage est extrait à l'aide d'un ajustement de courbe polynomial dans une région autour du minimum des courbes de transfert. Nous pouvons tirer plusieurs conclusions informatives de ces graphiques. Tout d'abord, toutes les courbes sont dopées positivement, un comportement commun pour les TECG qu'on attribue à l'oxygène dans l'air et à une distribution inhomogène des charges entre le graphène et le substrat [230]. Dans la gamme de voltages positifs, la répartition est elle-même plutôt uniforme. Il ne semble donc pas avoir de biais particulier induit par le système de mesure ou la fabrication. Nous pouvons également évaluer l'hystérèse et la stabilité temporelle des courbes.

L'hystérèse est la différence de forme des courbes croissantes et décroissantes et peut être évaluée par la différence de leur voltage au PNC. On attribue l'hystérèse à des mécanismes de capture de charges à la surface du graphène [231, 232] dont l'impact peut être réduit à travers différentes stratégies de fabrication comme des recuits [233] ou de la passivation [231]. Bien qu'elle n'affecte pas la performance de détection des capteurs, la magnitude de l'hystérèse est intéressante à quantifier car elle témoigne de la qualité de la fabrication des TECG, notamment l'homogénéité

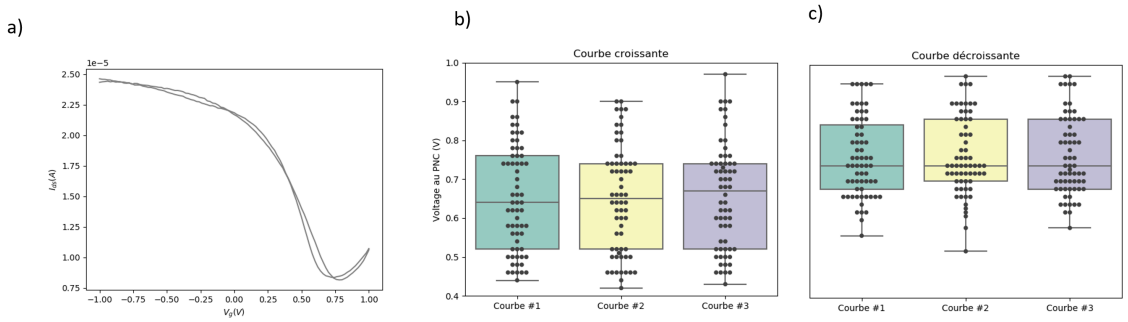

Figure 3.11 – a) Courbe de transfert du dispositif B6 de la puce *WAF_CMB2_3x3_3 Chip2*. Le voltage de grille est balayé de -1 V à 1 V, puis de 1 V à -1 V par incréments de 0,02 V avec $V_{ds} = 0{,}05$ V et un délai de source de 0,1 s. b) Boîtes à moustaches des valeurs du voltage au point de neutralité de charge des courbes croissantes de 64 dispositifs répartis sur neuf puces pour trois courbes de transfert prises à cinq minutes d'intervalle. c) Boîtes à moustaches des valeurs du voltage au point de neutralité de charge des courbes décroissantes de 64 dispositifs répartis sur neuf puces pour trois courbes de transfert prises à cinq minutes d'intervalle. Pour toutes les courbes, le voltage de grille est balayé de -1 V à 1 V, puis de 1 V à -1 V par incréments de 0,02 V avec $V_{ds} = 0{,}05$ V et un délai de source de 0,1 s.

de la répartition de la charge entre le graphène et le susbtrat. Pour ce faire, nous comparons la moyenne des distributions croissantes (0,65 V) et décroissantes (0,76 V). L'échantillonnage de plus de 40 dispositifs (qu'on approxime indépendants), nous permet de faire un test T à deux échantillons. Nous obtenons $p << 0{,}01$, ce qui suggère que la variation entre ces deux moyennes n'est pas due à des fluctuations statistiques. L'hystérèse moyenne de nos dispositifs est donc d'environ 0,11 V entre les courbes croissantes et décroissantes. Cette valeur pourrait être diminuée par les stratégies de fabrication précédemment mentionnées. Pour les travaux décrits dans ce mémoire, nous nous satisferons de cette hystérèse. Lors de détections, on contournera ce problème en ne comparant que les courbes croissantes, ou que les courbes décroissantes.

Contrairement à l'hystérèse, l'instabilité temporelle entre des courbes de transfert ne peut pas être contournée lors des expériences et il est important de la caractériser, particulièrement lorsque le dopage est la métrique de détection. Des courbes stables dans le temps sont bien sûr favorables et sont parfois considérées comme une métrique de qualité des transistors [233]. L'instabilité temporelle peut également être due à une propriété intrinsèque du système de mesure. En effet, un comportement anecdotique de la station de mesures sous pointes utilisée dans le passé est le changement de dopage marqué entre une première courbe et les courbes subséquentes. Afin d'établir la variabilité temporelle, on compare les moyennes entre les courbes 1, 2 et 3 des panneaux b et c de la figure 3.11, qui varient très peu dans les deux cas. La variance observée pour les courbes croissantes est de $2{,}89 \times 10^{-6}$ V et de $9{,}35 \times 10^{-5}$ V pour les courbes décroissantes. En moyenne, le voltage au PNC varie de 0,002 V entre la première et la deuxième courbe et de 0,001 V entre la deuxième et la troisième. Nous concluons donc que les courbes croissantes et

décroissantes sont très stables dans le temps, ce qui atteste de la qualité de nos transistors et de notre système de mesure.

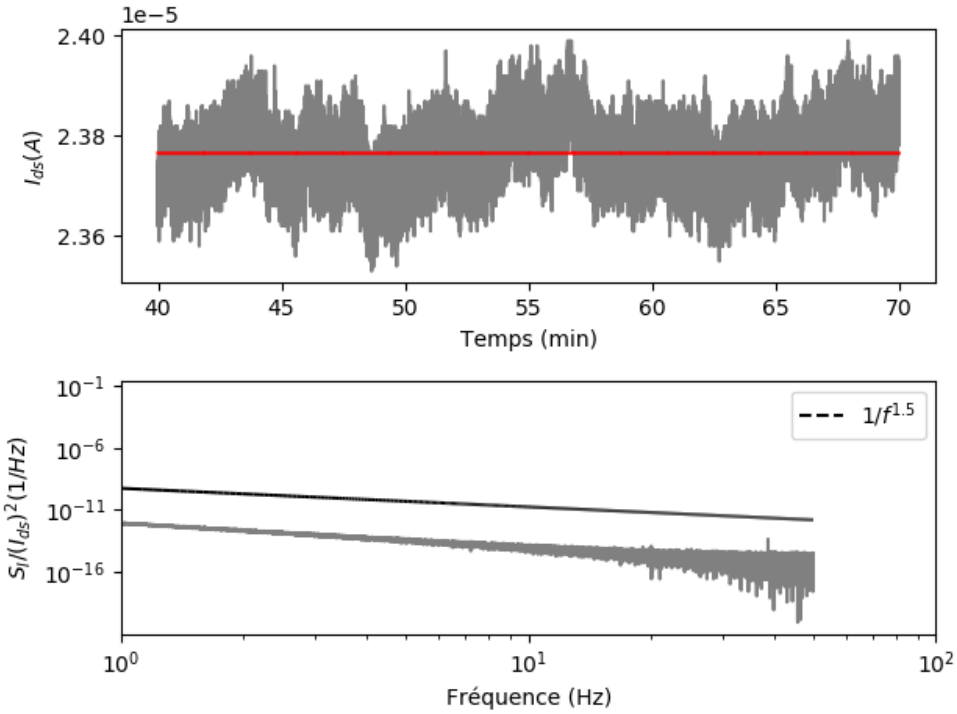

Figure 3.12 – Panneau supérieur : série temporelle de la puce *WAF_CMB2_3x3_3 Chip9* dispositif B5 avec $V_g = 0{,}9$ V, $V_{ds} = 0{,}05$ V, une vitesse d'échantillonnage de 100 échantillons/s, un tampon de 100 échantillons par chaine et un délai de source de 0,1 s. Cette série est la portion stable à voltage de grille fixe suivant les 40 premières minutes d'une plus longue série temporelle. La ligne rouge présente le courant moyen de cette série. Panneau inférieur : profil spectral de puissance du bruit associé à la série temporelle, extrait avec la méthode du périodogramme moyen de Welch. La ligne pointillée sert de guide pour l'oeil.

Un important critère de performance de notre appareillage est la qualité de ses séries temporelles. Ces dernières doivent pouvoir permettre à la fois une longue période d'acquisition et une grande vitesse d'échantillonage, en plus d'avoir un signal propre et stable. Le *PXI* n'ayant pas de mémoire interne, les données sont enregistrées directement dans l'ordinateur branché sur un nuage de mémoire virtuellement illimitée. La qualité et la longueur des séries temporelles ne sont donc jamais compromises. La vitesse d'échantillonnage maximale théorique du module d'acquisition de données est de $1{,}25 \times 10^6$ échantillons par seconde, ce qui n permet de détecter un signal d'une fréquence maximale de 625000 Hz (pour éviter le repliement de spectre), équivalent à une résolution temporelle de l'ordre de 1×10^{-6} s. Ceci correspond aux vitesses d'intérêt pour des événements biologiques comme le repliement de protéines [234, 235]. Une analyse de bruit sommaire est illustrée à la figure 3.12. Le panneau supérieur présente une section de 30 minutes d'une série temporelle prise à un voltage $V = 0{,}9$ V, à une vitesse d'échantillonage de 100 échantillons par seconde. La

ligne rouge correspond à la valeur moyenne du courant mesuré pour cette section. Un graphique de la densité spectrale de puissance de bruit, calculée avec la méthode du périodogramme moyen de Welch, est présenté dans le panneau du bas. Pour les TECG, la densité de puissance spectrale du bruit est donnée par

$$S_I = \frac{AI_D^2}{f^\gamma} \tag{3.2}$$

où S_I est la densité spectrale de puissance, A est l'amplitude du bruit, I_D est le courant moyen, f est la fréquence et γ est un paramètre expérimental [236]. Typiquement, $\gamma \approx 1 - 1{,}1$ [237]. Le bruit associé au graphène (appelé parfois bruit de scintillement) a un profil spectral en $1/f$. Une courbe d'ajustement montre dans notre cas que $\gamma \approx 1{,}5$, ce qui suggère que le système est dominé par le bruit de scintillement, mais pourrait contenir d'autres contributions comme la résistance de contact [237] ou le bruit systématique provenant des amplificateurs [238]. Afin d'évaluer l'importance du bruit, on regarde son amplitude à $f = 1$ Hz qui est de 10^{-12}/Hz. On peut comparer cette amplitude à celle d'autres articles, typiquement entre 10^{-8}/Hz et 10^{-9}/Hz [236, 237, 239]. Le bruit de notre système est donc très bas, mais nous nous devons de nuancer en mentionnant la vitesse d'échantillonnage supérieure dans les articles, pouvant permettre une représentation potentiellement plus fidèle du signal, notamment à cause d'effets de repliements de signal [240]. Cette analyse sommaire du bruit sera suffisante dans le cadre de ce mémoire, où des comportement généraux s'étendant sur plusieurs minutes et ordres de magnitude seront évalués dans le chapitre 4, ne nécessitant pas une grande précision. Toutefois, une analyse plus systématique en fonction du voltage de grille, de la vitesse d'échantillonnage ainsi que des calculs du ratio de signal sur bruit devra être menée avant des expériences s'intéressant à des événements à l'échelle de la microseconde.

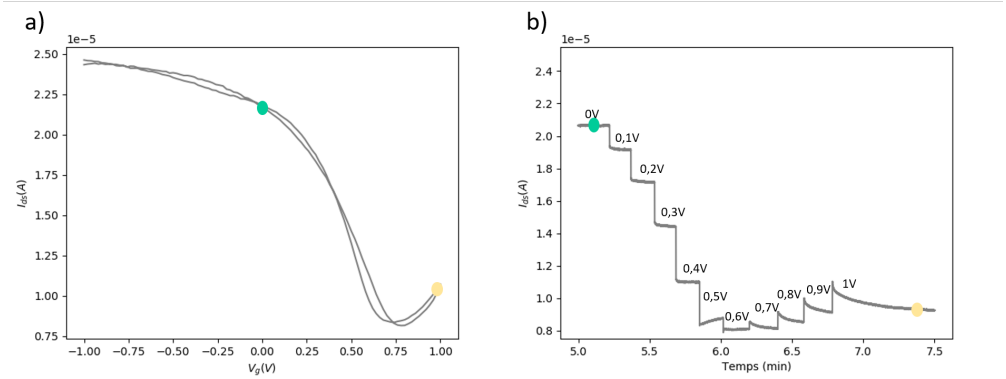

Figure 3.13 – a) Courbe de transfert du dispositif B6 de la puce *WAF_CMB2_3x3_3 Chip2*. Le voltage de grille est balayé de -1 V à 1 V, puis de 1 V à -1 V par incréments de 0,02 V avec $V_{ds} = 0{,}05$ V et un délai de source de 0,1 s. b) Série temporelle du même dispositif à $V_{ds} = 0{,}05$ V avec une vitesse d'échantillonnage de 100 échantillons/s, un tampon à 100 échantillons par chaine et un délai de source de 0,1 s. Le voltage de grille est balayé de 0 V à 1V par incréments de 0,1 V à intervalles de 5 secondes. Les points verts indiquent le courant à 0 V dans chacune des courbes et les points jaunes le courant à 1 V.

Le dernier critère évalué porte sur la synchronisation et le couplage entre la grille et les dispositifs pour les deux types de mesures principales (courbes de transfert et séries temporelles). Un montage et un code convenablement conçus devraient permettre de mesurer la même valeur de courant à un voltage donné indépendamment du type de mesure. La figure 3.13a montre une courbe de transfert acquise automatiquement par le système, alors que le panneau b montre une courbe de transfert prise manuellement, en changeant les voltages de 0 V à 1 V par incréments de 0,1 V à des intervalles de cinq secondes lors d'une série temporelle. En suivant les points jaunes et verts, nous notons une bonne correspondance entre les valeurs de courant aux mêmes voltages. Le point vert se situe entre 2×10^{-5} A et $2{,}25 \times 10^{-5}$ A dans les deux courbes, alors que le point jaune se trouve aux environs de 1×10^{-5} A. Cette correspondance démontre un couplage entre la grille et les dispositifs efficace et cohérent pour les deux types de mesures. Nous pouvons aussi voir au panneau b que le changement de voltage semble se traduire par un changement de courant immédiat, en observant la droiture du courant entre les différents voltages. Concrètement, la synchronisation entre le voltage et le courant a été mesurée par des minuteurs internes au codes, qui démontrent une précision au dix-millième de seconde près.

3.3. Conclusion

Bien que nous étions déjà en mesure de fabriquer et mesurer nos capteurs, la rédaction de la revue de littérature critique du chapitre 2 nous a mené à reconsidérer la qualité et la pertinence de nos pratiques, ainsi que nos exigences scientifiques. Dans cette optique, la première étape fut d'optimiser la fabrication des transistors, notre matière première. Des modifications au protocole, ainsi que l'instauration d'un processus de suivi a permis d'en améliorer et d'en monitorer la qualité. Plus de 250 capteurs furent générés suivant cette méthodologie. Nous avons également développé une nouvelle instrumentation répondant à nos besoins :

- **Capacité de prendre des courbes de sortie, des courbes de transfert et des séries temporelles de qualité** : nous avons démontré que le système produit des signaux stables dans les trois cas. Nous avons des faibles résistances de contact, des courbes de transfert stables dans le temps et des séries temporelles peu bruitées.
- **Mesures de tous les dispositifs d'une puce en parallèle** : le mécanisme interne des DAQ ouvre toutes les chaines d'acquisition parfaitement simultanément, ce qui permet de les mesurer au même moment.
- **Contrôle sur la mesure des dispositifs** : grâce à l'architecture des circuits imprimés, nous pouvons connecter à la masse ou faire flotter chaque dispositif. De plus, les codes permettent de choisir quels dispositifs sont mesurés et quelles données enregistrées.
- **Résolution et longueur des séries temporelles** : la mémoire disponible virtuellement infinie et la haute vitesse d'acquisition permettent des mesures précises sur de longues durées.

- **Synchronisation de la prise de donnée et de l'application des voltages** : le fonctionnement interne du *PXI*, où les modules sont connectés à un châssis permet une synchronisation de très haute précision.
- **Flexibilité du montage** : implémenté pour lire une puce, le montage peut facilement être modifié pour en lire jusqu'à quatre simultanément. De plus, puisqu'il est directement posé sur un banc de laboratoire, l'ajout d'autres instruments est facile. Par exemple, un système de pompes à seringues a déjà été ajouté pour contrôler le flux de solution (voir l'annexe B où ceci est illustré).

Finalement, en concevant et construisant ce système de mesures électriques en parallèle à haute précision adapté à nos besoins, nous avons créé un contexte idéal pour investiguer un élément clé de la performance de biodétection qui sera détaillé dans le prochain chapitre : la fonctionnalisation de la surface du graphène.

Chapitre 4

Fonctionnalisation covalente par électrogreffage sur transistors de graphène

L'analyse présentée dans le premier chapitre suggère que la conception de la surface de biodétection est un élément déterminant de la performance d'un capteur biologique. La fonctionnalisation du graphène est à la base du développement de l'interface de détection, puisque la stabilité et la densité surfacique des molécules de fonctionnalisation dicte celle des sondes biologiques, et éventuellement celle du complexe sonde-cible. La fonctionnalisation covalente aux sels de diazonium présente plusieurs avantages comme la stabilité et la versatilité de ses adduits, mais modifie la structure électronique du graphène, pouvant rendre les dispositifs inutilisables si elle n'est pas contrôlée. Ce chapitre propose une solution permise par l'optimisation de la fabrication et de l'opération des capteurs présentée au dernier chapitre.

Contributions d'Anouk Béraud (auteure principale à égale contribution avec C.M. Bazán) : conception de l'approche, développement d'instrumentation, fabrication des capteurs, expériences de fonctionnalisation et contrôles sur le nouvel appareil et leur analyse, l'analyse des données de Minh Nguyen, rédaction des sections de résumé, introduction, expériences de surface, expériences sur la cinétique et production des figures. Contributions de Claudia M. Bazán : expériences préliminaires pour la preuve de concept, expériences de fonctionnalisation spontanée et leur analyse, fabrication de la version finale des circuits électriques, mesures RIMA et analyse des spectres, expériences de fonctionnalisation et expériences contrôles sur le nouvel appareil et leur analyse, rédaction des sections sur la fonctionnalisation spontanée et le contrôle de la réaction par la grille (avec Anouk Béraud) et production des figures. Contributions des co-auteurs : Minh Nguyen a fait les expériences sur l'effet du substrat sur la fonctionnalisation et Amira Bencherif la fabrication des dispositifs pour les expériences préliminaires. Richard Martel a assuré la supervision de Minh Nguyen. Delphine Bouilly a assuré la supervision globale des expériences et du contenu de l'article. Elle a effectué la relecture, ainsi que la réécriture finale de toutes les sections.

Note : Les informations supplémentaires de cet article (*Supporting Information*) sont présentées à l'Annexe B.

Dynamic Gate Control of Aryldiazonium Chemistry on Graphene Field-Effect Transistors

Claudia M. Bazán[†1], Anouk Béraud[†1,2], Minh Nguyen[3], Amira Bencherif[1,4], Richard Martel[3] et Delphine Bouilly[1,2]

1- Institut de recherche en immunologie et cancérologie, Université de Montréal, Montréal, Canada.
2- Département de Physique, Faculté des arts et des sciences, Université de Montréal, Montréal, Canada.
3- Département de chimie, Faculté des arts et des sciences, Université de Montréal, Montréal, Canada.
4- Institut d'ingénierie biomédicale, Faculté de médecine, Université de Montréal, Montréal, Canada.
† Ces deux auteures ont contribué également.

RÉSUMÉ. Alors que l'utilisation de transistors à effet de champ à base de graphène (TECG) comme capteurs est en plein essor, l'efficacité et le contrôle de la fonctionnalisation de leur surface devient un paramètre critique. Ici, nous introduisons une méthode innovatrice utilisant l'électrode de grille pour moduler avec haute précision la fonctionnalisation aux sels d'aryldiazonium directement sur des dispositifs de graphène. Bien que cette chimie covalente soit connue, nous montrons que la forme spontanée de sa réaction sur TECG est hautement hétérogène et produit un rendement global faible. En ajustant dymaniquement le voltage de grille en présence du réactif, nous pouvons rapidement favoriser ou supprimer la réaction, résultant en un important degré d'homogénéité entre les dispositifs. Nous sommes également capables de suivre et de contrôler la cinétique de réaction en temps-réel. Le mécanisme de notre approche est basé sur la disponibilité du transfert d'électrons, de manière analogue au dopage chimique, de substrat, ou électrochimique, mais a l'avantage pratique distinct d'être complètement implémentable sur des dispositifs, ou des puces. Ce travail illustre la puissance des plateformes de TEC pour étudier les réactions à la surface de nanomatériaux en temps-réel.
Mots-clés : Détection, graphène, transistors à effet de champs, fonctionnalisation, électrogreffage, diazonium

ABSTRACT. As graphene field-effect transistors (GFETs) are increasingly valued for sensor applications, efficiency and control of their surface functionalization become critical. Here, we introduce an innovative method using the gate electrode to precisely modulate aryldiazonium functionalization directly on graphene devices. Although this covalent chemistry is well-known, we show that its spontaneous reaction on GFETs is highly heterogeneous with a low overall yield. By dynamically tuning the gate voltage in presence of the reactant, we can quickly enable or suppress the reaction, resulting in a high degree of homogeneity between devices. We are also able to monitor and control functionalization kinetics in real-time. The mechanism for our approach is based on electron transfer availability, analogous to chemical, substrate-based, or electrochemical doping, but has the practical advantage of being fully implementable on devices or chips. This work illustrates how powerful the FET platforms are to study surface reactions on nanomaterials in real-time.

Keywords : Sensing, graphene, field-effect transistors, fonctionnalization, gate-controlled functionalization, diazonium

Cet article a été accepté pour publication à Nanoletters, American Chemical Society.

4.1. Introduction

Amongst the many functionalization strategies available for nanocarbon materials [31, 241, 242], aryldiazonium chemistry has sparked a lot of interest due to its ease of preparation, rapid reaction time, various choice of functional groups, compatibility with a wide range of materials, and its strong aryl-surface covalent bonding [33]. First popularized for carbon nanotubes in 2001 [243], this chemistry was eventually adopted for the functionalization of graphene surfaces [244-246]. In graphene, the spontaneous reduction of aryldiazonium salts leading to the covalent modification of the surface material has been widely investigated by optical and scanning probe methods such as Raman spectroscopy [247-250], scanning tunneling microscopy (STM) [251, 252], angle-resolved ultraviolet photoelectron spectroscopy (ARPES) [253], or atomic force microscopy (AFM) [252, 254]. Improvements have been made over the years, either to increase the grafting density by electrochemically or chemically driving the reaction [249, 252, 255-258] or to control the position of adducts using local probes or surface patterning [254, 259, 260].

Spontaneous diazonium functionalization has also been conducted on graphene field-effect transistors (GFETs) and studied electrically [28, 77, 217, 248, 261-266]. Surface functionalization of GFETs is particularly essential for applications requiring to either enhance or passivate the interactions of graphene with the surrounding environment, such as in chemical or biological sensing [33, 34, 257, 267]. It is interesting to note that experiments using aryldiazonium salts with GFETs have led to variable results in the literature with respect to electrical metrics : some studies have reported a lateral shift in the transfer curve without much change in conductance amplitude [262, 266], which is more consistent with doping than covalent binding [34], while others have reported the opposite behaviour [264]. The variability of response between initially similar individual graphene devices has been highlighted by Pembroke *et al.* [217], who underline the need for statistical analyses over an ensemble of devices.

In addition, the electrical curves of field-effect transistors provide specific metrics that are informative about surface reactions and interactions [34]. This has already proved to be of great interest to study the aryldiazonium chemistry in carbon nanotubes : as examples, the study of transfer curves and their temperature dependence has revealed evidence of mid-gap electronic states localized around aryl adducts [268], and real-time series have recorded the formation and stability of individual sp^3 defects from this grafting reaction [269]. Precise control of the aryldiazonium chemistry on carbon nanotube devices, using either nanolithography or potential control, has been pushed to the limit of single-point functionalization and applied for single-molecule sensing [270-272]. In graphene, aryldiazonium chemistry has been little investigated in real-time, most studies rather compare microscopy, optical spectra, or electrical curves before and after a finite reaction

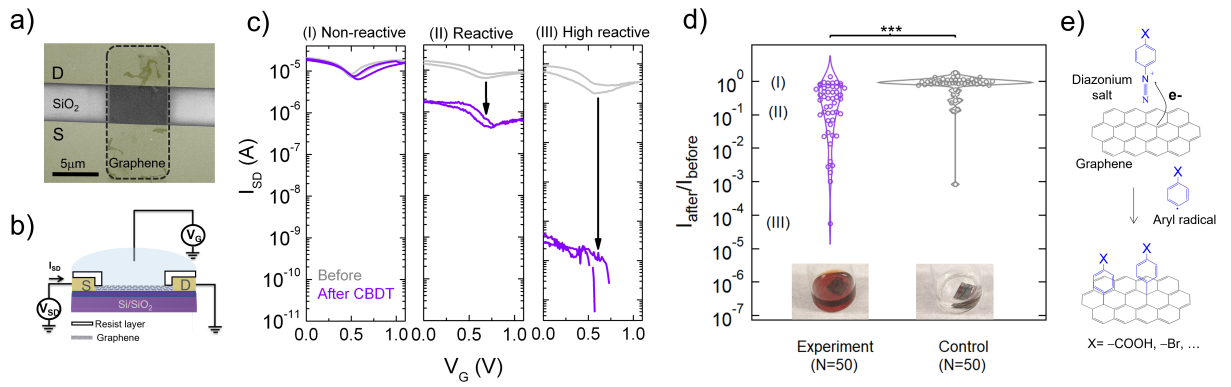

Figure 4.1 – Spontaneous aryldiazonium reaction on GFETs. (a) Colored scanning electron microscope (SEM) image of a typical GFET showing a graphene ribbon on SiO_2 connected by source (S) and drain (D) electrodes. The channel area between electrodes is 4 μm x 6 μm. (b) Schematics of a GFET device with passivated S/D electrodes, operated in buffer solution with an immersed gate electrode (G). (c) Transfer curves for three initially similar GFETs showing different degrees of conductance drop after spontaneous reaction with aryldiazonium salts (24h incubation with CBDT). (d) Violin plots of the change in conductance across multiple GFET devices (N=50), for the spontaneous functionalization experiment (in CBDT reagent) and the control (in buffer only). Labels (I), (II) and (III) represent the change associated to GFET devices shown in (c). (e) Schematic illustration of the grafting of aryl groups to graphene via the reduction of a generic aryldiazonium salt.

time. More generally, the interesting features available in devices (e.g. electrical fields, multiplexing, real-time) have not yet been fully exploited to understand or control the surface reaction in GFETs. And to this day, there is little control available on the degree of covalent functionalization on GFETs, which is critical for many applications of these devices, such as chemical or biological sensors.

Here, we present a powerful method taking advantage of the field-effect transistor configuration to achieve highly controlled functionalization of GFETs with aryl adducts. Specifically, we use the gate voltage to modulate *in situ* the functionalization rate and to trigger or stop the reaction at will, thus controlling the functionalization yield with high precision and uniformity across multiple devices and chips. Our on-chip method also allows for the multiplexed monitoring and control of many GFET devices simultaneously. We start by a systematic and statistical study of the spontaneous functionalization approach over multiple GFET devices, demonstrating that it is unreliable and most of the time inefficient. We describe our state-of-the-art setup for gate-controlled functionalization (see Fig. B.1), then we present evidence for unprecedented control on the functionalization metrics (rate, start/stop, yield) while being able to monitor and adjust reaction kinetics in real-time.

4.2. Results and Discussion

The most common approach to performing aryldiazonium functionalization on GFETs is simply to immerse the devices in a solution of the reactant [248, 261, 264]. We first demonstrate the

limitations of this method, especially its low efficacy and reproducibility, by performing a robust statistical analysis on a large number of GFETs (N=50), assessing for each their electrical properties before and after passive immersion in solution with aryldiazonium salts.

Our GFET devices were fabricated from graphene grown by chemical vapor deposition (CVD), transferred and patterned onto Si^{++}/SiO_2 chips previously evaporated with an array of metallic electrodes (see more details on Materials, methods, and instrumentation in the Supporting information, Annexe B). Figure 4.1a shows a colored scanning electron microscope (SEM) image of a typical GFET, with a graphene ribbon (grey) connecting source (S) and drain (D) electrodes (gold). A protective layer of photoresist was added over the whole chip except the graphene ribbon area, to avoid unwanted reactions of electrodes in solution. A total of 50 GFET devices were tested, distributed over 9 different chips. Backgated transfer curves were first taken in air, but showed significant p-doping of the graphene, as common in ambient conditions on SiO_2 [217, 273, 274]. To be able to resolve the charge neutrality point (CNP) and thus monitor for any doping effects during the chemical reaction, we turned to transfer curves collected in saline buffer (phosphate buffer (PB) 100mM, pH = 8.0) using a pseudo reference gate electrode immersed in a top-open PDMS cell (Fig. 4.1b). Typical transfer curves with backgate and immersed gate are shown in Fig. B.2. All devices were found to exhibit comparable initial electrical metrics, *i.e.* voltage and current at the charge neutrality point (V_{CNP}, I_{CNP}, see Fig. B.3), as shown by their compact distributions in Fig. B.4.

We investigated changes in the electrical transfer curves of the devices after immersion 24h in buffer only (control), then 24h with 10mM 4-carboxybenzenediazonium tetrafluoroborate (CBDT) (experiment). Figure 4.1c shows examples of transfer curves for three individual graphene devices (I-II-III) before and after incubation in the CBDT solution. We see that the response varies largely between different devices : many show barely any change after exposure to the reactant (as in I), but others show a drop in conductance, with a magnitude going from moderate (II) to very large (III). It should be noted that all devices, including I to III, started with similar initial electrical characteristics (Fig. B.4), and were not significantly affected by the control incubation in buffer only (Fig. B.5). The change in transfer curves seen in devices II-III is really a drop, and not a shift : only a small p-doping was observed on average after functionalization (Fig. B.6), which cannot explain a change of such magnitude in the conductance [34]. We compiled the conductance drop across all devices (N=50) : Figure 4.1d shows the ratio of the current of each individual GFET after/before 24h incubation in buffer (control) or CBDT solution (experiment), at fixed immersed gate voltage (V_G=0), with the intensity profile of the distribution captured using violin plots. After the control incubation in buffer, the distribution is tightly centered around 1, as expected when no reaction is occurring, with all devices but one outlier remaining within one order of magnitude of their initial conductance value (see statistical analysis in Fig. B.7). After incubation in CBDT, the distribution shows a much wider variance, with 28% of the devices dropping by more than one order of magnitude (Fig. B.7). The two distributions (chemistry *vs.* control) are statistically different (p-value $<$ 1e-5 for a two-tailed two-sample Student's t-test assuming non-equal variances) indicating that there is a net effect from the chemistry, but the magnitude of this effect is small for most devices and significantly heterogeneous across the population of devices.

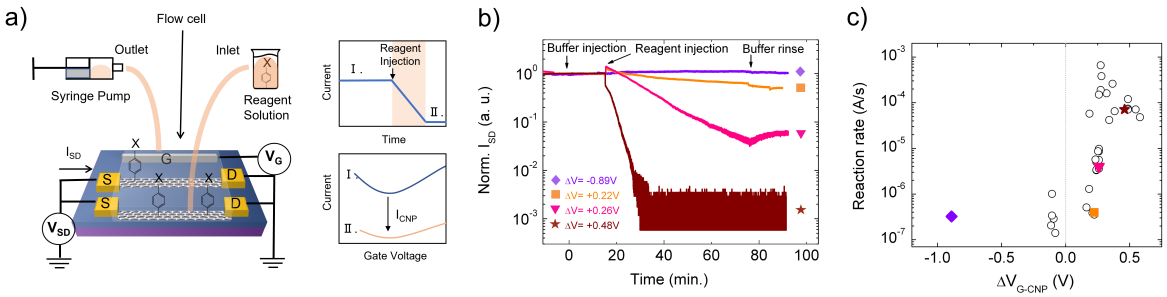

Figure 4.2 – Real-time monitoring and control of the aryldiazonium reaction rates on GFETs. (a) Illustration of the experimental system using an on-chip gate electrode to modulate the doping state of multiple GFETs *in situ* while immersed in a syringe-operated flow cell. Time series of the current are recorded during incubation ; transfer curves are also recorded before and after the reaction. (b) Typical time series of the aryldiazonium reaction on GFETs under different applied gate voltages, showing the effect of buffer injection (control), then reagent injection (experiment) and subsequent washing. (c) Reaction rates obtained from an exponential fit of multiple time series (N=33) as a function of the applied gate voltage relative to the charge neutrality point of the device ($\Delta V_{G-CNP} = V_G - V_{CNP}$). Each marker corresponds to the functionalization rate of an individual device following the same protocol at different gate voltages ; colored markers specifically refer to time series shown in (b).

The loss of electrical conductance following covalent functionalization is due to the sp^2-to-sp^3 change in the hybridization of host carbon atoms and the resulting conversion of delocalized electrons into covalent bonds between the aryl groups and the graphene surface (Fig. 4.1e) [246, 275, 276]. The limiting step of the reaction is considered to be the reduction of the diazonium group of the reagent, which requires an electron transfer from the carbon material [277]. In the case of devices on Si/SiO_2, the graphene is typically p-doped (Fig. B.4) [230, 278], hence in an electron-deprived state, which explains why the majority of devices reported a low response to the functionalization chemistry. Still, a certain fraction of functionalized devices (28%) did exhibit a significant reactivity. This heterogeneity was verified to be unrelated to the initial electrical characteristics of the devices (Fig. B.8). We expect it could be due to inhomogeneous charge puddles caused by impurities on the graphene surface or in the SiO_2 layer [279, 280]. The variability in the response of similar devices and its unpredictability from initial device metrics constitute a critical issue for most applications relying on surface functionalization, such as sensors, and raises the need for a more controlled approach.

In response to this challenge, we propose to take advantage of the constitutive configuration of electrodes in the GFET architecture to control the aryldiazonium reaction on the surface of graphene devices. Specifically, our approach exploits the modulation of the Fermi level of graphene by the potential applied to the gate electrode, as recently used with carbon nanotubes [272] or on graphene with another chemistry [281]. The underlying mechanism is analogous to that of electrochemical doping [256], but this implementation offers more powerful possibilities than standard

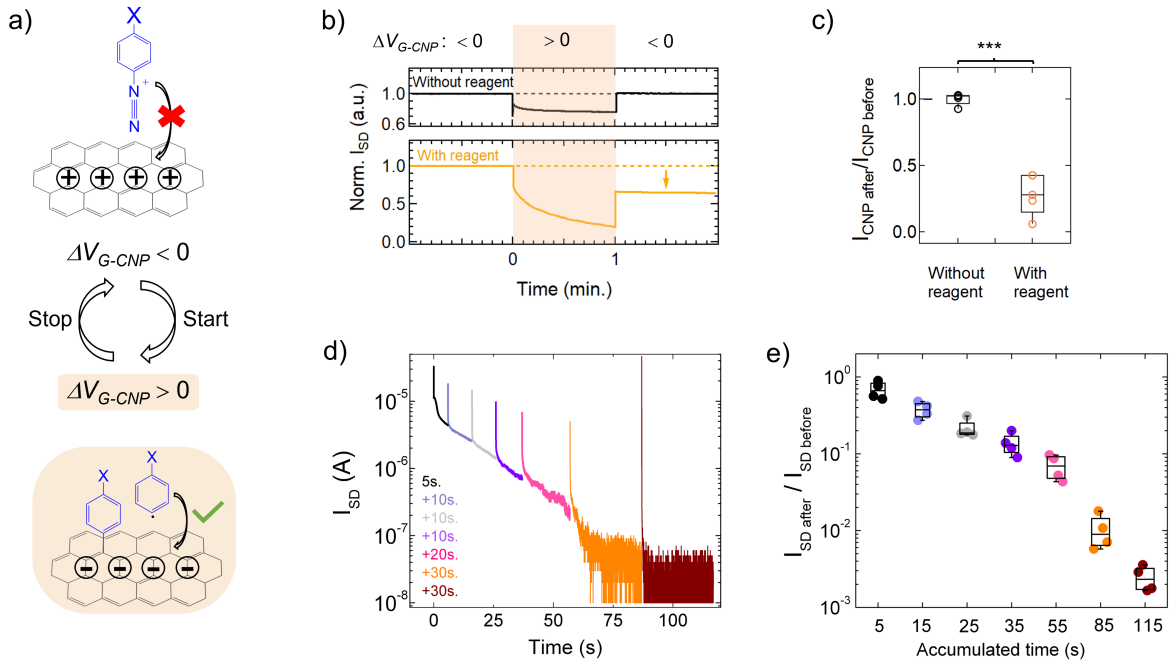

Figure 4.3 – Dynamic control of the aryldiazonium reaction on GFETs. (a) Conceptual illustration of the gate-mediated start/stop triggering of the functionalization reaction in presence of the aryldiazonium reagent. (b) Time series showing gate-mediated 1 min activation and subsequent quenching of the reaction in presence of the aryldiazonium reagent (orange) and a control in buffer only (black). (c) Distribution of the change in conductance for multiple devices after 1-min gate-activated functionalization (orange) vs control (black). (d) Time series showing incremental reaction on the same GFET, using short successive gate-switched activation times. (e) Distribution of the change in conductance versus accumulated grafting time for multiple devices (N=4). Colors correspond to the gate-activated reactions periods shown in (d).

electrochemistry in terms of real-time monitoring and control on arrays of devices. In the following, we demonstrate that we can use instrumentation already adapted for the electrical probing of GFETs to obtain precise control on the rate, duration and yield of the aryldiazonium reaction while recording its progress in real-time. Given the established need for robust statistical analysis [217], we specifically used a custom multiplexed chip probing system to parallelize gate-controlled aryldiazonium reaction on arrays of multiple devices. Figure 4.2a presents a schematic of the system ; more details on its components are provided in the Materials, methods and instrumentation section of the Supporting Information (including Fig. B.1). Gate and source-drain voltages were simultaneously applied to all devices, while source-drain currents were measured in parallel. The GFET chip was also mounted with a flow cell linked to a programmable syringe pump to deliver the functionalization reagents.

A major advantage of studying functionalization on GFETs is to be able to directly monitor the evolution of the reaction in real-time, and therefore to extract kinetic information. Time series of the drain-source current were first collected in parallel at fixed gate voltage, during which the

aryldiazonium salt solution was injected for a given period and then washed away using the syringe pump. Transfer curves were also taken before and after the time series. This experimental protocol is schematized in Fig. 4.2a, and further detailed in Fig. B.9. Figure 4.2b presents four time series of GFET source-drain current recorded during subsequent injections of buffer (control) and reagent (experiment), under different gate potentials. For all devices, the control injection of buffer only had no noticeable effect on the conductance. During injection of the reagent, the curve collected in the p-doped regime (violet) also remains flat, consistent with an absence of covalent functionalization on the graphene surface. In electron-doped devices (orange, pink, brown), however, the conductance clearly drops with time, following an exponential decrease from the moment of injection with a reaction rate increasing with the applied gate voltage. In the brown curve, the conductance actually completely drops to zero within a few minutes.

The reaction rate was systematically extracted for multiple GFETs (empty and colored markers) as the slope of the linear regime in semilog plots (see Figs. B.10 and B.11), and its resulting relationship with the doping voltage ($\Delta V_{G-CNP} = V_G - V_{CNP}$), i.e. the applied gate voltage relative to the charge neutrality point of the graphene device, is compiled in Fig. 4.2c. In electron-deprived regime ($\Delta V_{G-CNP} < 0$), extracted reaction rates are extremely small and oscillate around zero (Fig. B.12), which is consistent with flat times series such as the violet curve in Fig. 4.2b. An inflexion point occurs at the charge neutrality point ($\Delta V_{G-CNP} = 0$ V), after which starts a strong increase of the reaction rate with gate voltage. To get a more intuitive metric on the speed of the reaction, we also extracted the time required for the conductance to drop by 10% of its initial value ($t_{10\%}$, see Figs. B.13 and B.14). This time follows a generally decreasing trend with ΔV_{G-CNP} that spans over orders of magnitude, for instance going from ∼30 min (orange curve), to ∼10 min (pink curve), down to ∼1 s (brown curve). Kinetic metrics show that the rate of creation of adducts is negligible for negative ΔV_{G-CNP} and increases with positive ΔV_{G-CNP}.

This strong modulation of the reaction rate by the gate voltage is extremely promising to achieve a predetermined functionalization yield on graphene devices, by controlling both the rate and the duration of the reaction. This is critically needed for covalently functionalized GFETs and their applications, in which the density of adducts must be well-calibrated to provide optimal surface functionality while preserving enough electrical signal. Up to this point, our experiments were performed at fixed gate voltage, and the start/stop of the reaction was controlled by injecting the reagent solution or washing it away. We now propose to operate the gate voltage as a dynamic switch, to trigger the activation and quenching of the reaction while in presence of the reagent, as illustrated in Fig. 4.3a. We show that we can effectively constrain the aryldiazonium reaction during a brief time interval, resulting in a controlled and moderate change in conductance, which can then be incremented until the desired functionalization yield is obtained.

Figure 4.3b shows two subsequent time series from the same GFET : during each, the gate voltage was switched for 1 min from an electron-depriving value ($\Delta V_{G-CNP} < 0$) to an electron-doping value ($\Delta V_{G-CNP} > 0$) and then back (Fig. B.15). The first time series is a control performed in buffer only : it shows a transient shift of the current that quickly stabilizes during the 1-min window, and then reverts back to its initial value when the gate voltage is reversed. This temporary change of conductance is simply due to the altered density of charge carriers in graphene induced

by the change in gate voltage [34]. In presence of aryldiazonium salt (10 mM CBDT), the change in current during the 1-min window has a higher amplitude and keeps a sustained slope. After the gate voltage reversal, the current quickly stabilizes back in a plateau, but with a lower amplitude than its initial value. This permanent alteration of the conductance level indicates that covalent defects were created during the gate voltage switch. This experiment was repeated on multiple GFETs and the distribution of current ratios after/before gate switching are presented in Fig. 4.3c. While the conductance of devices was unaltered during the gate switch in buffer only (control), it decreased to an average of (29 ± 15)% of its initial value after 1 min activation of the reaction in presence of the reagent. This represents a moderate level of functionalization and an appreciable level of reproducibility between devices.

Such gate-switching has the advantage of decoupling the onset of the reaction from the injection of the reagent, which likely allows the aryldiazonium molecules to reach an equilibrium distribution near the graphene surface before being converted into reactive radicals. This appears to make the reaction less sensitive to injection fluctuations, as seen by the relatively homogeneous distribution of conductance change obtained even for a high reaction rate (here $\Delta V_{G-CNP} = +0.62$ V). The quick stabilization back in a plateau after the activation interval indicates that the gate voltage reversal is efficient at stopping the functionalization reaction on graphene, even if reagent molecules are still present around the surface. In comparison, we tested the effect of washing away the reagent after a similar interval of activation (Fig. B.16). The conductance of GFETs settled at (29 ± 25)% of its initial value (Fig. B.17), *i.e.* the same average value as with the gate switching but with a larger variance. The suppression of the electron reservoir with the gate voltage may thus be more efficient at quenching the reaction than physically flowing away the reagent molecules. The gate switching approach is also substantially more practical than mechanically operating syringes, which makes it easier to implement with standard GFET instrumentation.

We then show that we can dynamically increment very short gate-activated reaction times to achieve the desired change in device conductance. Successive time series were conducted, each with a short activation period ranging from 5 to 30 seconds at a very positive gate voltage. More details about the protocol are provided in Fig. B.18. Figure 4.3d shows the activated segments of each time series collated next to each other, showing a consistent continuity between reaction periods. The time series were conducted on multiple GFETs simultaneously, and the changes in conductance after each iteration for every device are compiled in Fig. 4.3e. The conductance of GFETs is found to drop regularly with accumulated reaction time, decreasing about one order of magnitude after a total of 35 seconds and reaching complete current loss after a little less than two minutes. This indicates that controlling the reaction time can be used as an effective proxy to modulate the functionalization yield. Despite the regular variance in the initial doping of the different devices, we observe a remarkable uniformity between devices from the tightly-centered boxplots in panel e, which might be explained by a saturation in reaction rates at high gate voltages. This enhances the practicality of the time-based approach to prepare arrays of GFETs with similar functionalization yields.

As the last part of this paper, we present data confirming the validity of the correlation between the loss of electrical conductance and the functionalization yield. Specifically, we compare

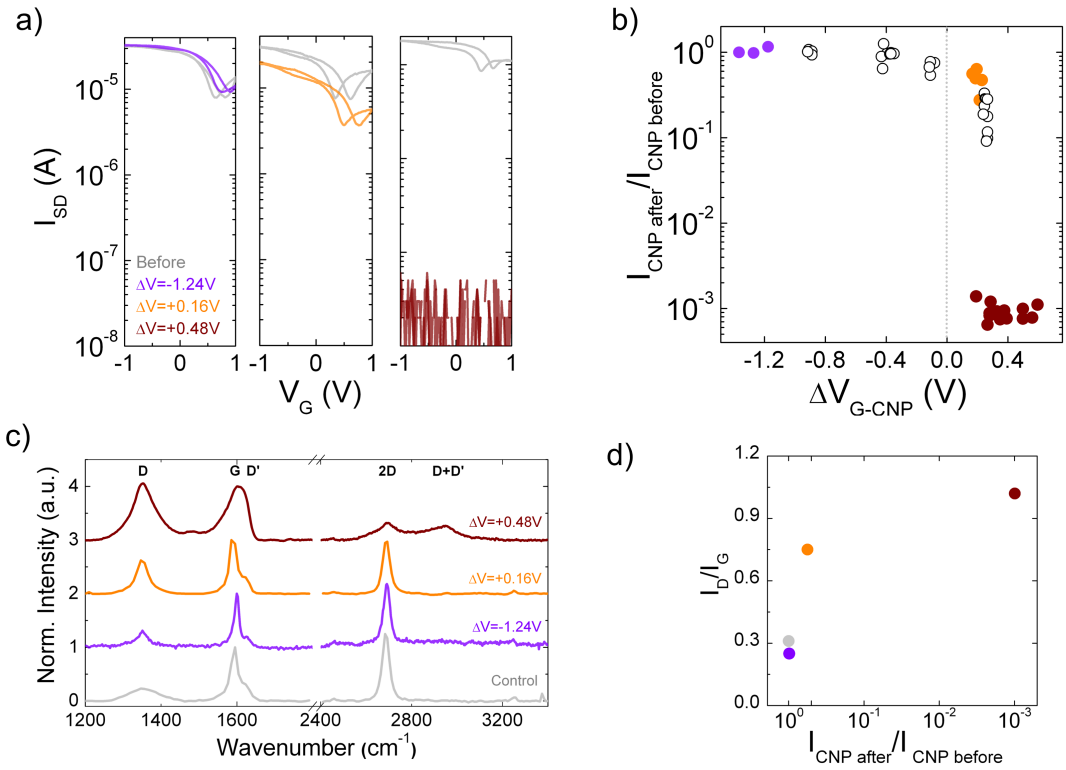

Figure 4.4 – Gate-controlled modulation of the aryldiazonium reaction yield on GFETs. (a) Typical transfer curves of GFETs before and after aryldiazonium reaction (1h incubation in CBDT), showing different degrees of change in the conductance depending on the applied gate voltage during incubation. (b) Change in conductance for multiple devices, as a function of ΔV_{G-CNP}. Each marker corresponds to the change in conductance of an individual device following the same protocol at different gate voltages ; colored markers specifically refer to the transfer curves shown in (a). (c) Raman spectra of functionalized GFET devices showing an increase in defects bands (D, D' and D+D') with increasing ΔV_{G-CNP}. (d) Integrated I_D/I_G ratios extracted from spectra in (c) as a function of the change in conductance of the devices. The control spectra is from a GFET incubated with ΔV_{G-CNP}= + 0.39 V in buffer only.

electrical metrics after functionalization with Raman spectroscopy, a widely used method to assess the amount of defects in the graphene lattice [282, 283]. Figure 4.4a first presents typical transfer curves of GFETs obtained before and after a 1h exposure to CBDT, for different values of applied gate voltage. Even when initially similar, devices undergo a loss of conductance that differs widely depending on the gate voltage applied during their exposure to the reagent : going from an absence of reaction (left) to a moderate effect (middle) until reaching a very high effect (right). Figure 4.4b compiles the loss of conductance for multiple devices (empty and colored markers) as a function of the doping voltage (ΔV_{G-CNP}). For experiments occurring in the electron-deprived state ($\Delta V_{G-CNP} < 0$), the conductance remains basically unchanged, suggesting an absence of covalent reaction with the graphene surface. On the opposite, from the CNP voltage and up ($\Delta V_{G-CNP} > 0$),

as the graphene gets increasingly electron-doped, the intensity of the conductance loss increases quickly, suggesting a corresponding increasing efficiency in the formation of aryl adducts.

Figure 4.4c presents the corresponding Raman spectra for individual devices functionalized under a gate voltage placing them in a p-doping state (violet curve), in the vicinity of the charge neutrality point (orange curve), and in an n-doping state (brown curve). The control spectrum of a device incubated in buffer only (grey) shows the typical Raman spectrum of unfunctionalized graphene on Si/SiO_2, with a G band at $\sim$1580 cm^{-1} and a 2D band at $\sim$2680 cm^{-1}, plus a small D peak at $\sim$1350 cm^{-1} occurring from measurements in solution [284]. The device exposed to CBDT in an electron-deprived state (violet) has a similar spectrum than the control, which is consistent with the functionalization process creating no additional defects in this regime. The addition of sp^3 defects typically produces additional D and D' bands at $\sim$1350 cm^{-1} and $\sim$1615 cm^{-1}, disorder-induced bands activated by a single-phonon intervalley and intravalley scattering process [285]. Indeed, in the two other spectra (orange and brown), the D and D' peaks (and their combination mode D+D' at $\sim$2965 cm^{-1}) grow with the intensity of electron doping during functionalization. To further confirm that the intensity of these peaks follows the efficiency of aryldiazonium functionalization, we tested various approaches on graphene surfaces, specifically (1) spontaneous functionalization, (2) chemical doping with hydrazine, (3) electrochemical doping using cyclic voltammetry, and (4) substrate-based doping on copper (see details in Materials, methods and instrumentation in the Supporting information). The resulting Raman spectra are presented in Fig. B.19 (spontaneous in grey, chemical doping in pink, electrochemical doping in blue, and substrate-based doping in orange). As expected, the curves show increasingly important D and D' bands with the doping strength of the method. The relative intensity of the D peak was found to depend on both incubation time and diazonium concentration during electrochemical doping (Fig. B.20), supporting the origin of disorder peaks from chemical defects. The Raman response was also similar regardless of the nature of the aryl group (Fig. B.21), also corroborating its origin in the binding chemistry. This investigation confirms that the D and D' Raman bands after functionalization are indeed due to covalent bonding of aryl adducts onto the graphene lattice as it shows increasing amounts of defects with the efficiency of the method.

In Fig. 4.4d, we confirm that the level of defects assessed by Raman is qualitatively coherent with the electrical data. To do so, we present the relative ratio of the D and G bands (I_D/I_G) of the Raman spectra from panel c. Unfunctionalized and p-doped curves (grey and violet) exhibit a similar low I_D/I_G around 0.3, whereas the orange and dark brown curves have ratios around 0.75 and 1.1. These correlate positively, although non-linearly, with the intensity of the current drop observed in panels a and b. We see a similar correlation in devices functionalized with the spontaneous approach, as shown in Fig. B.22 : device I (no loss of conductance) shows no Raman evidence of disorder, whereas device III (high loss of conductance) reports D and D' bands with high intensities. The loss of conductance and the intensity of D and D' Raman bands both appear as consistent indicators of an increase in defect density following covalent functionalization. The gate voltage, specifically its difference with the charge neutrality point, thus proves to be an effective handle to precisely modulate the density of adducts formed with the aryldiazonium reaction on devices.

4.3. Conclusion

This paper highlights the gate voltage as a practical handle to precisely control the reactivity of graphene field-effect transistors to the aryldiazonium chemistry. By adjusting the doping level of the graphene surface, it modulates the density of electrons available for the conversion of diazonium groups into reactive radical aryl species, that then bind to the graphene in the form of covalent adducts. Our work identifies the key variable to be the doping voltage (ΔV_{G-CNT}), *i.e.* the difference between the applied gate voltage and the charge neutrality voltage of the device, which was shown to regulate multiple dimensions of the chemistry : the functionalization yield, the reaction rate, as well as the triggering and the quenching (and hence the duration) of the reaction. Using FET probing equipment to apply a gate voltage *in situ* with the reactant, we demonstrated the ability to switch the functionalization reaction on and off and to monitor its progress in real-time. This approach fully exploits the architecture of GFET arrays, taking advantage of features like electric fields, multiplexing, real-time sensitivity, and on-chip integration. It is conceptually in line with other recent work using the electrostatics of the gate voltage in GFETs to influence molecular processes at the surface, for instance for controlling the orientation [286] or spatial distribution [254, 287, 288] of adsorbed molecules. The multiplexing capability of FET arrays was harnessed to obtain robust statistical analyses, proved to be essential to go beyond device-to-device variability[34, 217]. For instance, the use of ensembles of devices was decisive to demonstrate the limitations of the spontaneous reaction (low average effect, high variability) and, in contrast, the higher homogeneity obtained with a gate voltage applied.

Achieving a controlled degree of functionalization on GFET devices, especially using covalent chemistry, addresses a long-standing challenge. Indeed, the preparation of a well-defined functional surface is one of the most critical challenges faced by GFET applications such as chemical and biological sensors [34]. Covalent approaches, such as aryldiazonium chemistry, have been difficult to integrate with device-based applications because of their strong disruption of electrical conductance. Using the gate-controlled approach, our results show that it is possible to regulate and limit the formation of covalent adducts on GFETs to preserve their electrical conductance, which unlocks the preparation of functional devices with stable and strongly coupled immobilized molecules. Higher levels of functionalization densities may also be desired, for instance to form a transient seeding layer for atomic layer deposition on the channel [258]. Finally, with their real-time measurement capability allowing kinetic analyses, combined with transfer curves providing physical insight on the nature of the chemical coupling (e.g. defect *vs* doping) [34], GFETs offer a powerful platform for in-depth study of graphene functionalization [289] ; this could be further harnessed to characterize the effect of various reaction conditions (e.g. reagent concentration, flow rate, ...) and expanded to study other types of covalent and non-covalent chemistry on 2D materials.

Conclusion et perspectives

Dans ce mémoire, nous avons initié une réflexion, construit de l'instrumentation et fait des expériences dans le but d'établir les fondements nécessaires à la construction de capteurs biologiques performants. Nous synthétisons ici les résultats spécifiques reliés aux trois sous-objectifs décrits dans l'introduction et nous présentons les perspectives futures associées à ces contributions.

Disséquer les éléments clés de la conception et de l'opération des transistors comme capteurs bioanalytiques afin d'en extraire les meilleurs pratiques et d'en optimiser la performance.

Nous avons traité cet objectif de nature analytique dans le premier article de ce mémoire, une revue de littérature critique présentée au chapitre 2. Dans la première partie dédiée aux différentes stratégies de conception et de fabrication des TECG, nous avons décrit les types de graphène, les types de substrats, les possibles configurations et options de fabrication des électrodes, les médias d'analytes, les cellules de flux ainsi que les approches de fonctionnalisation et de passivation. En second lieu, nous avons expliqué les mesures électriques pertinentes à la biodétection : courbes de transfert, courbes de sortie et séries temporelles. Nous avons aussi établi les métriques associées aux mesures. Nous avons disséqué la physique de ces métriques, illustrant la relation entre les variations de signal dans les séries temporelles et les courbes de transfert. Ce faisant, nous avons souligné la complémentarité de l'information encodée dans les mesures «avant-après» et les mesures en temps-réel. Ces deux types de mesures sont nécessaires lors du développement d'un protocole expérimental complet. La dernière section traitait de l'évaluation de la performance de détection sous plusieurs formes. Nous avons établi que la métrique de performance principale est la limite de détection (LOD), soit la plus petite concentration de molécule-cible générant un signal mesurable. Dans une analyse originale, nous avons disséqué les méthodes rapportées pour la LOD et compilé 61 valeurs, triées en fonction du type de graphène, de la nature de la cible et autres paramètres pertinents. Ceci nous a permis de réfuter une croyance commune que la LOD est dépendante de la qualité du graphène. On identifie la taille de la cible comme facteur clair et on émet l'hypothèse que les autres facteurs prédominants sont la configuration de l'électrode de grille et l'assemblage de l'interface de biodétection. Plus particulièrement, nous avons noté que la chimie de surface (fonctionnalisation, densité de molécules-sondes, passivation, etc.) nécessiterait une enquête approfondie et un contrôle accru. Nous avons présenté quelques autres métriques de performances et avenues potentielles à l'optimisation de la technologie, mais soulignions que dans

tous les cas, la fiabilité des résultats ne sera garantie que par une bonne caractérisation de la variabilité intra- et inter-dispositifs à l'aide de contrôles positifs et négatifs pertinents, ainsi qu'un nombre de réplicats suffisant.

Cette revue de littérature, particulièrement son aspect critique, nous a permis d'établir les bases pour le reste du projet. Nous avons amorcé une réflexion quant à l'orientation de notre recherche, qui aura directement influencé les thèmes abordés de ce mémoire. En comparant et analysant les différentes façons de mesurer et de caractériser les biocapteurs, nous avons pu établir des protocoles expérimentaux mieux adaptés à nos critères de qualité. Les bonnes pratiques établies dans ce travail sont solides et ne dépendent pas des nouvelles avancées dans le domaine. Toutefois, dans le futur, il sera important de rester au fait des nouveaux développements, particulièrement ceux attrayant à l'interface de détection biologique pouvant nous aider à optimiser la performance de nos biocapteurs. De manière générale, il est souhaitable en tant que laboratoire de pointe de suivre de près tous les développements techniques et technologiques, en gardant l'esprit analytique suggéré dans cette revue.

Créer des systèmes expérimentaux propices à l'étude des TECG.

Dans le chapitre 3, nous quittions les réflexions pour se lancer dans une étape intermédiaire concrète indispensable aux expériences futures. Les systèmes expérimentaux désignent à la fois la production des transistors et la capacité à les mesurer. Le mot «propice» est utilisé comme un synonyme d'optimal, basé sur les critères définis dans le chapitre précédent. En première partie, nous nous sommes concentrées sur la production des capteurs, dont le rendement est directement relié à notre capacité à présenter un ensemble statistique suffisant. Nous avons décrit le protocole de fabrication ainsi que les améliorations apportées. Ces modifications concernent le suivi et la systématisation de la production ainsi que la modification de certaines parties du protocole. De manière générale, les modifications apportées sont liées à la réduction de la contamination et au nettoyage des surfaces des puces. Un système de traçage des puces et des étapes de fabrication ont également été mis en place. Nous rapportons ainsi plus de 250 dispositifs avec un rendement de dispositifs fonctionnels par puce presque doublé. La deuxième partie du chapitre concernait le développement d'une nouvelle instrumentation de mesures électriques. Nous avons commencé par décrire l'ancienne, fonctionnelle, mais limitée par la quantité d'information extraite par mesure. En effet, nous ne pouvions mesurer qu'un dispositif à la fois et la mémoire interne de l'appareil limitait la longueur des séries temporelles. Nous avons décrit la nouvelle instrumentation qui permet de prendre des courbes de sortie, des courbes de transfert et des séries temporelles pour tous les dispositifs d'une puce en parallèle. Pour évaluer la performance du système, nous avons démontré la grande qualité des contacts en extrayant la résistance grâce à des courbes de production, le bon couplage entre le voltage et le courant en comparant des courbes de transfert automatiques et manuelles, l'hystérèse raisonnable des courbes de transfert, la stabilité du PNC pour ces mêmes courbes et la petite amplitude du bruit dans une série temporelle.

Par l'optimisation du rendement de fabrication et de la mesure, nous avons significativement augmenté notre capacité à mener des expériences de qualité. Cette mission est cependant loin d'être terminée. Sur le plan de la fabrication, le rendement du nombre de dispositifs fonctionnels par puce laisse place à l'amélioration, avec un rendement parfait comme objectif final. Il serait naïf de ne pas mentionner l'habileté humaine comme facteur, mais plusieurs autres avenues pourraient aussi être explorées. Mentionnons par exemple la caractérisation de la surface du graphène par des méthodes optiques plus précises comme la microscopie électronique à balayage qui nous permettrait d'avoir une meilleure idée de sa propreté. Ceci permettrait de nous assurer d'avoir accès à un maximum de la surface du graphène lors d'expérience de fonctionnalisation, entre autres. Les nombreuses sources de contamination, particulièrement celles présentes lors du transfert et par la verrerie utilisée lors des manipulations gagneraient à être davantage caractérisées. Nous pourrions également tester des méthodes de recuit pour améliorer l'adhérence du graphène au substrat et solidifier les contacts. Du côté de l'instrumentation, il est aussi possible de prévoir toutes sortes de perfectionnements. Notamment, nous pouvons penser à une amélioration du code d'acquisition de séries temporelles pour pouvoir contrôler l'échelle de l'affichage des données en temps-réel, à l'intégration d'un système automatique programmable pour les injections de solutions, à l'ajout de circuits pour mesurer plusieurs puces en parallèle (le *PXI* peut en mesurer théoriquement jusqu'à quatre), etc. Nous pouvons aussi dépasser les considérations techniques et imaginer toutes sortes de projets intéressants permis par l'architecture de nos puces et de notre appareillage. Par exemple, en extrapolant notre système à plusieurs puces, nous pourrions prendre avantage du réseau de transistor mesurables simultanément pour mettre en place un système analogue aux microréseaux optiques qui sont utilisés pour plusieurs biomolécules comme l'ADN ou les protéines [290]. En travaillant à réduire le bruit provenant du graphène (en le suspendant [291], en construisant des nanorubans de très haute qualité [292]) et de l'instrument de mesure (par des techniques d'échantillonage, une optimisation du circuit comme l'ajout d'une boite de Faraday), nous pourrions utiliser la grande stabilité de notre système ainsi que la très haute vitesse d'échantillonage pour détecter d'infimes changements de conformations moléculaires. Ceci pourrait nous permettre de suivre la cinétique de molécules d'ADN [81], d'autres molécules, ou même d'explorer des stratégies de séquençage d'ADN [293].

Contrôler la fonctionnalisation covalente du graphène.

Comme expliqué lors de notre premier article, une des stratégies pour maximiser le signal produit par la liaison entre cible et sonde lors d'une expérience de biodétection relève du contrôle de la chimie de surface du graphène. La fonctionnalisation permet de relier les sondes au graphène et la maîtrise de sa forme covalente fait partie des grands défis du domaine. Nous avons commencé par démontrer statistiquement que la fonctionnalisation covalente aux sels de diazonium obtenue par une méthode spontanée (la plus commune) est imprévisible et hétérogène. Dans une optique de détection, il est impératif de savoir équilibrer la perte de courant résultant de la liaison covalente avec un taux suffisant de greffons par unité de surface. Nous avons confirmé par plusieurs méthodes que la disponibilité des électrons est le facteur limitant la réaction et que c'est en la contrôlant

qu'on pourra moduler le taux de fonctionnalisation. La méthode présentée consistait à utiliser le voltage de grille comme proxy pour réguler la concentration de porteurs de charge dans le graphène, et donc réguler la réaction de fonctionnalisation. Nous avons démontré un contrôle sur le taux de greffage, confirmé par spectroscopie Raman, ainsi qu'un contrôle sur la vitesse de réaction, que nous pouvions observer en temps-réel. Nous avons prouvé qu'avec le voltage de grille il est possible de débuter et d'arrêter la réaction sur demande, et conséquemment d'obtenir le taux de fonctionnalisation désiré. Cette méthode permet de visualiser la réaction de fonctionnalisation aux sels de diazonium en temps-réel comme jamais auparavant, en plus de permettre des taux de greffage adaptés à des expériences de détection.

La réussite de cette expérience n'aurait pas été possible sans la parallélisation des mesures permises par le *PXI* et ses circuits, mais elle représente beaucoup plus qu'un simple succès technique. La méthode de contrôle de la fonctionnalisation covalente nous est utile régulièrement pour fixer des molécules-sondes sur tous les transistors d'une puce simultanément, puis pour faire des expériences de biodétection. L'utilisation d'une chimie covalente permet de nous assurer de la stabilité des sondes lors des rinçages, un avantage significatif. Notre nouvelle approche nous permet d'atteindre un niveau de précision et de productivité jusqu'alors inégalés. Dans les prochaines étapes de ce projet, il serait intéressant de se pencher sur la quantification du taux de greffage et la distribution spatiale des greffons. Des expériences préliminaires d'imagerie Raman ont été menées en ce sens et méritent d'être poursuivies dans un article futur. Entre autres, il serait intéressant d'étudier l'effet du taux de greffage sur la limite de détection et d'éventuellement identifier une valeur optimale. Nous pourrions aussi tenter de comprendre la cinétique spatiale de la réaction (comparer la réactivité des bords des rubans et celle du centre) ou encore vérifier la réversibilité de la réaction de fonctionnalisation. Il serait également possible d'étudier les effets de la techniques sur d'autres molécules par exemple en testant l'effet du champ électrique sur la fonctionnalisation non-covalente ou sur l'interaction non-spécifique entre des molécules chargées et du graphène. De manière plus générale, ces travaux sur le contrôle de la fonctionnalisation covalente peuvent être considérés comme les premières étapes d'une série d'expériences visant à perfectionner l'assemblage de l'interface de détection biologique de nos capteurs afin d'en améliorer la performance.

Bibliographie

1. Schwierz, F. Graphene Transistors. *Nature Nanotechnology* **5,** 487-496. issn : 1748-3395 (juill. 2010).
2. Naresh, V. & Lee, N. A Review on Biosensors and Recent Development of Nanostructured Materials-Enabled Biosensors. *Sensors* **21,** 1109. issn : 1424-8220 (jan. 2021).
3. Shabaninejad, Z. *et al.* Electrochemical-Based Biosensors for microRNA Detection : Nanotechnology Comes into View. *Analytical Biochemistry* **581,** 113349. issn : 0003-2697 (sept. 2019).
4. Zubiarrain-Laserna, A. & Kruse, P. Review—Graphene-Based Water Quality Sensors. *Journal of The Electrochemical Society* **167,** 037539. issn : 1945-7111 (jan. 2020).
5. Xu, S. Electromechanical Biosensors for Pathogen Detection. *Microchimica Acta* **178,** 245-260. issn : 1436-5073 (sept. 2012).
6. Syu, Y.-C., Hsu, W.-E. & Lin, C.-T. Review—Field-Effect Transistor Biosensing : Devices and Clinical Applications. *ECS Journal of Solid State Science and Technology* **7,** Q3196. issn : 2162-8777 (juin 2018).
7. Wu, D. *et al.* Dual-Aptamer Modified Graphene Field-Effect Transistor Nanosensor for Label-Free and Specific Detection of Hepatocellular Carcinoma-Derived Microvesicles. *Analytical Chemistry* **92,** 4006-4015. issn : 0003-2700 (mars 2020).
8. Budhathoki-Uprety, J. *et al.* Synthetic Molecular Recognition Nanosensor Paint for Microalbuminuria. *Nature Communications* **10,** 1-9. issn : 2041-1723 (août 2019).
9. Ono, T. *et al.* Electrical Biosensing at Physiological Ionic Strength Using Graphene Field-Effect Transistor in Femtoliter Microdroplet. *Nano Letters* **19,** 4004-4009. issn : 1530-6984 (juin 2019).
10. Kwong Hong Tsang, D. *et al.* Chemically Functionalised Graphene FET Biosensor for the Label-free Sensing of Exosomes. *Scientific Reports* **9,** 1-10. issn : 2045-2322 (sept. 2019).
11. Etzioni, R. *et al.* The Case for Early Detection. *Nature Reviews Cancer* **3,** 243-252. issn : 1474-1768 (avr. 2003).

12. Novoselov, K. S. *et al.* Electric Field Effect in Atomically Thin Carbon Films. *Science* **306,** 666-669. issn : 0036-8075, 1095-9203 (oct. 2004).
13. Avouris, P. Graphene : Electronic and Photonic Properties and Devices. *Nano Letters* **10,** 4285-4294. issn : 1530-6984, 1530-6992 (nov. 2010).
14. Castro Neto, A. H., Guinea, F., Peres, N. M. R., Novoselov, K. S. & Geim, A. K. The Electronic Properties of Graphene. *Reviews of Modern Physics* **81,** 109-162 (jan. 2009).
15. Wallace, P. R. The Band Theory of Graphite. *Physical Review* **71,** 622-634 (mai 1947).
16. Geim, A. K. & Novoselov, K. S. The Rise of Graphene. *Nature Materials* **6,** 183-191. issn : 1476-4660 (mars 2007).
17. Novoselov, K. S. *et al.* Two-Dimensional Gas of Massless Dirac Fermions in Graphene. *Nature* **438,** 197-200. issn : 1476-4687 (nov. 2005).
18. Lu, C. L., Chang, C. P., Huang, Y. C., Chen, R. B. & Lin, M. L. Influence of an Electric Field on the Optical Properties of Few-Layer Graphene with AB Stacking. *Physical Review B* **73,** 144427 (avr. 2006).
19. Snoke, D. W. *Electronics : A Physical Approach* isbn : 978-0-321-55133-7 (Pearson, Boston, 2015).
20. Keyes, R. W. Physical Limits of Silicon Transistors and Circuits. *Reports on Progress in Physics* **68,** 2701-2746. issn : 0034-4885 (sept. 2005).
21. Datta, S., Assad, F. & Lundstrom, M. S. The Silicon MOSFET from a Transmission Viewpoint. *Superlattices and Microstructures* **23,** 771-780. issn : 0749-6036 (mars 1998).
22. Lundstrom, M. & Ren, Z. Essential Physics of Carrier Transport in Nanoscale MOSFETs. *IEEE Transactions on Electron Devices* **49,** 133-141. issn : 1557-9646 (jan. 2002).
23. Bokdam, M., Khomyakov, P. A., Brocks, G. & Kelly, P. J. Field Effect Doping of Graphene in Metal$|$dielectric$|$graphene Heterostructures : A Model Based upon First-Principles Calculations. *Physical Review B* **87,** 075414 (fév. 2013).
24. Campos, R. *et al.* Attomolar Label-Free Detection of DNA Hybridization with Electrolyte-Gated Graphene Field-Effect Transistors. *ACS Sensors* **4,** 286-293 (fév. 2019).
25. Ping, J., Vishnubhotla, R., Vrudhula, A. & Johnson, A. T. C. Scalable Production of High-Sensitivity, Label-Free DNA Biosensors Based on Back-Gated Graphene Field Effect Transistors. *ACS Nano* **10,** 8700-8704. issn : 1936-0851 (sept. 2016).
26. Islam, K., Suhail, A. & Pan, G. A Label-Free and Ultrasensitive Immunosensor for Detection of Human Chorionic Gonadotrophin Based on Graphene FETs. *Biosensors* **7,** 27. issn : 2079-6374 (juill. 2017).

27. Jin, X. *et al.* A Field Effect Transistor Modified with Reduced Graphene Oxide for Immunodetection of Ebola Virus. *Microchimica Acta* **186,** 223. issn : 1436-5073 (mars 2019).
28. Zhang, H. *et al.* Aryl Functionalization as a Route to Band Gap Engineering in Single Layer Graphene Devices. *Nano Letters* **11,** 4047-4051. issn : 1530-6984 (oct. 2011).
29. Georgakilas, V. *et al.* Noncovalent Functionalization of Graphene and Graphene Oxide for Energy Materials, Biosensing, Catalytic, and Biomedical Applications. *Chemical Reviews* **116,** 5464-5519. issn : 0009-2665 (mai 2016).
30. Lherbier, A., Blase, X., Niquet, Y.-M., Triozon, F. & Roche, S. Charge Transport in Chemically Doped 2D Graphene. *Physical Review Letters* **101,** 036808 (juill. 2008).
31. Bottari, G. *et al.* Chemical Functionalization and Characterization of Graphene-Based Materials. *Chemical Society Reviews* **46,** 4464-4500. issn : 1460-4744 (juill. 2017).
32. Paulus, G. L. C., Wang, Q. H. & Strano, M. S. Covalent Electron Transfer Chemistry of Graphene with Diazonium Salts. *Accounts of Chemical Research* **46,** 160-170. issn : 0001-4842, 1520-4898 (jan. 2013).
33. Cao, C., Zhang, Y., Jiang, C., Qi, M. & Liu, G. Advances on Aryldiazonium Salt Chemistry Based Interfacial Fabrication for Sensing Applications. *ACS Applied Materials & Interfaces* **9,** 5031-5049. issn : 1944-8244 (fév. 2017).
34. Béraud, A. *et al.* Graphene Field-Effect Transistors as Bioanalytical Sensors : Design, Operation and Performance. *Analyst* **146,** 403-428 (2021).
35. Reina, G. *et al.* Promises, Facts and Challenges for Graphene in Biomedical Applications. *Chemical Society Reviews* **46,** 4400-4416. issn : 1460-4744 (juill. 2017).
36. Rogers, K. R. Biosensors for Environmental Applications. *Biosensors and Bioelectronics* **10,** 533-541. issn : 0956-5663 (jan. 1995).
37. Vaidya, A. M. & Annapure, U. S. in *Enzymes in Food Biotechnology* (éd. Kuddus, M.) 659-674 (Academic Press, jan. 2019). isbn : 978-0-12-813280-7.
38. Kokkinos, C. Electrochemical DNA Biosensors Based on Labeling with Nanoparticles. *Nanomaterials* **9,** 1361 (oct. 2019).
39. Sapsford, K. E., Pons, T., Medintz, I. L. & Mattoussi, H. Biosensing with Luminescent Semiconductor Quantum Dots. *Sensors (Basel, Switzerland)* **6,** 925-953. issn : 1424-8220 (août 2006).
40. Feng, Y., Zhang, Y., Ying, C., Wang, D. & Du, C. Nanopore-Based Fourth-generation DNA Sequencing Technology. *Genomics, Proteomics & Bioinformatics* **13,** 4-16. issn : 1672-0229 (fév. 2015).
41. Li, Z., Zhang, W. & Xing, F. Graphene Optical Biosensors. *International Journal of Molecular Sciences* **20,** 2461 (jan. 2019).

42. Kruss, S. *et al.* Carbon Nanotubes as Optical Biomedical Sensors. *Advanced Drug Delivery Reviews. Carbon Nanotubes in Medicine and Biology : Therapy and Diagnostics & Safety and Toxicology* **65,** 1933-1950. issn : 0169-409X (déc. 2013).
43. Tîlmaciu, C.-M. & Morris, M. C. Carbon Nanotube Biosensors. *Frontiers in Chemistry* **3.** issn : 2296-2646 (2015).
44. Coroş, M., Pruneanu, S. & Staden, R.-I. S.-v. Review—Recent Progress in the Graphene-Based Electrochemical Sensors and Biosensors. *Journal of The Electrochemical Society* **167,** 037528. issn : 1945-7111 (déc. 2019).
45. Zang, X., Zhou, Q., Chang, J., Liu, Y. & Lin, L. Graphene and Carbon Nanotube (CNT) in MEMS/NEMS Applications. *Microelectronic Engineering. Micro and Nanofabrication Breakthroughs for Electronics, MEMS and Life Sciences* **132,** 192-206. issn : 0167-9317 (jan. 2015).
46. Schöning, M. J. & Poghossian, A. Recent Advances in Biologically Sensitive Field-Effect Transistors (BioFETs). *Analyst* **127,** 1137-1151. issn : 1364-5528 (sept. 2002).
47. Caras, S. & Janata, J. Field Effect Transistor Sensitive to Penicillin. *Analytical Chemistry* **52,** 1935-1937. issn : 0003-2700 (oct. 1980).
48. Mao, S. *et al.* Two-Dimensional Nanomaterial-Based Field-Effect Transistors for Chemical and Biological Sensing. *Chemical Society Reviews* **46,** 6872-6904. issn : 1460-4744 (nov. 2017).
49. Noy, A., Artyukhin, A. B. & Misra, N. Bionanoelectronics with 1D Materials. *Materials Today* **12,** 22-31. issn : 1369-7021 (sept. 2009).
50. Mu, L. *et al.* Silicon Nanowire Field-Effect Transistors—A Versatile Class of Potentiometric Nanobiosensors. *IEEE Access* **3,** 287-302. issn : 2169-3536 (2015).
51. Allen, B. L., Kichambare, P. D. & Star, A. Carbon Nanotube Field-Effect-Transistor-Based Biosensors. *Advanced Materials* **19,** 1439-1451. issn : 1521-4095 (2007).
52. Hou, G., Zhang, L., Ng, V., Wu, Z. & Schulz, M. Review of Recent Advances in Carbon Nanotube Biosensors Based on Field-Effect Transistors. *Nano LIFE* **06,** 1642006. issn : 1793-9844 (août 2016).
53. Wang, J. *et al.* Point Decoration of Silicon Nanowires : An Approach Toward Single-Molecule Electrical Detection. *Angewandte Chemie International Edition* **53,** 5038-5043. issn : 1521-3773 (2014).
54. Choi, Y. *et al.* Single-Molecule Lysozyme Dynamics Monitored by an Electronic Circuit. *Science* **335,** 319-324. issn : 0036-8075, 1095-9203 (jan. 2012).
55. Bouilly, D. *et al.* Single-Molecule Reaction Chemistry in Patterned Nanowells. *Nano Letters* **16,** 4679-4685. issn : 1530-6984 (juill. 2016).

56. Das, S., Robinson, J. A., Dubey, M., Terrones, H. & Terrones, M. Beyond Graphene : Progress in Novel Two-Dimensional Materials and van Der Waals Solids. *Annual Review of Materials Research* **45,** 1-27 (2015).
57. Duong, D. L., Yun, S. J. & Lee, Y. H. Van Der Waals Layered Materials : Opportunities and Challenges. *ACS Nano* **11,** 11803-11830. issn : 1936-0851 (déc. 2017).
58. Zhong, Y., Zhen, Z. & Zhu, H. Graphene : Fundamental Research and Potential Applications. *FlatChem* **4,** 20-32. issn : 2452-2627 (août 2017).
59. Brown, M. A., Crosser, M. S., Leyden, M. R., Qi, Y. & Minot, E. D. Measurement of High Carrier Mobility in Graphene in an Aqueous Electrolyte Environment. *Applied Physics Letters* **109,** 093104. issn : 0003-6951 (août 2016).
60. Huang, C., Hao, Z., Qi, T., Pan, Y. & Zhao, X. An Integrated Flexible and Reusable Graphene Field Effect Transistor Nanosensor for Monitoring Glucose. *Journal of Materiomics.* issn : 2352-8478 (fév. 2020).
61. Zhan, B. *et al.* Graphene Field-Effect Transistor and Its Application for Electronic Sensing. *Small* **10,** 4042-4065. issn : 1613-6829 (2014).
62. Schedin, F. *et al.* Detection of Individual Gas Molecules Adsorbed on Graphene. *Nature Materials* **6,** 652-655. issn : 1476-1122, 1476-4660 (sept. 2007).
63. Mao, S., Lu, G. & Chen, J. Nanocarbon-Based Gas Sensors : Progress and Challenges. *Journal of Materials Chemistry A* **2,** 5573-5579. issn : 2050-7496 (mars 2014).
64. Fakih, I., Mahvash, F., Siaj, M. & Szkopek, T. Sensitive Precise $p\mathrm{H}$ Measurement with Large-Area Graphene Field-Effect Transistors at the Quantum-Capacitance Limit. *Physical Review Applied* **8,** 044022 (oct. 2017).
65. Zhu, Y. *et al.* A Solid Dielectric Gated Graphene Nanosensor in Electrolyte Solutions. *Applied Physics Letters* **106,** 123503. issn : 0003-6951 (mars 2015).
66. Mohanty, N. & Berry, V. Graphene-Based Single-Bacterium Resolution Biodevice and DNA Transistor : Interfacing Graphene Derivatives with Nanoscale and Microscale Biocomponents. *Nano Letters* **8,** 4469-4476. issn : 1530-6984 (déc. 2008).
67. Sudibya, H. G., He, Q., Zhang, H. & Chen, P. Electrical Detection of Metal Ions Using Field-Effect Transistors Based on Micropatterned Reduced Graphene Oxide Films. *ACS Nano* **5,** 1990-1994. issn : 1936-0851 (mars 2011).
68. Li, Y. *et al.* Fully Integrated Graphene Electronic Biosensor for Label-Free Detection of Lead (II) Ion Based on G-quadruplex Structure-Switching. *Biosensors and Bioelectronics* **89,** 758-763. issn : 0956-5663 (mars 2017).
69. Zhu, Y. *et al.* A Graphene-Based Affinity Nanosensor for Detection of Low-Charge and Low-Molecular-Weight Molecules. *Nanoscale* **8,** 5815-5819. issn : 2040-3372 (mars 2016).

70. Kim, D.-J. *et al.* Reduced Graphene Oxide Field-Effect Transistor for Label-Free Femtomolar Protein Detection. *Biosensors and Bioelectronics* **41,** 621-626. issn : 0956-5663 (mars 2013).
71. Cai, B. *et al.* Ultrasensitive Label-Free Detection of PNA–DNA Hybridization by Reduced Graphene Oxide Field-Effect Transistor Biosensor. *ACS Nano* **8,** 2632-2638. issn : 1936-0851 (mars 2014).
72. Hwang, M. T. *et al.* Highly Specific SNP Detection Using 2D Graphene Electronics and DNA Strand Displacement. *Proceedings of the National Academy of Sciences* **113,** 7088-7093. issn : 0027-8424, 1091-6490 (juin 2016).
73. Huang, Y., Dong, X., Liu, Y., Li, L.-J. & Chen, P. Graphene-Based Biosensors for Detection of Bacteria and Their Metabolic Activities. *Journal of Materials Chemistry* **21,** 12358-12362. issn : 1364-5501 (août 2011).
74. Thakur, B. *et al.* Rapid Detection of Single E. Coli Bacteria Using a Graphene-Based Field-Effect Transistor Device. *Biosensors and Bioelectronics* **110,** 16-22. issn : 0956-5663 (juill. 2018).
75. Liu, F., Kim, Y. H., Cheon, D. S. & Seo, T. S. Micropatterned Reduced Graphene Oxide Based Field-Effect Transistor for Real-Time Virus Detection. *Sensors and Actuators B : Chemical* **186,** 252-257. issn : 0925-4005 (sept. 2013).
76. Kim, J. W., Kim, S., Jang, Y.-h., Lim, K.-i. & Lee, W. H. Attomolar Detection of Virus by Liquid Coplanar-Gate Graphene Transistor on Plastic. *Nanotechnology* **30,** 345502. issn : 0957-4484 (mai 2019).
77. Lerner, M. B. *et al.* Scalable Production of Highly Sensitive Nanosensors Based on Graphene Functionalized with a Designed G Protein-Coupled Receptor. *Nano Letters* **14,** 2709-2714. issn : 1530-6984 (mai 2014).
78. Chen, X. *et al.* Ultratrace Antibiotic Sensing Using Aptamer/Graphene-Based Field-Effect Transistors. *Biosensors and Bioelectronics* **126,** 664-671. issn : 0956-5663 (fév. 2019).
79. Jiang, S. *et al.* Real-Time Electrical Detection of Nitric Oxide in Biological Systems with Sub-Nanomolar Sensitivity. *Nature Communications* **4,** 1-7. issn : 2041-1723 (juill. 2013).
80. Wang, Z. *et al.* Free Radical Sensors Based on Inner-Cutting Graphene Field-Effect Transistors. *Nature Communications* **10,** 1544. issn : 2041-1723 (avr. 2019).
81. Xu, S. *et al.* Real-Time Reliable Determination of Binding Kinetics of DNA Hybridization Using a Multi-Channel Graphene Biosensor. *Nature Communications* **8,** 1-10. issn : 2041-1723 (mars 2017).
82. Zuccaro, L. *et al.* Real-Time Label-Free Direct Electronic Monitoring of Topoisomerase Enzyme Binding Kinetics on Graphene. *ACS Nano* **9,** 11166-11176. issn : 1936-0851 (nov. 2015).

83. Hajian, R. *et al.* Detection of Unamplified Target Genes via CRISPR–Cas9 Immobilized on a Graphene Field-Effect Transistor. *Nature Biomedical Engineering* **3,** 427-437. issn : 2157-846X (juin 2019).
84. Islam, S. *et al.* Microfluidic-Based Graphene Field Effect Transistor for Femtomolar Detection of Chlorpyrifos. *Scientific Reports* **9,** 1-7. issn : 2045-2322 (jan. 2019).
85. Gao, Z. *et al.* Detection of Sub-fM DNA with Target Recycling and Self-Assembly Amplification on Graphene Field-Effect Biosensors. *Nano Letters* **18,** 3509-3515. issn : 1530-6984 (juin 2018).
86. Vishnubhotla, R. *et al.* Attomolar Detection of ssDNA without Amplification and Capture of Long Target Sequences with Graphene Biosensors. *IEEE Sensors Journal,* 1-1. issn : 1558-1748 (2020).
87. Hwang, M. T. *et al.* Ultrasensitive Detection of Nucleic Acids Using Deformed Graphene Channel Field Effect Biosensors. *Nature Communications* **11,** 1543. issn : 2041-1723 (mars 2020).
88. Chan, C., Shi, J., Fan, Y. & Yang, M. A Microfluidic Flow-through Chip Integrated with Reduced Graphene Oxide Transistor for Influenza Virus Gene Detection. *Sensors and Actuators B : Chemical* **251,** 927-933. issn : 0925-4005 (nov. 2017).
89. Wang, X., Hao, Z., Olsen, T. R., Zhang, W. & Lin, Q. Measurements of Aptamer–Protein Binding Kinetics Using Graphene Field-Effect Transistors. *Nanoscale* **11,** 12573-12581. issn : 2040-3372 (juill. 2019).
90. Khan, N. I., Mousazadehkasin, M., Ghosh, S., Tsavalas, J. G. & Song, E. An Integrated Microfluidic Platform for Selective and Real-Time Detection of Thrombin Biomarkers Using a Graphene FET. *Analyst* **145,** 4494-4503. issn : 1364-5528 (juin 2020).
91. Xu, G. *et al.* Electrophoretic and Field-Effect Graphene for All-Electrical DNA Array Technology. *Nature Communications* **5,** 4866. issn : 2041-1723 (sept. 2014).
92. Saltzgaber, G. *et al.* Scalable Graphene Field-Effect Sensors for Specific Protein Detection. *Nanotechnology* **24,** 355502. issn : 0957-4484 (août 2013).
93. Fu, W. *et al.* Biosensing near the Neutrality Point of Graphene. *Science Advances* **3,** e1701247. issn : 2375-2548 (oct. 2017).
94. Forsyth, R., Devadoss, A. & Guy, O. J. Graphene Field Effect Transistors for Biomedical Applications : Current Status and Future Prospects. *Diagnostics* **7,** 45 (sept. 2017).
95. Terse-Thakoor, T., Badhulika, S. & Mulchandani, A. Graphene Based Biosensors for Healthcare. *Journal of Materials Research* **32,** 2905-2929. issn : 0884-2914, 2044-5326 (août 2017).
96. Szunerits, S. & Boukherroub, R. Graphene-Based Biosensors. *Interface Focus* **8,** 20160132 (juin 2018).

97. Wu, X., Mu, F., Wang, Y. & Zhao, H. Graphene and Graphene-Based Nanomaterials for DNA Detection : A Review. *Molecules* **23,** 2050 (août 2018).
98. Xu, L. *et al.* Graphene-Based Biosensors for the Detection of Prostate Cancer Protein Biomarkers : A Review. *BMC Chemistry* **13,** 112. issn : 2661-801X (sept. 2019).
99. Salvo, P. *et al.* Graphene-Based Devices for Measuring pH. *Sensors and Actuators B : Chemical* **256,** 976-991. issn : 0925-4005 (mars 2018).
100. Papageorgiou, D. G., Kinloch, I. A. & Young, R. J. Mechanical Properties of Graphene and Graphene-Based Nanocomposites. *Progress in Materials Science* **90,** 75-127. issn : 0079-6425 (oct. 2017).
101. Bonaccorso, F., Sun, Z., Hasan, T. & Ferrari, A. C. Graphene Photonics and Optoelectronics. *Nature Photonics* **4,** 611-622. issn : 1749-4893 (sept. 2010).
102. Geim, A. K. & Novoselov, K. S. The Rise of Graphene. *Nature Materials* **6,** 183-191. issn : 1476-4660 (mars 2007).
103. Kumar Srivastava, P. & Ghosh, S. Eliminating Defects from Graphene Monolayers during Chemical Exfoliation. *Applied Physics Letters* **102,** 043102. issn : 0003-6951 (jan. 2013).
104. Yi, M. & Shen, Z. A Review on Mechanical Exfoliation for the Scalable Production of Graphene. *Journal of Materials Chemistry A* **3,** 11700-11715. issn : 2050-7496 (mai 2015).
105. Chen, Y., Michael, Z. P., Kotchey, G. P., Zhao, Y. & Star, A. Electronic Detection of Bacteria Using Holey Reduced Graphene Oxide. *ACS Applied Materials & Interfaces* **6,** 3805-3810. issn : 1944-8244 (mars 2014).
106. Chen, X., Zhang, L. & Chen, S. Large Area CVD Growth of Graphene. *Synthetic Metals. Reviews of Current Advances in Graphene Science and Technology* **210,** 95-108. issn : 0379-6779 (déc. 2015).
107. De Heer, W. A. *et al.* Large Area and Structured Epitaxial Graphene Produced by Confinement Controlled Sublimation of Silicon Carbide. *Proceedings of the National Academy of Sciences* **108,** 16900-16905. issn : 0027-8424, 1091-6490 (oct. 2011).
108. Chen, B. *et al.* How Good Can CVD-grown Monolayer Graphene Be ? *Nanoscale* **6,** 15255-15261. issn : 2040-3372 (nov. 2014).
109. Xu, S. *et al.* Ultrasensitive Label-Free Detection of DNA Hybridization by Sapphire-Based Graphene Field-Effect Transistor Biosensor. *Applied Surface Science* **427,** 1114-1119. issn : 0169-4332 (jan. 2018).
110. Chang, J. *et al.* Ultrasonic-Assisted Self-Assembly of Monolayer Graphene Oxide for Rapid Detection of Escherichia Coli Bacteria. *Nanoscale* **5,** 3620-3626 (2013).
111. Wojtoniszak, M. *et al.* Synthesis, Dispersion, and Cytocompatibility of Graphene Oxide and Reduced Graphene Oxide. *Colloids and Surfaces B : Biointerfaces* **89,** 79-85. issn : 0927-7765 (jan. 2012).

112. Negishi, R. & Kobayashi, Y. Extraordinary Suppression of Carrier Scattering in Large Area Graphene Oxide Films. *Applied Physics Letters* **105,** 253502. issn : 0003-6951 (déc. 2014).
113. Li, P., Liu, B., Zhang, D., Sun, Y. & Liu, J. Graphene Field-Effect Transistors with Tunable Sensitivity for High Performance Hg (II) Sensing. *Applied Physics Letters* **109,** 153101. issn : 0003-6951 (oct. 2016).
114. Okamoto, S., Ohno, Y., Maehashi, K., Inoue, K. & Matsumoto, K. Immunosensors Based on Graphene Field-Effect Transistors Fabricated Using Antigen-Binding Fragment. *Japanese Journal of Applied Physics* **51,** 06FD08. issn : 1347-4065 (juin 2012).
115. Fu, W., Jiang, L., van Geest, E. P., Lima, L. M. C. & Schneider, G. F. Sensing at the Surface of Graphene Field-Effect Transistors. *Advanced Materials* **29,** 1603610. issn : 1521-4095 (2017).
116. You, X. & Pak, J. J. Graphene-Based Field Effect Transistor Enzymatic Glucose Biosensor Using Silk Protein for Enzyme Immobilization and Device Substrate. *Sensors and Actuators B : Chemical* **202,** 1357-1365. issn : 0925-4005 (oct. 2014).
117. Cagang, A. A. *et al.* Graphene-Based Field Effect Transistor in Two-Dimensional Paper Networks. *Analytica Chimica Acta* **917,** 101-106. issn : 0003-2670 (avr. 2016).
118. Huang, Y. *et al.* Reliable Exfoliation of Large-Area High-Quality Flakes of Graphene and Other Two-Dimensional Materials. *ACS Nano* **9,** 10612-10620. issn : 1936-0851 (nov. 2015).
119. Chen, Y., Gong, X.-L. & Gai, J.-G. Progress and Challenges in Transfer of Large-Area Graphene Films. *Advanced Science* **3,** 1500343. issn : 2198-3844 (2016).
120. Gao, L. *et al.* Repeated Growth and Bubbling Transfer of Graphene with Millimetre-Size Single-Crystal Grains Using Platinum. *Nature Communications* **3,** 1-7. issn : 2041-1723 (fév. 2012).
121. Cherian, C. T. *et al.* 'Bubble-Free' Electrochemical Delamination of CVD Graphene Films. *Small* **11,** 189-194. issn : 1613-6829 (2015).
122. Suk, J. W. *et al.* Transfer of CVD-Grown Monolayer Graphene onto Arbitrary Substrates. *ACS Nano* **5,** 6916-6924. issn : 1936-0851 (sept. 2011).
123. Wang, X., Zhi, L. & Müllen, K. Transparent, Conductive Graphene Electrodes for Dye-Sensitized Solar Cells. *Nano Letters* **8,** 323-327. issn : 1530-6984 (jan. 2008).
124. Eda, G., Fanchini, G. & Chhowalla, M. Large-Area Ultrathin Films of Reduced Graphene Oxide as a Transparent and Flexible Electronic Material. *Nature Nanotechnology* **3,** 270-274. issn : 1748-3395 (mai 2008).
125. Wang, S. *et al.* Graphene Field-Effect Transistor Biosensor for Detection of Biotin with Ultrahigh Sensitivity and Specificity. *Biosensors and Bioelectronics* **165,** 112363. issn : 0956-5663 (oct. 2020).

126. Maehashi, K. *et al.* Selective Ion Sensors Based on Ionophore-Modified Graphene Field-Effect Transistors. *Sensors and Actuators B : Chemical. Selected Papers from the 14th International Meeting on Chemical Sensors* **187,** 45-49. issn : 0925-4005 (oct. 2013).
127. Farid, S. *et al.* Detection of Interferon Gamma Using Graphene and Aptamer Based FET-like Electrochemical Biosensor. *Biosensors and Bioelectronics* **71,** 294-299. issn : 0956-5663 (sept. 2015).
128. Minot, E. D. *et al.* Carbon Nanotube Biosensors : The Critical Role of the Reference Electrode. *Applied Physics Letters* **91,** 093507. issn : 0003-6951 (août 2007).
129. Chen, T.-Y. *et al.* Label-Free Detection of DNA Hybridization Using Transistors Based on CVD Grown Graphene. *Biosensors and Bioelectronics* **41,** 103-109. issn : 0956-5663 (mars 2013).
130. Dong, X., Shi, Y., Huang, W., Chen, P. & Li, L.-J. Electrical Detection of DNA Hybridization with Single-Base Specificity Using Transistors Based on CVD-Grown Graphene Sheets. *Advanced Materials* **22,** 1649-1653. issn : 1521-4095 (2010).
131. Yu, C. *et al.* Creation of Reduced Graphene Oxide Based Field Effect Transistors and Their Utilization in the Detection and Discrimination of Nucleoside Triphosphates. *ACS Applied Materials & Interfaces* **7,** 10718-10726. issn : 1944-8244 (mai 2015).
132. Yin, Z. *et al.* Real-Time DNA Detection Using Pt Nanoparticle -Decorated Reduced Graphene Oxide Field-Effect Transistors. *Nanoscale* **4,** 293-297 (2012).
133. Kim, J. W. *et al.* Liquid Coplanar-Gate Organic/Graphene Hybrid Electronics for Label-Free Detection of Single and Double-Stranded DNA Molecules. *Organic Electronics* **62,** 163-167. issn : 1566-1199 (nov. 2018).
134. Kim, H. E., Schuck, A., Lee, J. H. & Kim, Y.-S. Solution-Gated Graphene Field Effect Transistor for TP53 DNA Sensor with Coplanar Electrode Array. *Sensors and Actuators B : Chemical* **291,** 96-101. issn : 0925-4005 (juill. 2019).
135. Du, X., Guo, H., Jin, Y., Jin, Q. & Zhao, J. Electrochemistry Investigation on the Graphene/Electrolyte Interface. *Electroanalysis* **27,** 2760-2765. issn : 1521-4109 (2015).
136. Lin, Y.-M. *et al.* 100-GHz Transistors from Wafer-Scale Epitaxial Graphene. *Science* **327,** 662-662. issn : 0036-8075, 1095-9203 (fév. 2010).
137. Chen, F., Qing, Q., Xia, J., Li, J. & Tao, N. Electrochemical Gate-Controlled Charge Transport in Graphene in Ionic Liquid and Aqueous Solution. *Journal of the American Chemical Society* **131,** 9908-9909. issn : 0002-7863 (juill. 2009).
138. Owczarzy, R., Moreira, B. G., You, Y., Behlke, M. A. & Walder, J. A. Predicting Stability of DNA Duplexes in Solutions Containing Magnesium and Monovalent Cations. *Biochemistry* **47,** 5336-5353. issn : 0006-2960 (mai 2008).

139. Kim, C.-H., Yoo, S.-W., Nam, D.-W., Seo, S. & Lee, J.-H. Effect of Temperature and Humidity on $\hboxNO_2$ and $\hboxNH_3$ Gas Sensitivity of Bottom-Gate Graphene FETs Prepared by ICP-CVD. *IEEE Electron Device Letters* **33,** 1084-1086. issn : 1558-0563 (juill. 2012).
140. Oshin, O. *et al.* Graphene-Based Biosensor for Early Detection of Iron Deficiency. *Sensors* **20,** 3688 (jan. 2020).
141. Islam, S. *et al.* A Smart Nanosensor for the Detection of Human Immunodeficiency Virus and Associated Cardiovascular and Arthritis Diseases Using Functionalized Graphene-Based Transistors. *Biosensors and Bioelectronics* **126,** 792-799. issn : 0956-5663 (fév. 2019).
142. Chang, J. *et al.* Real-Time Detection of Mercury Ions in Water Using a Reduced Graphene Oxide/DNA Field-Effect Transistor with Assistance of a Passivation Layer. *Sensing and Bio-Sensing Research* **5,** 97-104. issn : 2214-1804 (sept. 2015).
143. Fakih, I. *et al.* High Resolution Potassium Sensing with Large-Area Graphene Field-Effect Transistors. *Sensors and Actuators B : Chemical* **291,** 89-95. issn : 0925-4005 (juill. 2019).
144. Zhou, G. *et al.* Real-Time, Selective Detection of Pb2+ in Water Using a Reduced Graphene Oxide/Gold Nanoparticle Field-Effect Transistor Device. *ACS Applied Materials & Interfaces* **6,** 19235-19241. issn : 1944-8244 (nov. 2014).
145. Wang, C. *et al.* A Label-Free and Portable Graphene FET Aptasensor for Children Blood Lead Detection. *Scientific Reports* **6,** 1-8. issn : 2045-2322 (fév. 2016).
146. Tu, J. *et al.* Graphene FET Array Biosensor Based on ssDNA Aptamer for Ultrasensitive Hg2+ Detection in Environmental Pollutants. *Frontiers in Chemistry* **6.** issn : 2296-2646 (2018).
147. An, J. H., Park, S. J., Kwon, O. S., Bae, J. & Jang, J. High-Performance Flexible Graphene Aptasensor for Mercury Detection in Mussels. *ACS Nano* **7,** 10563-10571. issn : 1936-0851 (déc. 2013).
148. Kim, D. H. *et al.* Detection of Alpha-Fetoprotein in Hepatocellular Carcinoma Patient Plasma with Graphene Field-Effect Transistor. *Sensors (Basel, Switzerland)* **18.** issn : 1424-8220 (nov. 2018).
149. Ganguli, A. *et al.* High Sensitivity Graphene Field Effect Transistor-Based Detection of DNA Amplification. *Advanced Functional Materials* **30,** 2001031. issn : 1616-3028 (2020).
150. Zheng, C. *et al.* Fabrication of Ultrasensitive Field-Effect Transistor DNA Biosensors by a Directional Transfer Technique Based on CVD-Grown Graphene. *ACS Applied Materials & Interfaces* **7,** 16953-16959. issn : 1944-8244 (août 2015).

151. Sia, S. K. & Whitesides, G. M. Microfluidic Devices Fabricated in Poly(Dimethylsiloxane) for Biological Studies. *ELECTROPHORESIS* **24,** 3563-3576. issn : 1522-2683 (2003).
152. Qin, D., Xia, Y. & Whitesides, G. M. Soft Lithography for Micro- and Nanoscale Patterning. *Nature Protocols* **5,** 491-502. issn : 1750-2799 (mars 2010).
153. Tarasov, A. *et al.* Gold-Coated Graphene Field-Effect Transistors for Quantitative Analysis of Protein–Antibody Interactions. *2D Materials* **2,** 044008. issn : 2053-1583 (nov. 2015).
154. Kumar, S. & Parekh, S. H. Linking Graphene-Based Material Physicochemical Properties with Molecular Adsorption, Structure and Cell Fate. *Communications Chemistry* **3,** 1-11. issn : 2399-3669 (jan. 2020).
155. Kakatkar, A., Abhilash, T. S., Alba, R. D., Parpia, J. M. & Craighead, H. G. Detection of DNA and Poly-l-Lysine Using CVD Graphene-Channel FET Biosensors. *Nanotechnology* **26,** 125502. issn : 0957-4484 (mars 2015).
156. Dontschuk, N. *et al.* A Graphene Field-Effect Transistor as a Molecule-Specific Probe of DNA Nucleobases. *Nature Communications* **6,** 1-7. issn : 2041-1723 (mars 2015).
157. Stine, R., Robinson, J. T., Sheehan, P. E. & Tamanaha, C. R. Real-Time DNA Detection Using Reduced Graphene Oxide Field Effect Transistors. *Advanced Materials* **22,** 5297-5300. issn : 1521-4095 (2010).
158. Guo, S.-R. *et al.* Label Free DNA Detection Using Large Area Graphene Based Field Effect Transistor Biosensors. *Journal of Nanoscience and Nanotechnology* **11,** 5258-5263 (juin 2011).
159. Seo, G. *et al.* Rapid Detection of COVID-19 Causative Virus (SARS-CoV-2) in Human Nasopharyngeal Swab Specimens Using Field-Effect Transistor-Based Biosensor. *ACS Nano* **14,** 5135-5142. issn : 1936-0851 (avr. 2020).
160. Zhang, X. *et al.* Electrical Probing of COVID-19 Spike Protein Receptor Binding Domain via a Graphene Field-Effect Transistor. *arXiv e-prints,* 20 (2020).
161. Yüce, M. & Kurt, H. How to Make Nanobiosensors : Surface Modification and Characterisation of Nanomaterials for Biosensing Applications. *RSC Advances* **7,** 49386-49403. issn : 2046-2069 (oct. 2017).
162. Hao, Z. *et al.* Modulating the Linker Immobilization Density on Aptameric Graphene Field Effect Transistors Using an Electric Field. *ACS Sensors* **5,** 2503-2513 (août 2020).
163. Gao, N. *et al.* Specific Detection of Biomolecules in Physiological Solutions Using Graphene Transistor Biosensors. *Proceedings of the National Academy of Sciences* **113,** 14633-14638. issn : 0027-8424, 1091-6490 (déc. 2016).
164. De Moraes, A. C. M. & Kubota, L. T. Recent Trends in Field-Effect Transistors-Based Immunosensors. *Chemosensors* **4,** 20 (déc. 2016).

165. Paulus, G. L. C., Wang, Q. H. & Strano, M. S. Covalent Electron Transfer Chemistry of Graphene with Diazonium Salts. *Accounts of Chemical Research* **46,** 160-170. issn : 0001-4842 (jan. 2013).
166. Baraket, M. *et al.* Aminated Graphene for DNA Attachment Produced via Plasma Functionalization. *Applied Physics Letters* **100,** 233123. issn : 0003-6951 (juin 2012).
167. Park, J. & Yan, M. Covalent Functionalization of Graphene with Reactive Intermediates. *Accounts of Chemical Research* **46,** 181-189. issn : 0001-4842 (jan. 2013).
168. Kim, D.-J. *et al.* Electrical Graphene Aptasensor for Ultra-Sensitive Detection of Anthrax Toxin with Amplified Signal Transduction. *Small* **9,** 3352-3360. issn : 1613-6829 (2013).
169. Mao, S., Lu, G., Yu, K., Bo, Z. & Chen, J. Specific Protein Detection Using Thermally Reduced Graphene Oxide Sheet Decorated with Gold Nanoparticle-Antibody Conjugates. *Advanced Materials* **22,** 3521-3526. issn : 1521-4095 (2010).
170. Zhang, X. *et al.* Ultrasensitive Field-Effect Biosensors Enabled by the Unique Electronic Properties of Graphene. *Small* **n/a,** 1902820. issn : 1613-6810 (oct. 2019).
171. Gebbie, M. A. *et al.* Long Range Electrostatic Forces in Ionic Liquids. *Chemical Communications* **53,** 1214-1224. issn : 1364-548X (jan. 2017).
172. Chen, F., Qing, Q., Xia, J. & Tao, N. Graphene Field-Effect Transistors : Electrochemical Gating, Interfacial Capacitance, and Biosensing Applications. *Chemistry – An Asian Journal* **5,** 2144-2153. issn : 1861-471X (2010).
173. Ren, Y. *et al.* Detection of Sulfur Dioxide Gas with Graphene Field Effect Transistor. *Applied Physics Letters* **100,** 163114. issn : 0003-6951 (avr. 2012).
174. Genereux, J. C. & Barton, J. K. Mechanisms for DNA Charge Transport. *Chemical Reviews* **110,** 1642-1662. issn : 0009-2665 (mars 2010).
175. Champlain, J. G. A First Principles Theoretical Examination of Graphene-Based Field Effect Transistors. *Journal of Applied Physics* **109,** 084515. issn : 0021-8979 (avr. 2011).
176. Chen, J. .-. *et al.* Diffusive Charge Transport in Graphene on SiO2. *Solid State Communications. Recent Progress in Graphene Studies* **149,** 1080-1086. issn : 0038-1098 (juill. 2009).
177. Akbari, E., Nabipour, N., Hadavi, S. M. & Nilashi, M. Analytical Investigation of Ion-Sensitive Field Effect Transistor Based on Graphene. *Journal of Materials Science : Materials in Electronics.* issn : 1573-482X (mars 2020).
178. Li, H. *et al.* Graphene Field Effect Transistors for Highly Sensitive and Selective Detection of K+ Ions. *Sensors and Actuators B : Chemical* **253,** 759-765. issn : 0925-4005 (déc. 2017).

179. Yuan, Q. *et al.* Sensitivity Enhancement of Potassium Ion (K+) Detection Based on Graphene Field-Effect Transistors with Surface Plasma Pretreatment. *Sensors and Actuators B : Chemical* **285,** 333-340. issn : 0925-4005 (avr. 2019).
180. Xu, K. *et al.* Graphene- and Aptamer-Based Electrochemical Biosensor. *Nanotechnology* **25,** 205501. issn : 0957-4484 (avr. 2014).
181. Huang, X.-M., Liu, L.-Z., Zhou, S. & Zhao, J.-J. Physical Properties and Device Applications of Graphene Oxide. *Frontiers of Physics* **15,** 33301. issn : 2095-0470 (jan. 2020).
182. Manoharan, A. K., Chinnathambi, S., Jayavel, R. & Hanagata, N. Simplified Detection of the Hybridized DNA Using a Graphene Field Effect Transistor. *Science and Technology of Advanced Materials* **18,** 43-50. issn : 1468-6996 (jan. 2017).
183. Cai, B. *et al.* Gold Nanoparticles-Decorated Graphene Field-Effect Transistor Biosensor for Femtomolar MicroRNA Detection. *Biosensors and Bioelectronics* **74,** 329-334. issn : 0956-5663 (déc. 2015).
184. Chen, S. *et al.* Donor Effect Dominated Molybdenum Disulfide/Graphene Nanostructure-Based Field-Effect Transistor for Ultrasensitive DNA Detection. *Biosensors and Bioelectronics* **156,** 112128. issn : 0956-5663 (mai 2020).
185. Gowtham, S., Scheicher, R. H., Ahuja, R., Pandey, R. & Karna, S. P. Physisorption of Nucleobases on Graphene : Density-functional Calculations. *Physical Review B* **76,** 033401 (juill. 2007).
186. Antony, J. & Grimme, S. Structures and Interaction Energies of Stacked Graphene–Nucleobase Complexes. *Physical Chemistry Chemical Physics* **10,** 2722-2729. issn : 1463-9084 (mai 2008).
187. Lin, C.-T. *et al.* Label-Free Electrical Detection of DNA Hybridization on Graphene Using Hall Effect Measurements : Revisiting the Sensing Mechanism. *Advanced Functional Materials* **23,** 2301-2307. issn : 1616-3028 (2013).
188. Kokil, A., Yang, K. & Kumar, J. Techniques for Characterization of Charge Carrier Mobility in Organic Semiconductors. *Journal of Polymer Science Part B : Polymer Physics* **50,** 1130-1144. issn : 1099-0488 (2012).
189. Liang, X., Fu, Z. & Chou, S. Y. Graphene Transistors Fabricated via Transfer-Printing In Device Active-Areas on Large Wafer. *Nano Letters* **7,** 3840-3844. issn : 1530-6984 (déc. 2007).
190. Bolotin, K. I. *et al.* Ultrahigh Electron Mobility in Suspended Graphene. *Solid State Communications* **146,** 351-355. issn : 0038-1098 (juin 2008).
191. Larisika, M. *et al.* Electronic Olfactory Sensor Based on A. Mellifera Odorant-Binding Protein 14 on a Reduced Graphene Oxide Field-Effect Transistor. *Angewandte Chemie International Edition* **54,** 13245-13248. issn : 1521-3773 (2015).

192. Moon, J. S. *et al.* Ultra-Low Resistance Ohmic Contacts in Graphene Field Effect Transistors. *Applied Physics Letters* **100,** 203512. issn : 0003-6951 (mai 2012).
193. Vandecasteele, N., Barreiro, A., Lazzeri, M., Bachtold, A. & Mauri, F. Current-Voltage Characteristics of Graphene Devices : Interplay between Zener-Klein Tunneling and Defects. *Physical Review B* **82,** 045416 (juill. 2010).
194. Cohen-Karni, T., Qing, Q., Li, Q., Fang, Y. & Lieber, C. M. Graphene and Nanowire Transistors for Cellular Interfaces and Electrical Recording. *Nano Letters* **10,** 1098-1102. issn : 1530-6984 (mars 2010).
195. Lei, Y.-M. *et al.* Detection of Heart Failure-Related Biomarker in Whole Blood with Graphene Field Effect Transistor Biosensor. *Biosensors and Bioelectronics* **91,** 1-7. issn : 0956-5663 (mai 2017).
196. Fries, R. C. *Reliable Design of Medical Devices* isbn : 978-0-429-11106-8 (CRC Press, avr. 2016).
197. Stern, E. *et al.* Importance of the Debye Screening Length on Nanowire Field Effect Transistor Sensors. *Nano Letters* **7,** 3405-3409. issn : 1530-6984 (nov. 2007).
198. Green, N. S. & Norton, M. L. Interactions of DNA with Graphene and Sensing Applications of Graphene Field-Effect Transistor Devices : A Review. *Analytica Chimica Acta* **853,** 127-142. issn : 0003-2670 (jan. 2015).
199. Sorgenfrei, S., Chiu, C.-y., Johnston, M., Nuckolls, C. & Shepard, K. L. Debye Screening in Single-Molecule Carbon Nanotube Field-Effect Sensors. *Nano Letters* **11,** 3739-3743. issn : 1530-6984 (sept. 2011).
200. Zhang, G.-J. *et al.* DNA Sensing by Silicon Nanowire : Charge Layer Distance Dependence. *Nano Letters* **8,** 1066-1070. issn : 1530-6984 (avr. 2008).
201. Vacic, A. *et al.* Determination of Molecular Configuration by Debye Length Modulation. *Journal of the American Chemical Society* **133,** 13886-13889. issn : 0002-7863 (sept. 2011).
202. Kergoat, L. *et al.* DNA Detection with a Water-Gated Organic Field-Effect Transistor. *Organic Electronics* **13,** 1-6. issn : 1566-1199 (jan. 2012).
203. Matsumoto, K., Maehashi, K., Ohno, Y. & Inoue, K. Recent Advances in Functional Graphene Biosensors. *Journal of Physics D : Applied Physics* **47,** 094005. issn : 0022-3727 (fév. 2014).
204. Ohno, Y., Maehashi, K. & Matsumoto, K. Label-Free Biosensors Based on Aptamer-Modified Graphene Field-Effect Transistors. *Journal of the American Chemical Society* **132,** 18012-18013. issn : 0002-7863 (déc. 2010).
205. Kwon, O. S. *et al.* Flexible FET-Type VEGF Aptasensor Based on Nitrogen-Doped Graphene Converted from Conducting Polymer. *ACS Nano* **6,** 1486-1493. issn : 1936-0851 (fév. 2012).

206. Gao, N. *et al.* General Strategy for Biodetection in High Ionic Strength Solutions Using Transistor-Based Nanoelectronic Sensors. *Nano Letters* **15,** 2143-2148. issn : 1530-6984 (mars 2015).
207. Palazzo, G. *et al.* Detection Beyond Debye's Length with an Electrolyte-Gated Organic Field-Effect Transistor. *Advanced Materials* **27,** 911-916. issn : 1521-4095 (2015).
208. Ingle, J. D. Sensitivity and Limit of Detection in Quantitative Spectrometric Methods. *Journal of Chemical Education* **51,** 100. issn : 0021-9584 (fév. 1974).
209. Balandin, A. A. Low-Frequency 1/ f Noise in Graphene Devices. *Nature Nanotechnology* **8,** 549-555. issn : 1748-3395 (août 2013).
210. Hao, Z. *et al.* Real-Time Monitoring of Insulin Using a Graphene Field-Effect Transistor Aptameric Nanosensor. *ACS Applied Materials & Interfaces* **9,** 27504-27511. issn : 1944-8244 (août 2017).
211. Andoy, N. M., Filipiak, M. S., Vetter, D., Gutiérrez-Sanz, Ó. & Tarasov, A. Graphene-Based Electronic Immunosensor with Femtomolar Detection Limit in Whole Serum. *Advanced Materials Technologies* **3,** 1800186. issn : 2365-709X (2018).
212. Currie, L. A. Nomenclature in Evaluation of Analytical Methods Including Detection and Quantification Capabilities (IUPAC Recommendations 1995). *Pure and Applied Chemistry* **67,** 1699-1723. issn : 1365-3075 (1995).
213. Armbruster, D. A. & Pry, T. Limit of Blank, Limit of Detection and Limit of Quantitation. *The Clinical Biochemist Reviews* **29,** S49-S52. issn : 0159-8090 (août 2008).
214. Yu, F., Yao, D. & Knoll, W. Oligonucleotide Hybridization Studied by a Surface Plasmon Diffraction Sensor (SPDS). *Nucleic Acids Research* **32,** e75-e75. issn : 0305-1048 (mai 2004).
215. Ohno, Y., Maehashi, K., Yamashiro, Y. & Matsumoto, K. Electrolyte-Gated Graphene Field-Effect Transistors for Detecting pH and Protein Adsorption. *Nano Letters* **9,** 3318-3322. issn : 1530-6984 (sept. 2009).
216. Hasegawa, M., Hirayama, Y., Ohno, Y., Maehashi, K. & Matsumoto, K. Characterization of Reduced Graphene Oxide Field-Effect Transistor and Its Application to Biosensor. *Japanese Journal of Applied Physics* **53,** 05FD05. issn : 1347-4065 (avr. 2014).
217. Pembroke, E. *et al.* Effect of Anchor and Functional Groups in Functionalized Graphene Devices. *Nano Research* **6,** 138-148. issn : 1998-0124, 1998-0000 (fév. 2013).
218. Mao, S. *et al.* Ultrasensitive Detection of Orthophosphate Ions with Reduced Graphene Oxide/Ferritin Field-Effect Transistor Sensors. *Environmental Science : Nano* **4,** 856-863 (2017).
219. Lerner, M. B., Dailey, J., Goldsmith, B. R., Brisson, D. & Charlie Johnson, A. T. Detecting Lyme Disease Using Antibody-Functionalized Single-Walled Carbon

Nanotube Transistors. *Biosensors and Bioelectronics* **45,** 163-167. ISSN : 0956-5663 (juill. 2013).

220. Bhatt, K., Kumar, S. & Tripathi, C. C. High-Performance Ultra-Low Leakage Current Graphene-Based Screen-Printed Field-Effect Transistor on Paper Substrate. *Pramana* **94,** 31. ISSN : 0973-7111 (jan. 2020).
221. Blake, P. *et al.* Making Graphene Visible. *Applied Physics Letters* **91,** 063124. ISSN : 0003-6951 (août 2007).
222. Nouchi, R. & Tanigaki, K. Charge-Density Depinning at Metal Contacts of Graphene Field-Effect Transistors. *Applied Physics Letters* **96,** 253503. ISSN : 0003-6951 (juin 2010).
223. Choubak, S. *et al.* Graphene CVD : Interplay Between Growth and Etching on Morphology and Stacking by Hydrogen and Oxidizing Impurities. *The Journal of Physical Chemistry C* **118,** 21532-21540. ISSN : 1932-7447 (sept. 2014).
224. Li, X. *et al.* Transfer of Large-Area Graphene Films for High-Performance Transparent Conductive Electrodes. *Nano Letters* **9,** 4359-4363. ISSN : 1530-6984 (déc. 2009).
225. Lee, J. E., Ahn, G., Shim, J., Lee, Y. S. & Ryu, S. Optical Separation of Mechanical Strain from Charge Doping in Graphene. *Nature Communications* **3,** 1024. ISSN : 2041-1723 (août 2012).
226. Bissett, M. A., Tsuji, M. & Ago, H. Mechanical Strain of Chemically Functionalized Chemical Vapor Deposition Grown Graphene. *The Journal of Physical Chemistry C* **117,** 3152-3159. ISSN : 1932-7447 (fév. 2013).
227. Singh, Y. Electrical Resistivity Measurements : A Review. *International Journal of Modern Physics : Conference Series* **22,** 745-756 (jan. 2013).
228. Cusati, T. *et al.* Electrical Properties of Graphene-Metal Contacts. *Scientific Reports* **7,** 5109. ISSN : 2045-2322 (juill. 2017).
229. Russo, S., Craciun, M. F., Yamamoto, M., Morpurgo, A. F. & Tarucha, S. Contact Resistance in Graphene-Based Devices. *Physica E : Low-dimensional Systems and Nanostructures. 18th International Conference on Electron Properties of Two-Dimensional Systems* **42,** 677-679. ISSN : 1386-9477 (fév. 2010).
230. Levesque, P. L. *et al.* Probing Charge Transfer at Surfaces Using Graphene Transistors. *Nano Letters* **11,** 132-137. ISSN : 1530-6984 (jan. 2011).
231. Lee, Y. G. *et al.* Quantitative Analysis of Hysteretic Reactions at the Interface of Graphene and SiO2 Using the Short Pulse I–V Method. *Carbon* **60,** 453-460. ISSN : 0008-6223 (août 2013).
232. Winters, M., Sveinbjörnsson, E. Ö. & Rorsman, N. Hysteresis Modeling in Graphene Field Effect Transistors. *Journal of Applied Physics* **117,** 074501. ISSN : 0021-8979 (fév. 2015).

233. Ji Kim, Y. *et al.* A Facile Process to Achieve Hysteresis-Free and Fully Stabilized Graphene Field-Effect Transistors. *Nanoscale* **7,** 4013-4019 (2015).
234. Žoldák, G., Stigler, J., Pelz, B., Li, H. & Rief, M. Ultrafast Folding Kinetics and Cooperativity of Villin Headpiece in Single-Molecule Force Spectroscopy. *Proceedings of the National Academy of Sciences* **110,** 18156-18161. issn : 0027-8424, 1091-6490 (nov. 2013).
235. Kubelka, J., Hofrichter, J. & Eaton, W. A. The Protein Folding 'Speed Limit'. *Current Opinion in Structural Biology* **14,** 76-88. issn : 0959-440X (fév. 2004).
236. Wang, Y., Ho, V. X., Henschel, Z. N., Cooney, M. P. & Vinh, N. Q. Effect of High-κ Dielectric Layer on 1/f Noise Behavior in Graphene Field-Effect Transistors. *ACS Applied Nano Materials* **4,** 3647-3653 (avr. 2021).
237. Rumyantsev, S., Liu, G., Stillman, W., Shur, M. & Balandin, A. A. Electrical and Noise Characteristics of Graphene Field-Effect Transistors : Ambient Effects, Noise Sources and Physical Mechanisms. *Journal of Physics : Condensed Matter* **22,** 395302. issn : 0953-8984 (sept. 2010).
238. Marzano, M., Cultrera, A., Ortolano, M. & Callegaro, L. A Correlation Noise Spectrometer for Flicker Noise Measurement in Graphene Samples. *Measurement Science and Technology* **30,** 035102. issn : 0957-0233 (fév. 2019).
239. Kayyalha, M. & Chen, Y. P. Observation of Reduced 1/f Noise in Graphene Field Effect Transistors on Boron Nitride Substrates. *Applied Physics Letters* **107,** 113101. issn : 0003-6951 (sept. 2015).
240. Kidman, D. S. *Science of Test Measurement Accuracy - Data Sampling and Filter Selection during Data Acquisition* rapp. tech. (AIR FORCE TEST CENTER EDWARDS AFB CA, juin 2015). Chap. Technical Reports.
241. Kuila, T. *et al.* Chemical Functionalization of Graphene and Its Applications. *Progress in Materials Science* **57,** 1061-1105. issn : 0079-6425 (sept. 2012).
242. Hirsch, A. Functionalization of Single-Walled Carbon Nanotubes. *Angewandte Chemie International Edition* **41,** 1853-1859. issn : 1521-3773 (2002).
243. Bahr, J. L. *et al.* Functionalization of Carbon Nanotubes by Electrochemical Reduction of Aryl Diazonium Salts : A Bucky Paper Electrode. *Journal of the American Chemical Society* **123,** 6536-6542. issn : 0002-7863 (juill. 2001).
244. Lomeda, J. R., Doyle, C. D., Kosynkin, D. V., Hwang, W.-F. & Tour, J. M. Diazonium Functionalization of Surfactant-Wrapped Chemically Converted Graphene Sheets. *Journal of the American Chemical Society* **130,** 16201-16206. issn : 0002-7863 (déc. 2008).
245. Fang, M., Wang, K., Lu, H., Yang, Y. & Nutt, S. Covalent Polymer Functionalization of Graphene Nanosheets and Mechanical Properties of Composites. *Journal of Materials Chemistry* **19,** 7098-7105. issn : 1364-5501 (sept. 2009).

246. Bekyarova, E. *et al.* Chemical Modification of Epitaxial Graphene : Spontaneous Grafting of Aryl Groups. *Journal of the American Chemical Society* **131,** 1336-1337. issn : 0002-7863, 1520-5126 (fév. 2009).
247. Lim, H., Lee, J. S., Shin, H.-J., Shin, H. S. & Choi, H. C. Spatially Resolved Spontaneous Reactivity of Diazonium Salt on Edge and Basal Plane of Graphene without Surfactant and Its Doping Effect. *Langmuir* **26,** 12278-12284. issn : 0743-7463 (juill. 2010).
248. Wang, Q. H. *et al.* Understanding and Controlling the Substrate Effect on Graphene Electron-Transfer Chemistry via Reactivity Imprint Lithography. *Nature Chemistry* **4,** 724-732. issn : 1755-4349 (sept. 2012).
249. Xia, Y. *et al.* Iodide Mediated Reductive Decomposition of Diazonium Salts : Towards Mild and Efficient Covalent Functionalization of Surface-Supported Graphene. *Nanoscale* **12,** 11916-11926. issn : 2040-3372 (juin 2020).
250. Li, Y. *et al.* Light-Assisted Diazonium Functionalization of Graphene and Spatial Heterogeneities in Reactivity. *The Journal of Physical Chemistry Letters* **10,** 4788-4793 (sept. 2019).
251. Niyogi, S. *et al.* Covalent Chemistry for Graphene Electronics. *The Journal of Physical Chemistry Letters* **2,** 2487-2498 (oct. 2011).
252. Greenwood, J. *et al.* Covalent Modification of Graphene and Graphite Using Diazonium Chemistry : Tunable Grafting and Nanomanipulation. *ACS Nano* **9,** 5520-5535. issn : 1936-0851 (mai 2015).
253. Ambrosio, G. *et al.* Impact of Covalent Functionalization by Diazonium Chemistry on the Electronic Properties of Graphene on SiC. *Nanoscale* **12,** 9032-9037. issn : 2040-3372 (avr. 2020).
254. Rodríguez González, M. C. *et al.* Multicomponent Covalent Chemical Patterning of Graphene. *ACS Nano* **15,** 10618-10627. issn : 1936-0851 (juin 2021).
255. Gan, L., Zhang, D. & Guo, X. Electrochemistry : An Efficient Way to Chemically Modify Individual Monolayers of Graphene. *Small* **8,** 1326-1330. issn : 1613-6829 (2012).
256. Chan, C. K. *et al.* Electrochemically Driven Covalent Functionalization of Graphene from Fluorinated Aryl Iodonium Salts. *The Journal of Physical Chemistry C* **117,** 12038-12044. issn : 1932-7447 (juin 2013).
257. Mishyn, V. *et al.* Controlled Covalent Functionalization of a Graphene-Channel of a Field Effect Transistor as an Ideal Platform for (Bio)Sensing Applications. *Nanoscale Horizons* **6,** 819-829. issn : 2055-6764 (sept. 2021).
258. Brown, A. *et al.* A Chemisorbed Interfacial Layer for Seeding Atomic Layer Deposition on Graphite. *Nanoscale* **13,** 12327-12341. issn : 2040-3372 (juill. 2021).

259. Xia, Z. *et al.* Electrochemical Functionalization of Graphene at the Nanoscale with Self-Assembling Diazonium Salts. *ACS Nano* **10,** 7125-7134. ISSN : 1936-0851 (juill. 2016).
260. Kirkman, P. M., Güell, A. G., Cuharuc, A. S. & Unwin, P. R. Spatial and Temporal Control of the Diazonium Modification of Sp2 Carbon Surfaces. *Journal of the American Chemical Society* **136,** 36-39. ISSN : 0002-7863 (jan. 2014).
261. Farmer, D. B. *et al.* Chemical Doping and Electron-Hole Conduction Asymmetry in Graphene Devices. *Nano Letters* **9,** 388-392. ISSN : 1530-6984, 1530-6992 (jan. 2009).
262. Jacobsen, A., Koehler, F. M., Stark, W. J. & Ensslin, K. Towards Electron Transport Measurements in Chemically Modified Graphene : Effect of a Solvent. *New Journal of Physics* **12,** 125007. ISSN : 1367-2630 (déc. 2010).
263. Koehler, F. M., Jacobsen, A., Ensslin, K., Stampfer, C. & Stark, W. J. Selective Chemical Modification of Graphene Surfaces : Distinction Between Single- and Bilayer Graphene. *Small* **6,** 1125-1130. ISSN : 1613-6829 (2010).
264. Sinitskii, A. *et al.* Kinetics of Diazonium Functionalization of Chemically Converted Graphene Nanoribbons. *ACS Nano* **4,** 1949-1954. ISSN : 1936-0851, 1936-086X (avr. 2010).
265. Dong, X. *et al.* The Electrical Properties of Graphene Modified by Bromophenyl Groups Derived from a Diazonium Compound. *Carbon* **50,** 1517-1522. ISSN : 00086223 (avr. 2012).
266. Solís-Fernández, P., Bissett, M. A., Tsuji, M. & Ago, H. Tunable Doping of Graphene Nanoribbon Arrays by Chemical Functionalization. *Nanoscale* **7,** 3572-3580. ISSN : 2040-3364, 2040-3372 (2015).
267. Fu, W., Jiang, L., van Geest, E. P., Lima, L. M. C. & Schneider, G. F. Sensing at the Surface of Graphene Field-Effect Transistors. *Advanced Materials* **29,** 1603610. ISSN : 09359648 (fév. 2017).
268. Bouilly, D., Janssen, J. L., Cabana, J., Côté, M. & Martel, R. Graft-Induced Midgap States in Functionalized Carbon Nanotubes. *ACS Nano* **9,** 2626-2634. ISSN : 1936-0851 (mars 2015).
269. Wilson, H. *et al.* Electrical Monitoring of Sp ^{3} Defect Formation in Individual Carbon Nanotubes. *The Journal of Physical Chemistry C* **120,** 1971-1976. ISSN : 1932-7447, 1932-7455 (jan. 2016).
270. Bouilly, D. *et al.* Single-Molecule Reaction Chemistry in Patterned Nanowells. *Nano Letters* **16,** 4679-4685. ISSN : 1530-6984 (juill. 2016).
271. Vernick, S. *et al.* Electrostatic Melting in a Single-Molecule Field-Effect Transistor with Applications in Genomic Identification. *Nature Communications* **8,** 15450. ISSN : 2041-1723 (mai 2017).

272. Lee, Y. *et al.* Electrically Controllable Single-Point Covalent Functionalization of Spin-Cast Carbon-Nanotube Field-Effect Transistor Arrays. *ACS Nano* **12,** 9922-9930. issn : 1936-0851 (oct. 2018).
273. Joshi, P., Romero, H. E., Neal, A. T., Toutam, V. K. & Tadigadapa, S. A. Intrinsic Doping and Gate Hysteresis in Graphene Field Effect Devices Fabricated on SiO2substrates. **22,** 334214. issn : 0953-8984 (août 2010).
274. Lafkioti, M. *et al.* Graphene on a Hydrophobic Substrate : Doping Reduction and Hysteresis Suppression under Ambient Conditions. *Nano Letters* **10,** 1149-1153. issn : 1530-6984 (avr. 2010).
275. Delamar, M., Hitmi, R., Pinson, J. & Saveant, J. M. Covalent Modification of Carbon Surfaces by Grafting of Functionalized Aryl Radicals Produced from Electrochemical Reduction of Diazonium Salts. *Journal of the American Chemical Society* **114,** 5883-5884. issn : 0002-7863 (juill. 1992).
276. Niyogi, S. *et al.* Chemistry of Single-Walled Carbon Nanotubes. *Accounts of Chemical Research* **35,** 1105-1113. issn : 0001-4842 (déc. 2002).
277. Sharma, R., Baik, J. H., Perera, C. J. & Strano, M. S. Anomalously Large Reactivity of Single Graphene Layers and Edges toward Electron Transfer Chemistries. *Nano Letters* **10,** 398-405. issn : 1530-6984 (fév. 2010).
278. Goniszewski, S. *et al.* Correlation of P-Doping in CVD Graphene with Substrate Surface Charges. *Scientific Reports* **6,** 22858. issn : 2045-2322 (mars 2016).
279. Fan, X., Nouchi, R. & Tanigaki, K. Effect of Charge Puddles and Ripples on the Chemical Reactivity of Single Layer Graphene Supported by SiO2/Si Substrate. *The Journal of Physical Chemistry C* **115,** 12960-12964. issn : 1932-7447 (juill. 2011).
280. Shih, C.-J. *et al.* Disorder Imposed Limits of Mono- and Bilayer Graphene Electronic Modification Using Covalent Chemistry. *Nano Letters* **13,** 809-817. issn : 1530-6984, 1530-6992 (fév. 2013).
281. Liu, D., He, M., Huang, C., Sun, X. & Gao, B. Fermi-Level Dependence of the Chemical Functionalization of Graphene with Benzoyl Peroxide. *The Journal of Physical Chemistry C* **121,** 10546-10551. issn : 1932-7447 (mai 2017).
282. Ferrari, A. C. & Basko, D. M. Raman Spectroscopy as a Versatile Tool for Studying the Properties of Graphene. *Nature Nanotechnology* **8,** 235-246. issn : 1748-3395 (avr. 2013).
283. Beams, R., Cançado, L. G. & Novotny, L. Raman Characterization of Defects and Dopants in Graphene. *Journal of Physics : Condensed Matter* **27,** 083002. issn : 0953-8984 (jan. 2015).
284. Ott, A. *et al.* Tunable D Peak in Gated Graphene. *Nano Research* **7,** 338-344. issn : 1998-0000 (mars 2014).

285. Eckmann, A. *et al.* Probing the Nature of Defects in Graphene by Raman Spectroscopy. *Nano Letters* **12,** 3925-3930. issn : 1530-6984 (août 2012).
286. Hao, Z. *et al.* Modulating the Linker Immobilization Density on Aptameric Graphene Field Effect Transistors Using an Electric Field. *ACS Sensors* **5,** 2503-2513 (août 2020).
287. Liou, F. *et al.* Imaging Reconfigurable Molecular Concentration on a Graphene Field-Effect Transistor. *Nano Letters.* issn : 1530-6984 (oct. 2021).
288. Bao, L., Kohring, M., Weber, H. B., Hauke, F. & Hirsch, A. Covalently Doped Graphene Superlattices : Spatially Resolved Supratopic- and Janus-Binding. *Journal of the American Chemical Society* **142,** 16016-16022. issn : 0002-7863 (sept. 2020).
289. Nouchi, R., Matsumoto, M. & Mitoma, N. Gate-Controlled Photo-Oxidation of Graphene for Electronic Structure Modification. *Journal of Materials Chemistry C* **7,** 1904-1912. issn : 2050-7534 (fév. 2019).
290. Chiodi, E., Marn, A. M., Geib, M. T. & Ünlü, M. S. The Role of Surface Chemistry in the Efficacy of Protein and DNA Microarrays for Label-Free Detection : An Overview. *Polymers* **13,** 1026 (jan. 2021).
291. Kamada, M. *et al.* Electrical Low-Frequency 1/Fγ Noise Due to Surface Diffusion of Scatterers on an Ultra-low-Noise Graphene Platform. *Nano Letters* **21,** 7637-7643. issn : 1530-6984 (sept. 2021).
292. Song, B. *et al.* Atomic-Scale Electron-Beam Sculpting of Near-Defect-Free Graphene Nanostructures. *Nano Letters* **11,** 2247-2250. issn : 1530-6984 (juin 2011).
293. Heerema, S. J. & Dekker, C. Graphene Nanodevices for DNA Sequencing. *Nature Nanotechnology* **11,** 127-136. issn : 1748-3395 (fév. 2016).
294. McNab, H. & C. Monahan, L. 3-Hydroxypyrroles and 1 H -Pyrrol-3(2 H)-Ones. Part 8. Reactions of 1-Isopropyl-2,2-Dimethyl-1 H -Pyrrol-3(2 H)-One with Electrophiles. *Journal of the Chemical Society, Perkin Transactions 1* **0,** 419-424 (1989).
295. Bazan, C. M. *et al.* (Nano 2nd Place Best Poster Winner) Fabrication of Nanocarbon-Based Field-Effect Transistor Biosensors for Electronic Detection of DNA Sequences. *ECS Transactions* **85,** 499. issn : 1938-5862 (juin 2018).
296. Liang, X. *et al.* Toward Clean and Crackless Transfer of Graphene. *ACS Nano* **5,** 9144-9153. issn : 1936-0851 (nov. 2011).
297. Gaufrès, E. *et al.* Hyperspectral Raman Imaging Using Bragg Tunable Filters of Graphene and Other Low-Dimensional Materials. *Journal of Raman Spectroscopy* **49,** 174-182. issn : 1097-4555 (2018).
298. Feng, T., Xie, D., Wang, D., Wen, L. & Wu, M. Electron-Doping of Graphene-Based Devices by Hydrazine. *Journal of Applied Physics* **116,** 224511. issn : 0021-8979 (déc. 2014).

299. Park, S. *et al.* Chemical Structures of Hydrazine-Treated Graphene Oxide and Generation of Aromatic Nitrogen Doping. *Nature Communications* **3,** 638. issn : 2041-1723 (jan. 2012).
300. Shih, C.-J. *et al.* Disorder Imposed Limits of Mono- and Bilayer Graphene Electronic Modification Using Covalent Chemistry. *Nano Letters* **13,** 809-817. issn : 1530-6984 (fév. 2013).
301. Giovannetti, G. *et al.* Doping Graphene with Metal Contacts. *Physical Review Letters* **101,** 026803 (juill. 2008).

Annexe A

Information complémentaire de l'article *Graphene Field-Effect Transistors as Bioanalytical Sensors : Design, Operation and Performance*

A.1. Supporting Information

A.1.1. Literature survey

We surveyed the literature for studies on GFETs applied as bioanalytical sensors. Specifically, we selected experimental studies conducted with GFETs to detect biologically-relevant analytes, such as proteins, DNA, small molecules, ions, bacterias, viruses. We collected 85 papers fitting this criteria. For each paper, we extracted a wide range of parameters covering design, operation and performance specifications. We used n/a when the attribute was not applicable, and not found when we could not find the information in the paper. The complete database of these papers is provided online here : `http://bit.ly/Beraud2020_bioGFETdatabase`.

A.1.2. Analysis of reported LODs

The analysis of reported limits of detection (LoDs) was done on papers from the above collection that presented the following two critera :

— Limit of detection (LOD) explicitly stated in the paper ;

— Analyte concentrations expressed in molar unit (M) or conversion possible with the information provided in the paper.

With these constraints, we collected 61 papers providing the following data :

— 20 data points from 17 papers on protein detection (Table S1),

— 14 data points from 12 papers on ions detection (Table S2),

— 10 data points from 10 papers on the detection of various small molecules (Table S3),

— 23 data points from 22 papers on DNA detection (Table S4).

For these four sets, we tabulated below the nature of the analyte, the type of graphene used, and the LOD as it is reported in the paper. In the case of DNA detection, we also report the length of the target DNA sequence. When necessary, we also report the molecular weight of the analyte used to convert the LOD in molar unit. All reference numbers are the same as in the main article.

We draw attention on two considerations :

(1) The LODs were transcribed as reported in the original articles. Consequently, the tabulated data aggregates LODs calculated with various techniques, without validation or calibration of the methods used by the authors of the studies.

(2) Graphene type is presented here as a proxy for graphene quality (as discussed in the main article). Mobility values were not directly used because they were not reported in enough papers, and because reported values often include contributions external to the quality of graphene itself, such as from the contacts.

Graphene type	Analyte	Molecular weight	Reported LOD	LOD in M	Citation
rGO	Protective Antigen		1.2aM	1.2×10^{-18}	[168]
rGO	PSA-ACT		1.1 fM	1.1×10^{-15}	[70]
rGO	BNP		100 fM	1×10^{-13}	[195]
rGO	IgG	150 KDa	1 ng/mL	6.7×10^{-12}	[169]
rGO	IgE		43.2pM	4.3×10^{-11}	[216]
CVD	SARS-CoV-2 spike protein	90kDa	1fg/mL	1.1×10^{-17}	[159]
CVD	TSH		0.2×10^{-15}	2×10^{-16}	[211]
CVD	Ferritin		10fM	1×10^{-14}	[140]
CVD	HcG	36.7 kDa	1 pg/mL	2.7×10^{-14}	[26]
CVD	IL-6		618 fM	6.2×10^{-13}	[162]
CVD	Insulin		766 fM	7.6×10^{-13}	[162]
CVD	AFP	70 kDa	0.1 ng/mL	1.4×10^{-12}	[148]
CVD	Thrombin		2.6pM	2.6×10^{-12}	[90]
CVD	Poly-l-lysine		11 pM	1.1×10^{-11}	[155]
CVD	Insulin		35 pM	3.5×10^{-11}	[210]
CVD	IFN-γ		83 pM	8.3×10^{-11}	[127]
ME	cTn1	23.9 kDa	10 fg/mL	4.2×10^{-16}	[141]
ME	CCP	10 kDa	10 fg/mL	1×10^{-15}	[141]
ME	p24	24 kDa	100 fg/mL	4.2×10^{-15}	[141]
ME	HSP		100 pM	1×10^{-10}	[114]

Tableau A.1 – Reported data in GFET studies on protein detection (20 data points from 17 papers)

Graphene type	Analyte	Molecular weight	Reported LOD	LOD in M	Citation
rGO	Hg^{2+}		1 nM	1×10^{-9}	[142]
rGO	Hg^{2+}		1 nM	1×10^{-9}	[67]
rGO	Pb^{2+}		10 nM	1×10^{-8}	[144]
rGO	HPO_4^{2-}		26 nM	2.6×10^{-8}	[218]
rGO	Ca^{2+}		1 μM	1×10^{-6}	[67]
CVD	K^+		0.058pM	5.8×10^{-14}	[179]
CVD	Hg^{2+}		10 pM	1×10^{-11}	[147]
CVD	Hg^{2+}		40 pM	4×10^{-11}	[146]
CVD	Pb^{2+}	207 g/mol	163.7 ng/L	7.9×10^{-10}	[68]
CVD	K^+		1nM	1×10^{-9}	[143]
CVD	Pb^{2+}		2μM	2×10^{-6}	[180]
CVD	K^+		27μM	2.7×10^{-5}	[180]
ME	Pb^{2+}	207 g/mol	37.5ng/L	1.8×10^{-10}	[145]
ME	Hg^{2+}	200.58 g/mol	0.1ppb	5×10^{-7}	[113]

Tableau A.2 – Reported data in GFET studies on ion detection (14 data points from 12 papers)

Graphene type	Analyte	Molecular weight	Reported LOD	LOD in M	Citation
rGO	Tobramycin		0.3 nM	3×10^{-10}	[78]
rGO	ATP		400nM	4×10^{-7}	[131]
CVD	Biotin		0.37pM	3.7×10^{-13}	[125]
CVD	Nalodextrone	341.401 g/mol	10 pg/mL	2.9×10^{-11}	[77]
CVD	OH radical		10^{-9}M	1×10^{-9}	[80]
CVD	Glucose		0.15 μM	1.5×10^{-7}	[60]
CVD	Glucose		0.46 μM	4.6×10^{-7}	[69]
CVD	Glucose		0.1 mM	1×10^{-4}	[116]
ME	Chlorpyrifos		1.8 fM	1.8×10^{-15}	[84]
ME	NO		0.3 nM	3×10^{-10}	[79]

Tableau A.3 – Reported data in GFET studies on small molecules detection (10 data points from 10 papers)

Graphene type	DNA length (mer)	LOD reported (M)	Citation
rGO	18	5×10^{-12}	[88]
rGO	22	1×10^{-13}	[71]
rGO	22	1×10^{-14}	[183]
rGO	22	2.4×10^{-9}	[132]
rGO	24	2×10^{-9}	[157]
CVD	11	2×10^{-12}	[93]
CVD	12	1×10^{-12}	[129]
CVD	12	1×10^{-11}	[130]
CVD	15	1×10^{-13}	[109]
CVD	15	1×10^{-17}	[184]
CVD	19	1×10^{-9}	[133]
CVD	20	1×10^{-11}	[81]
CVD	20	3×10^{-9}	[158]
CVD	20	1×10^{-13}	[91]
CVD	21	5×10^{-15}	[85]
CVD	22	6×10^{-19}	[87]
CVD	22	2×10^{-17}	[87]
CVD	22	1×10^{-14}	[150]
CVD	25	2.5×10^{-17}	[24]
CVD	30	1×10^{-9}	[134]
CVD	39	8×10^{-21}	[149]
CVD	60	1×10^{-15}	[25]
CVD	80	1×10^{-18}	[86]

Tableau A.4 – Reported data in GFET studies on DNA hybridization detection (23 data points from 22 papers)

Annexe B

Information complémentaire pour l'article *Gate Control of Aryldiazonium Chemistry on Graphene Field-Effect Transistors* (Supporting Information)

B.1. Materials, methods and instrumentation

B.1.1. Aryldiazonium reagents

The 4-carboxybenzenediazonium tetrafluoroborate (CBDT) reagent was synthesized according to established synthesis protocol [294]. The 4-bromobenzenediazonium tetrafluoroborate (BBDT) was purchased from Sigma-Aldrich (no 280895). CBDT or BBDT solutions were prepared at the moment of use.

B.1.2. Graphene synthesis

Graphene was grown by low pressure chemical vapor deposition (CVD) using 25 μm-thick copper as the catalyst for methane decomposition, following a method adapted from [223]. Devices were made using either this graphene or CVD graphene purchased from Graphenea (product number : F24993). No significant differences were observed in either device properties or functionalization response between the two types of graphene. All surface doping experiments were performed on graphene surfaces synthesized as described above.

B.1.3. Fabrication of GFET devices

GFET devices were fabricated on a doped silicon substrate covered with an oxide layer (Si doped n^{++}/SiO_2 285 nm), following a design inspired from previous work [295]. Source-drain electrode pairs (5 nm Ti/25 nm Au) with a 4 μm separation were first patterned on the substrate using photolithography techniques and e-beam metal evaporation. When relevant, a coplanar gate

electrode (10 nm Ti/40 nm Pt) was added using the same methods. In some chips, the surface was treated with hexamethyldisilazane (HMDS) vapor at 120°C for 90 seconds before graphene transfer to promote graphene adhesion - no effect was noted on device performance. Graphene films were transferred using a wet etching technique in 0.1 M ammonium persulphate ($(NH_4)_2S_2O_8$, Across Organics, +98%) aqueous solution [224, 296]. Finally, graphene ribbons of 6 μm-wide x 39 μm-long were patterned using a combination of photolithography and oxygen plasma techniques.

B.1.4. Spontaneous functionalization of GFETs

Before functionalization, the chips contacts were passivated with photoresist (resin OIR 674-11, Fujifilm) and photolithography was used to expose the graphene ribbon areas in micron-scale chambers of 17 μm wide x 170 μm long. As a control, passivated chips were first immersed in saline buffer solution (in 100 mM phosphate buffer, PB, pH=8.0) for 24h at room temperature. After incubation, the devices were washed with 20 mL of Milli-Q water (drop by drop) and quickly dried with nitrogen to be able to mount a top open Polydimethylsiloxane (PDMS) cell, fabricated using 3D printing and soft lithography techniques. Once assembled, the PDMS cell was filled with PB to proceed to electrical characterization. For the experiment, the same chips were dismounted and then immersed in 10 mM CBDT solution in PB, incubated for 24h at room temperature, and washed with Milli-Q water as described earlier before their electrical characterization in PB. For both electrical measurements, a pseudo-reference electrode (Pt-Ir 70 :30 alloy) was immersed in PB in the PDMS cell and used as gate electrode. Transfer curves were acquired at $V_{DS} = 50$ mV in a Cascade Summit ambient probe station linked to a Keysight B1500A Parameter Analyzer.

B.1.5. Surface doping and functionalization

Spontaneous functionalization on Si/SiO_2. Graphene transferred on an Si/SiO_2 substrate was incubated for one hour in 1mM of of BBDT in acetonitrile (ACN) purged in nitrogen. It was then rinsed in acetonitrile for 5 minutes and in isopropanol for 5 minutes.

Functionalization of hydrazine-doped graphene. Graphene on Si/SiO_2 samples were immersed for 10 min in a hydrazine solution, with concentrations ranging from 1 mM to 10 mM, then immediately dried with N_2. The same samples were then immersed in the 1 mM BBDT solution for 30 min.

Electrochemical functionalization. Graphene was transferred on an Si/SiO_2 substrate and a small Pd/Ti (30 nm/2 nm) contact was deposited by e-beam evaporation to apply the working potential. A twisted Pt wire was used as a counter electrode and an Ag/AgCl electrode as reference. Potential was swept from 0 V to -0.5 V at a rate of 50 mV/s for five cycles with an Epsilon potentiostat. For functionalization, 0.1 M tetrabutylammonium hexafluorophosphate (TBAF, Sigma-Aldrich no 86879) was added to the 1 mM BBDT solution as an electrolyte. After electrografting was complete, the sample was rinsed in acetonitrile for 5 minutes and in isopropanol for 5 minutes.

Functionalization on copper. Immediately after CVD growth, the graphene still on copper was immersed in the 1mM of BBDT solution, then rinsed in acetonitrile for 5 minutes and in isopropanol

for 5 minutes. Afterwards, the sample was transferred onto Si/SiO_2 substrate using wet transfer, and Raman and XPS characterization were conducted.

B.1.6. Raman spectroscopy

On GFET devices. Raman images of GFETs were recorded at a wavelength of $\lambda = 532$ nm (2.33 eV) with a hyperspectral global imaging instrument (RIMA, Photon Etc. [297]) using a 100X objective giving a laser spot size of about 200μm, a laser power of 45 µW.μm^{-2} and an acquisition time of 15 s per pixel.

On graphene surfaces. Raman spectra were collected with a RM3000 Renishaw Raman Spectroscopy system coupled with a 514 nm Ar^+ ion laser with a 25 mW power. A 50X lens with a 0.55 numerical aperture was used in parallel to a diffraction lattice with a 1800 lines/mm density. The power measured at the lens during data acquisition was 0.16 mW with 30 s exposition time for a single accumulation.

B.1.7. Gate-controlled functionalization of GFETs

Functionalization and electrical measurements were done together in a custom setup designed to combine multiplexed electrical probing and flow control. In this setup, a GFET chip was placed in a custom-machined holder allowing to align a flow cell and electrical probes connecting the S/D electrodes of each GFET as well as the common co-planar gate electrode (Fig. S1, no.1). Here, we used chips with non-passivated electrodes, after testing functionalization experiments on passivated and non-passivated chips. Both of these gave similar results, indicating that there was no perturbation from possible reactions on electrodes in the experimental conditions used. The flow cell was made of PDMS from a 3D-printed mold and comprises a thin enclosed channel aligned to the middle of the chip, thus minimizing sample evaporation, that can be filled/emptied with inlet and outlet tubings. A programmable infusion/withdrawal syringe pump (Kd Scientific, Fig. S1, no.2) was used to control the flow at a rate of 3mL/min. Saline solutions of 100mM phosphate buffer (PB) pH=8.0, with or without 10 mM of CBDT, were used in the flow cell for functionalization or control experiments, respectively. Details of the protocols followed during each experiment are detailed later (see Figs. S9-15-16-18).

To power and measure GFET devices, on-chip pins were routed through a custom printed circuit board (Fig. S1, no.3) to a National Instruments PXI system including a DAQ (PXIe-6358) and an SMU (PXIE-4140) modules (Fig. S1, no.4). Drain-source voltage ($V_{DS} = 50$ mV) was applied by the analog output of the DAQ, and drain-source currents were read by its analog inputs. The gate voltage (variable) was applied by the SMU. Labview codes were implemented to simultaneously record transfer curves and time series for each individual GFET on the chip.

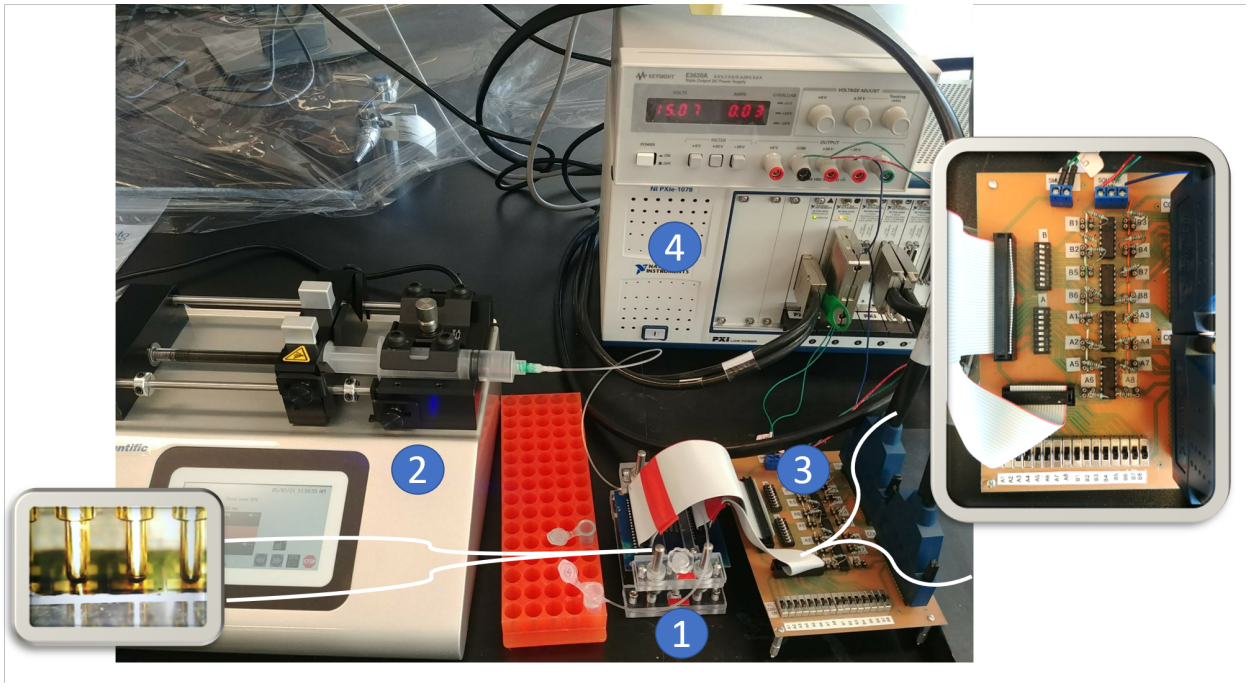

Figure B.1 – Setup design for multiplexed gate-controlled functionalization. 1) Machined chip holder including a flow cell and electrical pin-probes, with a close-up of the pin-probes connecting to on-chip electrodes. 2) Syringe pump connected to the flow cell tubing. 3) Printed circuit board connecting the holder pins to the acquisition system, with a close-up to the right. 4) PXI chassis and modules used for applying source, drain and gate voltages and for reading currents in a multiplexed configuration.

B.2. Backgated vs immersed gate transfer curves

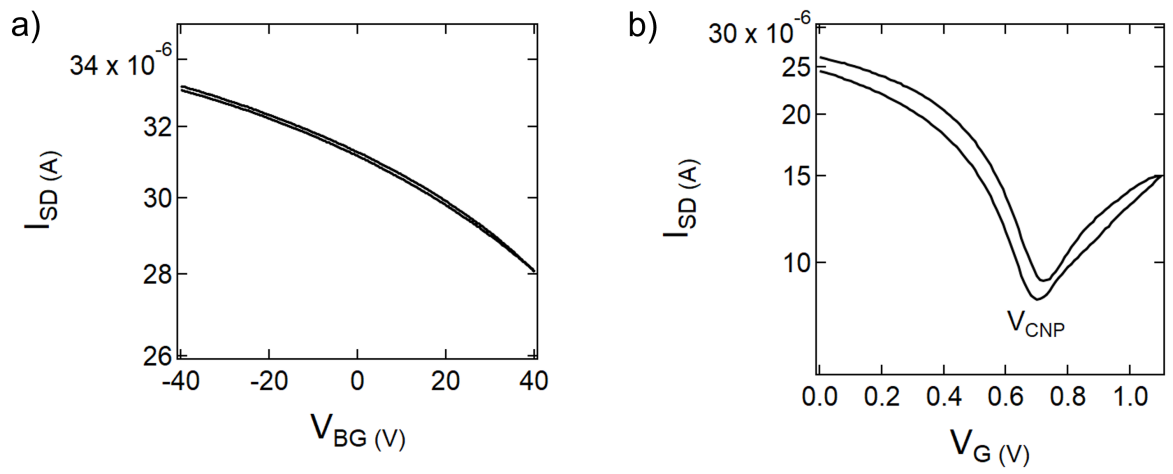

Figure B.2 – Typical transfer curves I_{SD} vs. V_G from the same GFET device before functionalization for back-gate (a) and immersed gate (b) configurations.

Transfer curves were performed to characterize the initial electrical characteristics of the devices. Typical transfer curves are shown in the figure : in (a) the backgate bias was swept from -40V to 40V and in (b) the bias from the immersed gate in saline buffer was swept from 0V to 1.1V. In both cases, the source-drain bias, V_{SD}, was fixed at 0.05V. The transfer curve for the immersed gate shows the typical ambipolar behavior (p- and n-branches) of graphene, with a minimum associated to the charge neutrality point voltage V_{CNP}. Here the V_{CNP} is larger than zero, meaning that the graphene is p-doped. The V_{CNP} is out of the range of the backgated curve. Following displacements of the V_{CNP} in subsequent measurements allows to characterize changes in the doping level of the graphene.

B.3. Example of fitting for I_{CNP} and V_{CNP} extraction

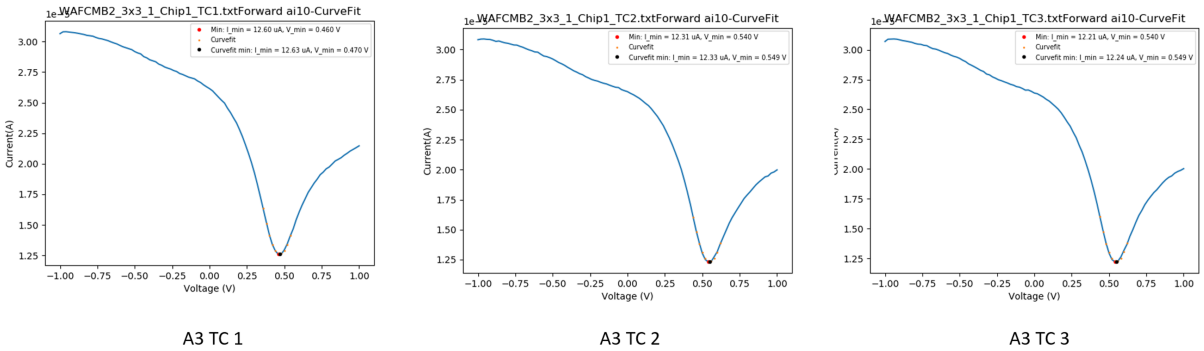

Figure B.3 – Three typical transfer curves taken sequentially before functionalization. Two methods are used to retrieve the I_{CNP} and V_{CNP} (curve minimum and polynomial curve-fitting), which give comparable results.

The values of I_{CNP} and V_{CNP} were extracted by home-made codes. Two methods were compared. The fist one consists of taking the absolute minima of each transfer curve, and extracting the associated voltage. The second method consists of taking a polynomial fit, and then extracting the minima of the fit itself and its associated voltage. Both methods rendered very close results, we chose the curve-fitting method as it allows for a better precision in the V_{CNP} value.

B.4. Initial electrical metrics of GFETs

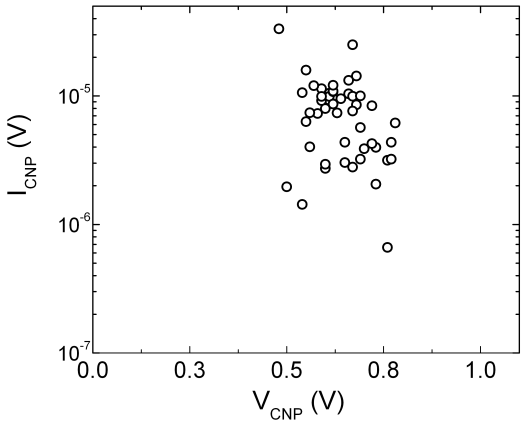

Figure B.4 – Device-to-device variability in initial metrics before functionalization.

Device-to-device variability was determined by the distribution of the current and gate voltages at the charge neutrality point (I_{CNP} and V_{CNP}) obtained from transfer curves in saline buffer solution before the spontaneous functionalization. Values of I_{CNP} and V_{CNP} were obtained using the curve-fitting method described in Fig. S3. All the devices showed comparable initial electrical metrics as seen from the compact distribution. According to the extracted V_{CNP}, the graphene in all GFETs is initially p-doped.

B.5. Effect of 24h incubation in buffer (control)

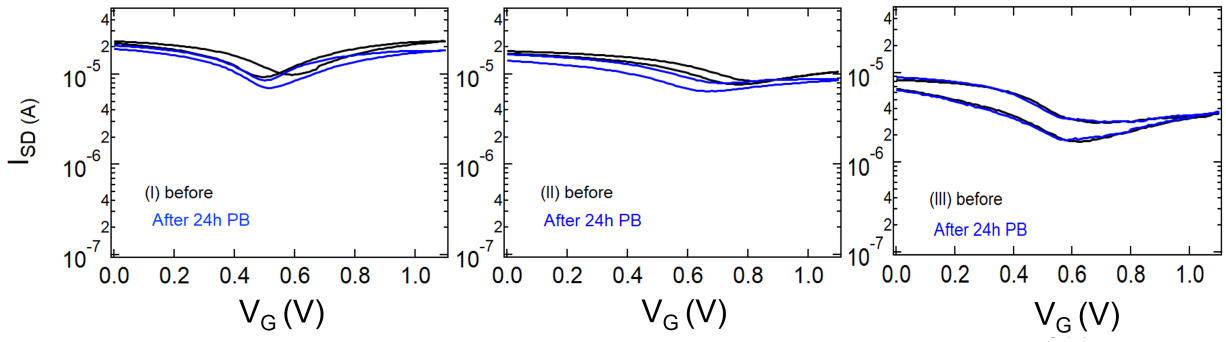

Figure B.5 – Electrical characteristics of control devices before and after 24h incubation in saline buffer.

We performed control experiments by incubating the chips for 24h in saline buffer solution, and compared the electrical characteristics of the devices in transfer curves before and after incubation. Typical transfer curves for control devices before (black line) and after PB incubation (blue line) show that saline buffer does not lead to any significant decrease in conductance (*i.e.* I_{SD}), nor is it modifying significantly the doping level of devices (*i.e.* V_{CNP}).

B.6. Shift of the transfer curves after CBDT

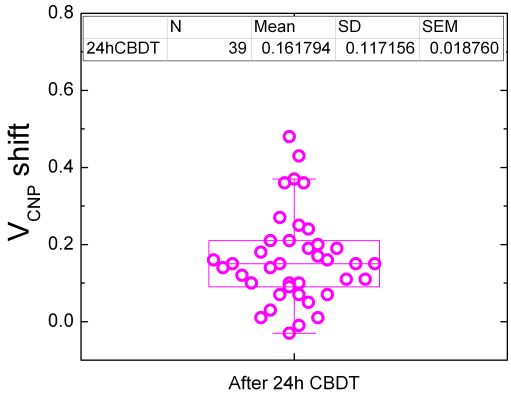

Figure B.6 – V_{CNP} shift after 24h CBDT reaction, with points distributed according to a violin plot algorithm over the boxplot.

After 24h CBDT reaction, the devices typically showed a small positive V_{CNP} shift, of 0.16±0.12V in average, indicating a moderate p-doping of the graphene after CBDT grafting. Note that some devices (N=11/50) did not show a clear V_{CNP} after the reaction, often because the modulation of the transfer curve after functionalization was too much altered ; these devices were not included in this analysis.

B.7. Statistical analysis on spontaneous functionalization

	N total	Mean	Standard	SE of mea	Minimum	Median	Maximum
Control	50	-0.141091	0.4830926	0.0683196	-3.069932	-0.024067	0.2666512

	N total	Mean	Standard	SE of mea	Minimum	Median	Maximum
Experime	50	-0.861701	0.930128	0.131540	-4.242603	-0.501158	0.158362

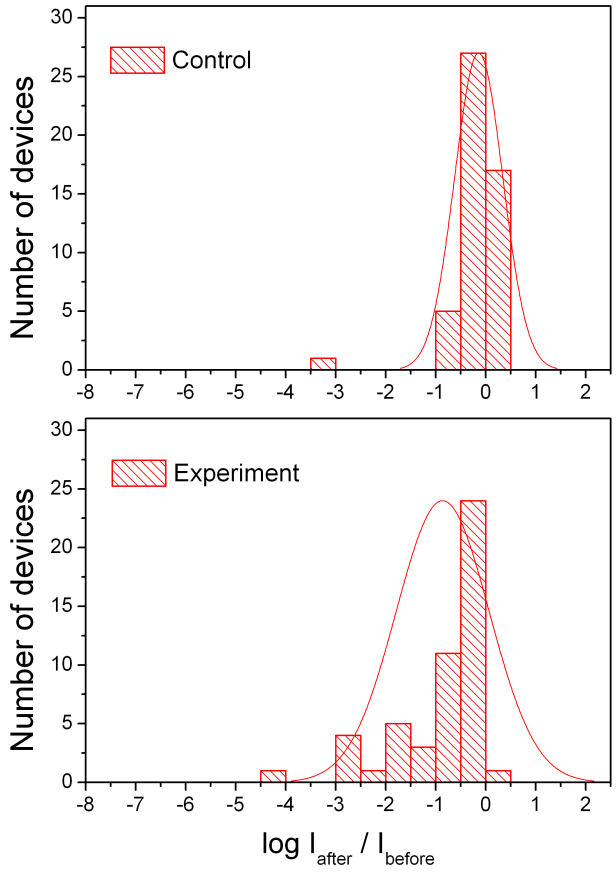

Figure B.7 – Statistical analysis on spontaneous functionalization dataset for control and experiment.

The dataset of Figure 1d is presented here in the form of histograms in log scale, and the resulting distribution is fitted with a normal distributions (corresponding to a log-normal distribution of the data itself). The geometric mean of the conductance change is $10^{(-0.1\pm0.5)}$ for the control and $10^{(-0.9\pm0.9)}$ for the experiment, respectively. In control devices, the distribution is centered around 10^0 since no functionalization is taking place. In functionalized devices (experiment), the distribution extends to lower values, with most of the devices showing a conductance change within one order of magnitude and 28% of the devices showing a larger conductance drop of up to five orders of magnitude.

B.8. Conductance drop vs. initial electrical metrics

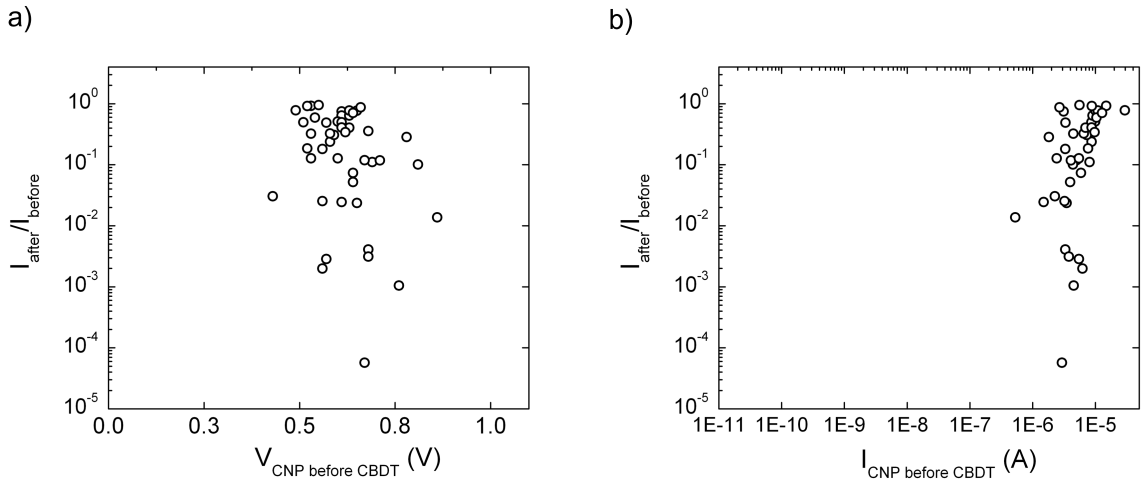

Figure B.8 – Conductance drop after 24h CBDT vs. electrical metrics before functionalization (a) V_{CNP} and (b) I_{CNP}.

We investigated the role of the initial electrical characteristics of graphene in GFETs on its reactivity. We plotted the conductance drop (I_{after}/I_{before}) obtained after spontaneous functionalization in CBDT as a function of the electrical metrics of the devices before functionalization, specifically (a) the initial graphene doping V_{CNP} and (b) the initial I_{CNP} (as a metric of possible defects on the graphene surface). There seems to be no correlation between the conductance drop and the initial electrical metrics. I_{CNP} and V_{CNP} values were obtained using the curve-fitting method described in Fig. S3.

B.9. Experimental protocol for gate-controlled CBDT functionalization on GFETs

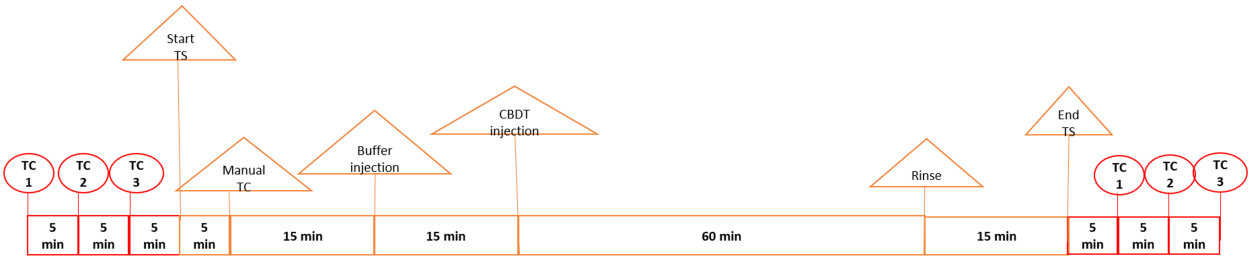

Figure B.9 – Timeline of the experiments for the gate-controlled CBDT functionalization of GFETs with the PXI setup. TC stands for transfer curve, TS stands for time series.

All the experiments in Figures 2 and 4a-b were conducted with the PXI setup (see Fig. S1) following the same protocol. The GFET chip was inserted in the chip holder, and mounted with a PDMS flow cell on top. Saline buffer (PB pH = 8.0) was injected until the flow cell is full. Three transfer curves were collected with a 5 minutes stabilization time in between, going from $V_G = -1$ V to $V_G = 1$ V with $V_{SD} = 0.05$ V. The value of the charge neutrality currents and voltages for the "before functionalization" state were extracted as described in Fig. S3. After another 5 minutes of stabilization, time series were started with the gate voltage at $V_G = 0$ V and $V_{SD} = 0.05$ V, with a sampling rate of 100 points per second. After 5 minutes, a manual transfer curve was conducted, meaning that the gate voltage was gradually increased, or decreased, to the desired value with increments of 0.1 V. This was done to confirm the gating activity of the gate electrode on the source-drain current. Some of the later experiments were conducted without this step, with the initial gate voltage directly at the desired value. In any case, the gate voltage was then left constant until the end of the time series. After waiting for a 15 min settling time, a fixed volume of saline buffer was injected, followed by 15 min wait time. During this time, the CBDT reagent was weighed and the same buffer volume was prepared in order to mix them in a 10 mM CBDT solution, that was then immediately injected in the flow cell, followed by 60 min wait time. After this, the flow cell was purged with 3 mL of buffer, followed by a wait time of 15 minutes, at which point the time series was finally stopped. After 5 minutes settling time, three final transfer curves were collected with 5 minutes in between. The values for I_{CNP} and V_{CNP} for "after functionalization" points were again extracted as shown in Fig. S3.

B.10. Extraction of reaction rates

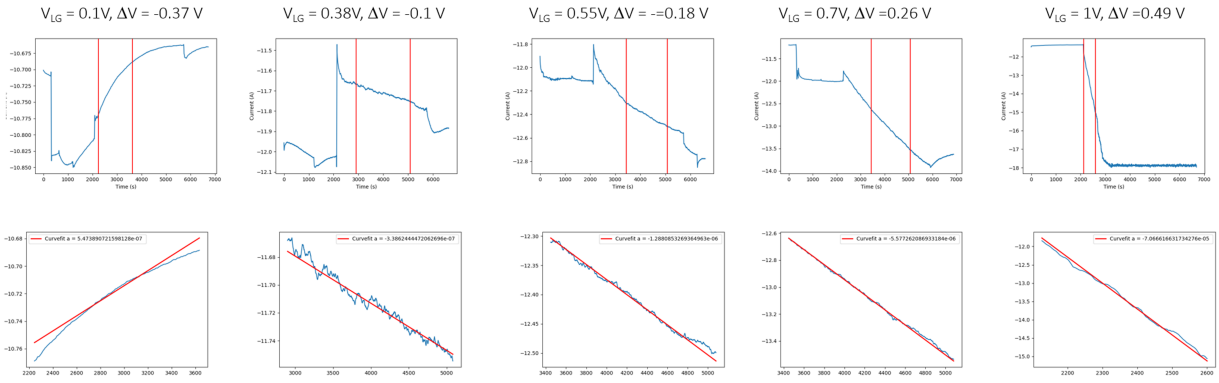

Figure B.10 – Top panels : complete time series for typical devices in experiments conducted at $V_G = 0.1$ V, $V_G = 0.38$ V, $V_G = 0.55$ V, $V_G = 0.7$ V and $V_G = 1$ V. The red lines show the boundaries for the linear fitting. Bottom panels : Parts of the time series between the boundaries and associated linear fits (red line), with values of rates given by the fit.

From Fig. 2b, one can see that the current decreases exponentially with time from the moment of injection of the reagent, such that $I_{SD} \propto \exp[-k(t-t_{inj})]$, or equivalently $\ln I_{SD} \propto -k(t-t_{inj})$. To get a value for the reaction rate k, the time series for all experiments were plotted in a logarithmic scale, and the linear regime was fitted to extract the slope.

Five experiments were run with different gate potentials applied during functionalization with CBDT ($V_G = 0.1$ V, $V_G = 0.38$ V, $V_G = 0.55$ V, $V_G = 0.7$ V and $V_G = 1$ V). Note that since the initial V_{CNP} was not exactly the same between devices, the resulting ΔV_{G-CNP} also varies slightly between devices that were functionalized in the same experiment. The figure shows a typical complete time series for each experiment (top panels), and a close-up of the fitted region with the extracted value of the linear fit (bottom panels). In the complete time series, red vertical lines show the range in which the fitting was applied. Regions at the beginning and the end of the time series were excluded : the former because of instabilities due to the flow of solution during injection, the latter to avoid increased noise levels as low current or occasional perturbations as discussed in Fig. S11 (right panel).

After the injection, a sublinear pattern is sometimes observed before stabilization into a linear behaviour. For simplicity, we focused our fitting on the linear part of the curve. In the case of negative ΔV_{G-CNP}, in which no reaction occurs, the curve is sometimes slightly positive. We note that in the reaction rate plot, the absolute value of the reaction rate was plotted since the data is presented in log scale.

B.11. Anomalies in reaction rates

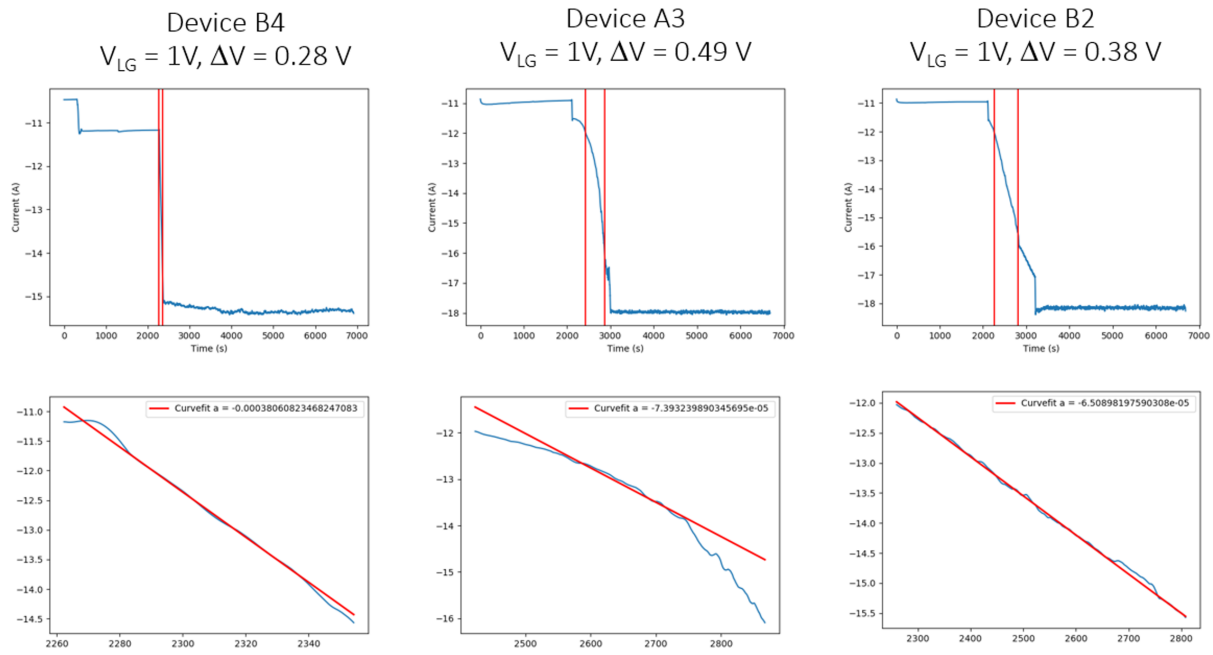

Figure B.11 – Top panels : complete time series for some devices in experiments conducted at $V_G = 1$ V (fastest rate). The red lines show the boundaries for the linear fitting. The first column presents a device with an excessively rapid rate of reaction. The second column presents a device with a supralinear behaviour at the start of the reaction. Third column presents a device with a change of rate at the end of reaction. Bottom panels : Parts of the time series between the boundaries and associated fits (red curve), with values of rates given by the fit.

We underline that at high gate voltage ($V_G = 1$ V), some devices exhibited anomalies in their time series. We present in Fig. **??** some examples. In the panel presenting device B4, we note a very quick drop in current, higher than most others, even though $\Delta V_{G-CNP} = 0.28$ V, which is not the highest value in our dataset. Around five devices presented this behaviour - those represent the highest rates in Fig. 2c. There is a possibility that these could be due to a breakdown of the devices unrelated to the CBDT reaction, or it could be representative of the high variability of response in this range of fast reaction at high gate voltages. In device A3, we note a supralinear behaviour at the beginning of the curve, different from the sublinearity observed at other voltages, and this results in a slightly worse fit quality. Finally, in device B2, we see a change in rate at the end of the reaction. Two different runs of experiments were conducted at $V_G = 1$ V, and all devices from only one of the two experiments show this feature, indicating that it could be related to some external perturbation during the experiment.

B.12. Reaction rates with a linear scale

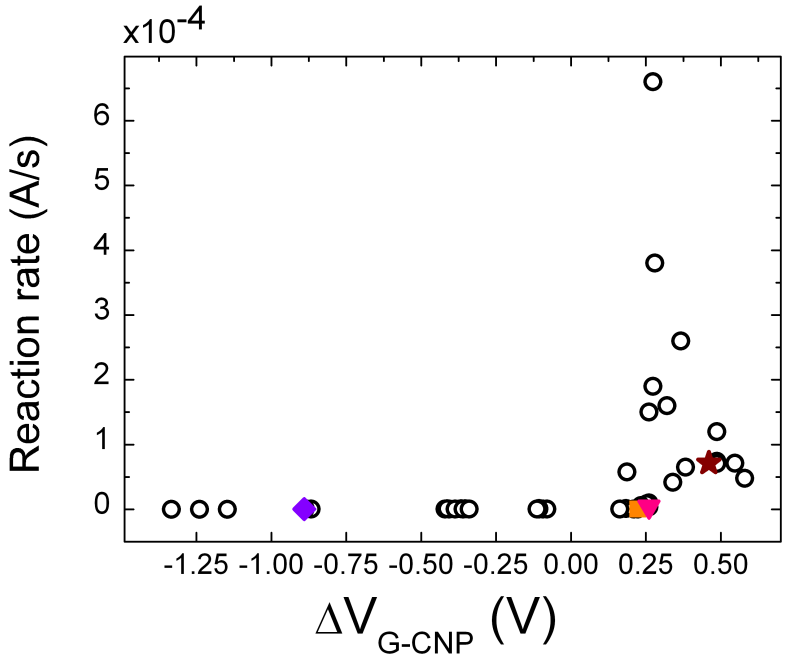

Figure B.12 – Reaction rates in function of ΔV_{G-CNP} presented in a linear scale.

We present all available reaction rate data, extracted with the previously detailed method. The linear scale (opposed to the semilog scale as in Fig. 2c) allows to see that at negative ΔV_{G-CNP} values, the reaction rates are close to zero, oscillating between positive and negative value. This represents the resolution limit or noise range for the reaction rate.

B.13. Reaction times $t_{10\%}$ for 10% decrease in the conductance

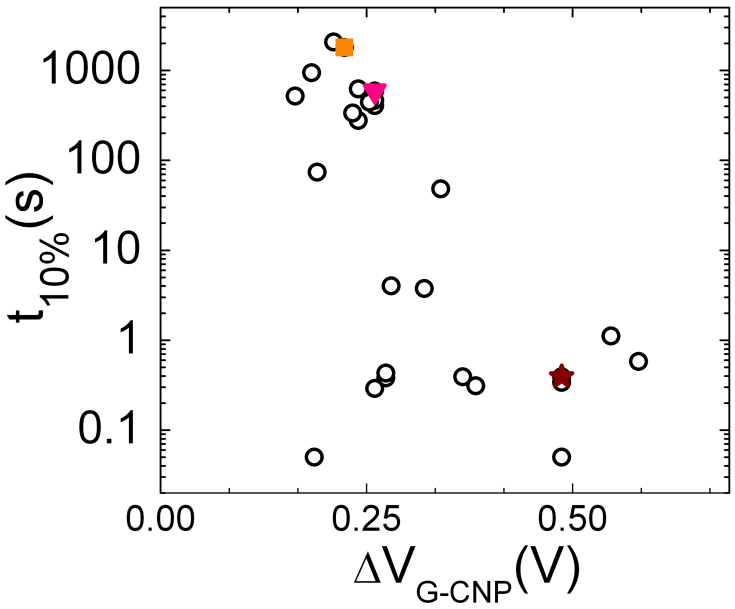

Figure B.13 – Reaction times extracted at 10% of current drop. Colored dots correspond to time series in Fig. 2b.

For each time series collected at positive ΔV_{G-CNP} (see Fig. 2c), the time necessary for the current to drop by 10% of its initial value ($t_{10\%}$) was extracted and is shown here as function of ΔV_{G-CNP}. Details on the approach for the extraction are described in Fig. S14. Values of $t_{10\%}$ are seen to span from tens of minutes to down to less than a second, and show a general decreasing trend with ΔV_{G-CNP}.

B.14. Extraction of $t_{10\%}$ from current time series

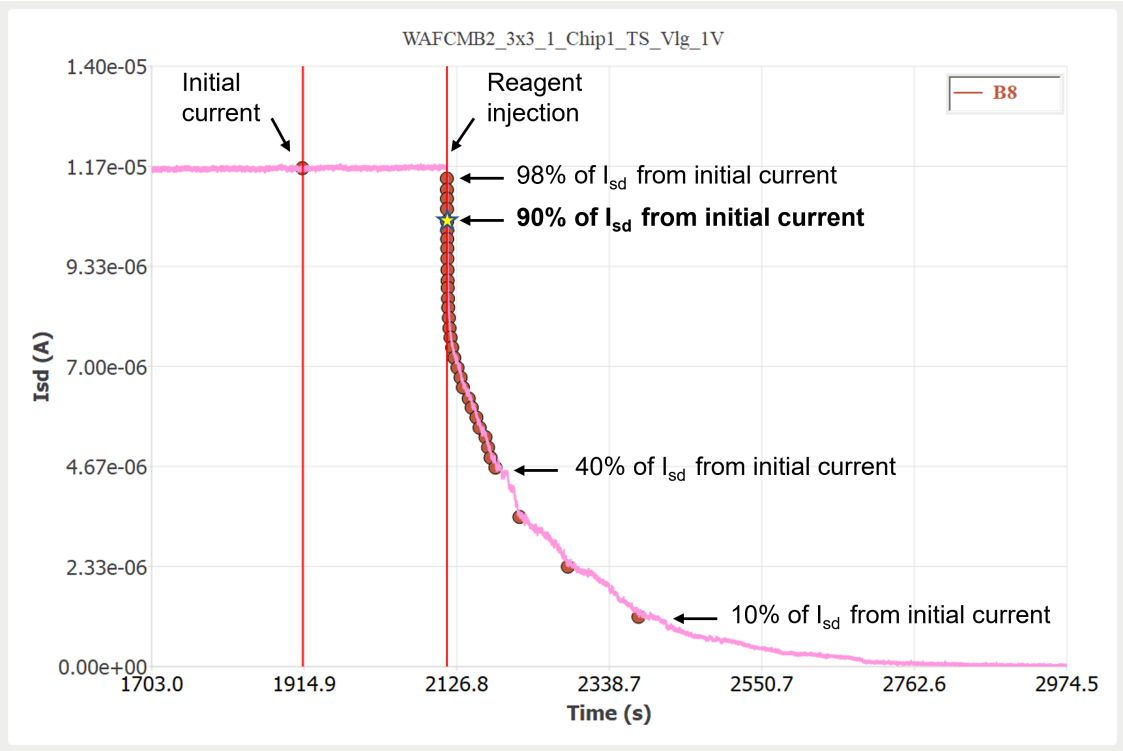

Figure B.14 – Example of a time series for a device functionalized at $V_G = 1$ V, with points placed at the initial current (before reagent injection) and then at current values corresponding to various percentages of decrease from the initial current (every 2% until reaching 40% of the initial current, then every 10%).

In each time series, the time required to reach a certain percentage of conductance drop from the initial value was extracted using a custom code. First, a value for the initial current is calculated from an average of the time series before reagent injection (300 points centered 200 seconds before injection). The code then calculates the current corresponding to every percentage of decrease from the initial current (*i.e.* points in the figure for every 2% decrease until reaching 40% of the initial current, then every 10%), and then extracts the time corresponding to these points in the TS curve. This procedure was done for all time series, and the times corresponding to a 10% decrease (or 90% of the initial current) were compiled in Fig. S13.

B.15. Experimental protocol for gate-switch experiments

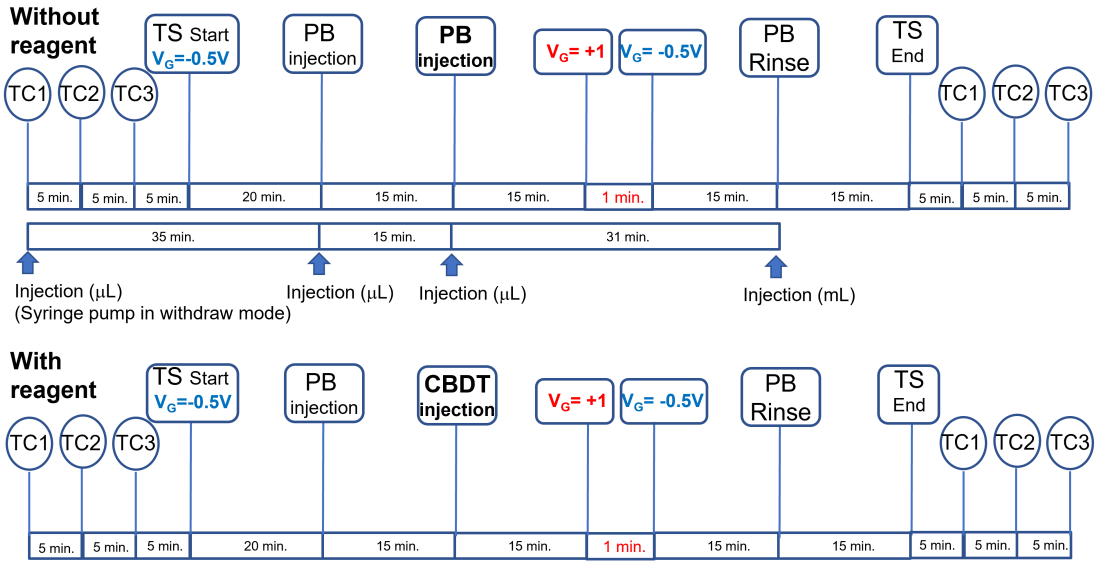

Figure B.15 – Timeline for gate-switch experiments with the PXI setup (control on top, experiment on the bottom). TC stands for transfer curve, TS stands for time series.

Experiments related to Fig. 3b-c were executed following this protocol. The GFET chip was loaded in the chip holder, with the PDMS flow cell secured on top. PB buffer (pH = 8.0) was injected with the syringe pump so as to fill the flow cell. The control experiment in absence of reagent was performed before the experiment in presence of reagent, and both were carried out on the same day. First, three transfer curves were acquired, with a 5 minutes stabilization time in between. After 5 minutes stabilization time, the time series was started with the gate voltage at -0.5V ($\Delta V_{G-CNP} < 0$, OFF state) and V_{SD}=0.05 V. After 20 minutes stabilization, a first PB injection was done to assess its effect on the time series, followed by 15 min wait time. Then, either a second dose of PB buffer was injected (control) or a dose of 10 mM CBDT in PB was injected (experiment). The same volume was used for both cases. After 15 minutes of stabilization, the gate voltage was switched to +1V ($\Delta V_{G-CNP} > 0$, ON state) for 1 min to activate the reaction, after which the gate voltage was changed back to -0.5V to turn off the reaction. After 15 min wait time, the flow cell was purged with 3 mL of PB buffer, and after another 15 minutes the time series was stopped. After 5 minutes, three transfer curves were taken with 5 minutes in between. The I_{CNP} values before and after the TS were extracted from the transfer curves as described in Fig. S3.

B.16. Experimental protocol for gate-activated/rinse-quenching experiments

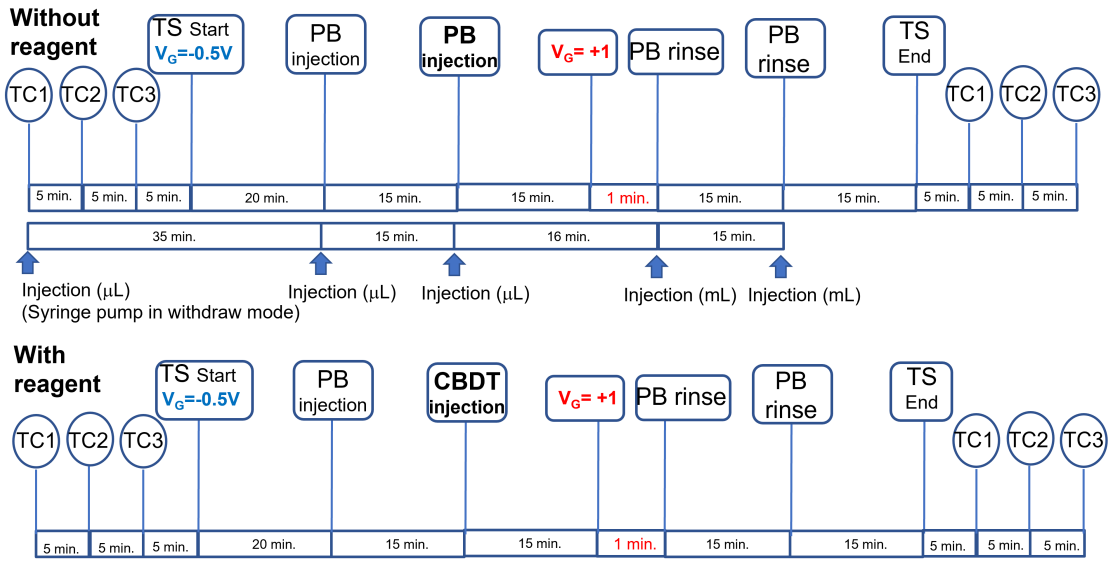

Figure B.16 – Timeline for gate activation and rinse quenching experiments with the PXI setup (control on top, experiment on the bottom). TC stands for transfer curve, TS stands for time series.

This is a similar experiment as in Fig. S15, but replacing the gate-mediated quenching step by rinsing with clean buffer. All steps were exactly the same until after the gate voltage was switched to +1 V ($\Delta V_{G-CNP} > 0$, ON state) for 1 min, in buffer for the control or in 10 mM CBDT for the experiment. At the end of the 1 min incubation, the gate voltage was left as is, and the flow cell was immediately purged with 3 mL of PB buffer in order to stop the reaction by removing the reagent. After 15 min wait time, another 3 mL of PB buffer was injected and, after another 15 min wait time, the time series was stopped. Transfer curves and resulting I_{CNP} values were then obtained as described in Fig. S3.

B.17. Gate-activated/rinse-quenching experiment results

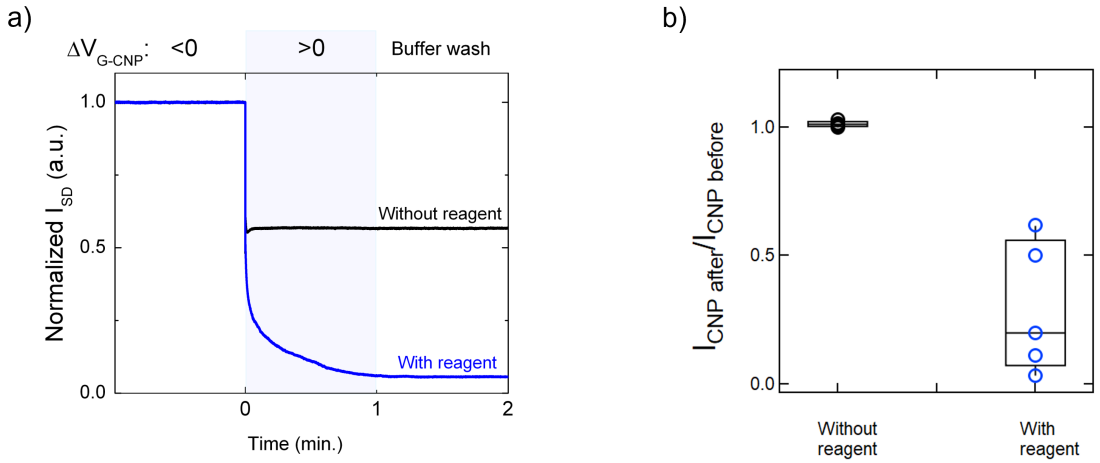

Figure B.17 – (a) Time series of an individual GFET while immersed in the reactant (blue curve). The gate voltage is switched from an OFF-value ($\Delta V_{G-CNP} < 0$) to an ON-value ($\Delta V_{G-CNP} > 0$) to enable the reaction during 1 min. The flow cell is then purged with buffer solution to stop the reaction while keeping the gate voltage ON. The black curve is a control done previously on the same device while immersed in buffer only. (b) Change in conductance for several devices after the gate-activated/rinse-quenching experiment (blue) and its control in buffer (black).

The effect of removing the diazonium aryl radicals by using extensive washing with saline buffer solution is tested with real-time measurements (see protocol in Fig. S16). The black curve is the control experiment always in buffer only, and the blue curve is collected in presence of the CBDT reagent. As in Fig. 3b, when the gate voltage is switched ON ($\Delta V_{G-CNP} > 0$), the conductance decreases in the control due to the change in density of charge carriers in the graphene, and it decreases more in the experiment because the formation of covalent adducts is activated. After 1 min, the flow cell is purged using clean buffer. In the control, the conductance remains the same since the gate voltage also remains the same. In the experiment, the conductance stops decreasing and stabilizes in a plateau, indicating that the removal of the reagent stops the formation of defects on the graphene surface. The current ratios (after buffer washing / before gate activation) for several devices are presented in panel b. Controls remain identical (no change), while devices exposed to CBDT report a decreased conductance, to (29±25)% of the initial value on average.

B.18. Experimental protocol for gate-switch experiments at different reaction times

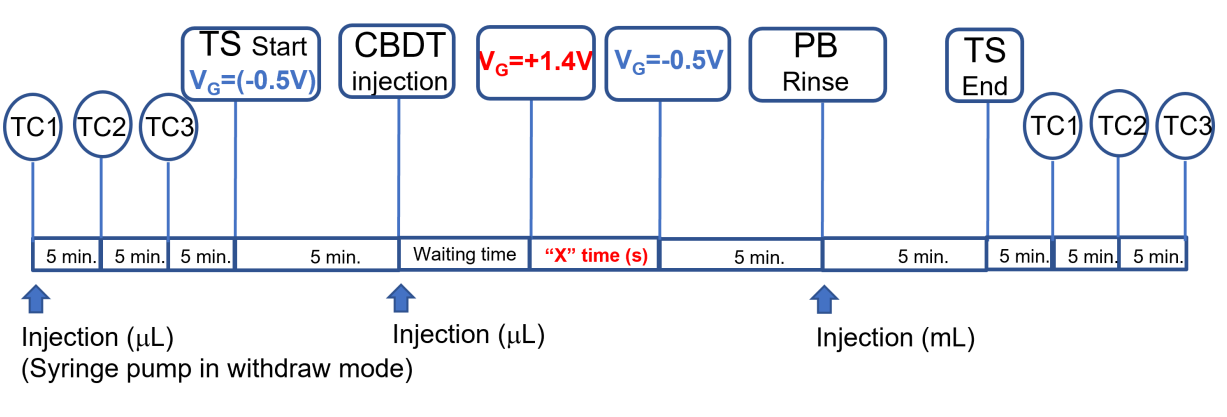

Figure B.18 – Timeline for gate-switch experiments at different reaction times with the PXI setup. TC stands for transfer curve ; TS stands for time series.

Experiments related to Fig. 3d-e were performed following this protocol. The GFET chip was loaded in the chip holder, with the PDMS flow cell secured on top. PB buffer (pH = 8.0) was injected with the syringe pump to fill the flow cell. First, three transfer curves were acquired, with a 5 minutes stabilization time in between. After 5 minutes of stabilization, the time series was started with the gate voltage at -0.5V and V_{SD}=0.05V. After 5 minutes stabilization, a dose of 10 mM CBDT in PB was injected, followed by a waiting time of 5 minutes, for the first experiment, or 5 minutes + the accumulated "X" reaction time for the following experiments (e.g., 5min. 5s. ; 5min. 15s., etc.). The "X" time is added to the waiting time to compensate for the spontaneous degradation of the CBDT reagent in solution. Then, the gate voltage was switched to +1.4V for "X" seconds to activate the reaction (reaction times used were "X"= 5, 10 ,10, 10, 20, 30 and 30 seconds, so that the total reaction time was 115 seconds), after which the gate voltage was changed back to -0.5V to turn off the reaction. After 5 minutes, the flow cell was purged with 3 mL of PB buffer, and after another 5 minutes the time series was stopped. Finally, after 5 minutes, three transfer curves were acquired with 5 minutes in between.

B.19. Raman spectra of various functionalization strategies

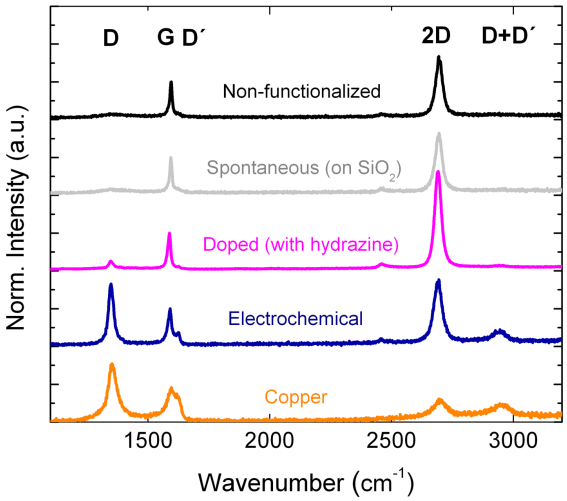

Figure B.19 – Raman spectra of graphene on Si/SiO_2 after functionalization in various conditions : non-functionalized graphene for reference (black), spontaneously functionalized graphene (gray), graphene functionalized after chemical doping with hydrazine (pink), electrochemically-driven functionalization (blue) and graphene functionalized on copper before transfer on Si/SiO_2 (orange).

Raman spectra of bare graphene (black), spontaneous functionalization on $SiSiO_2$ (grey), and three doping strategies on the functionalization reaction : (1) chemical doping with hydrazine (pink), (2) electrochemical doping using cyclic voltammetry (blue), and (3) substrate-based doping on copper (orange). All three experiments were conducted on CVD-grown graphene surfaces using a solution of BBDT (see Section S1.5 for more details about functionalization and Section S1.6 for details about Raman). For chemical doping, graphene transferred on Si/SiO_2 was immersed in a solution of hydrazine, an electron-donating molecule n-doping graphene [298, 299], prior to the BBDT solution. For electrochemical doping, we used cyclic voltammetry in a three-electrode electrochemical cell, with graphene as the working electrode, using the voltage to modulate the charge carrier density in graphene [255, 300]. For the substrate-based strategy, functionalization was executed immediately after graphene growth, while the graphene was still on copper to provide an electron reservoir [301]. The graphene was then transferred on Si/SiO_2 for Raman characterization. Overall, we observe increasingly important defect-induced peaks with increasingly effective methods (from the top-down).

B.20. Raman I_D/I_G ratios after functionalization on copper as a function of incubation time and reagent concentration

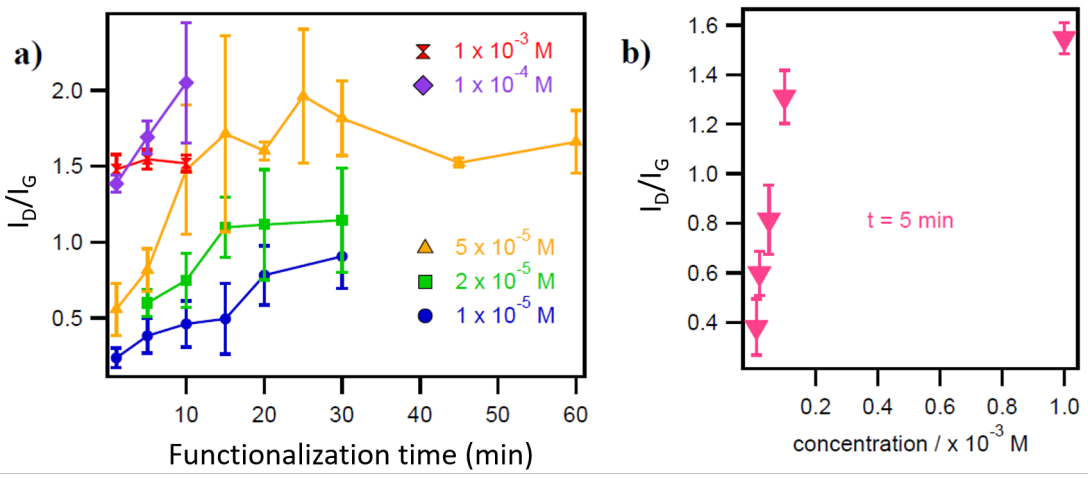

Figure B.20 – a) Integrated D/G ratio of Raman bands as a function of the functionalization time with BBDT on copper, at different concentrations. b) Integrated D/G ratio of Raman bands as a function of BBDT concentration after 5 minutes of incubation on copper.

The integrated D/G ratios were extracted from the Raman spectra taken from graphene after incubation in different concentrations of BBDT and after incubation times. For all concentrations from 1×10^{-4} M of BBDT and above, the D/G ratio increases with time until 20 minutes of reaction. From this time point, the behaviour mostly stabilizes, indicating that the reaction is likely completed. In the second panel, we see for 5-min incubations, the quantity of defect increases with the concentration of BBDT until a plateau at 1×10^{-3} M. Overall, this data shows that defect density increases both with time and concentration, confirming that functionalization occurs as expected.

B.21. Raman spectra after electrochemical functionalization with different aryldiazonium reagents

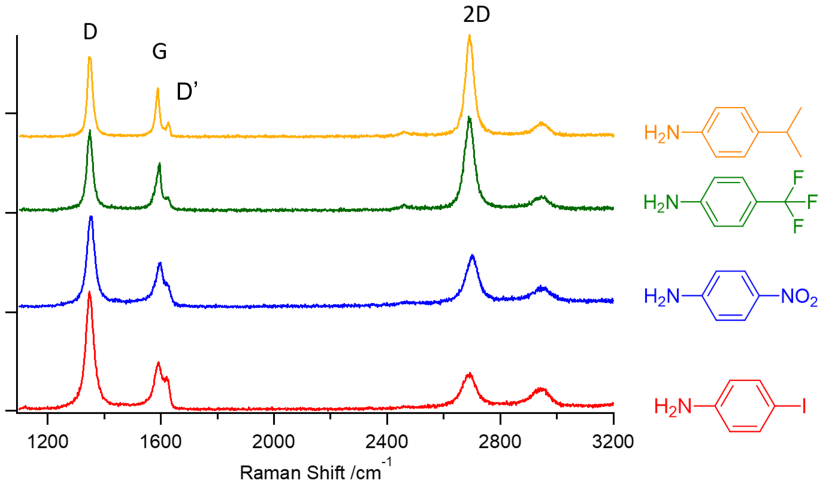

Figure B.21 – Raman characterization after functionalization with aryldiazonium reagents generated from iodianiline (red curve), nitroaniline (blue curve), trifluoroaniline (green curve), and isopropylaniline (yellow curve).

Electrochemical functionalization was repeated using the same method as with BBDT, with four different aryldiazonium reagents. The spectra all show the same disorder-induced bands (D and D'), coherent with the covalent modification of graphene surface. This indicates that functionalization with the electrochemical doping method and its Raman signature is not limited to BBDT, but is general to any aryl radicals.

B.22. Raman results after spontaneous functionalization

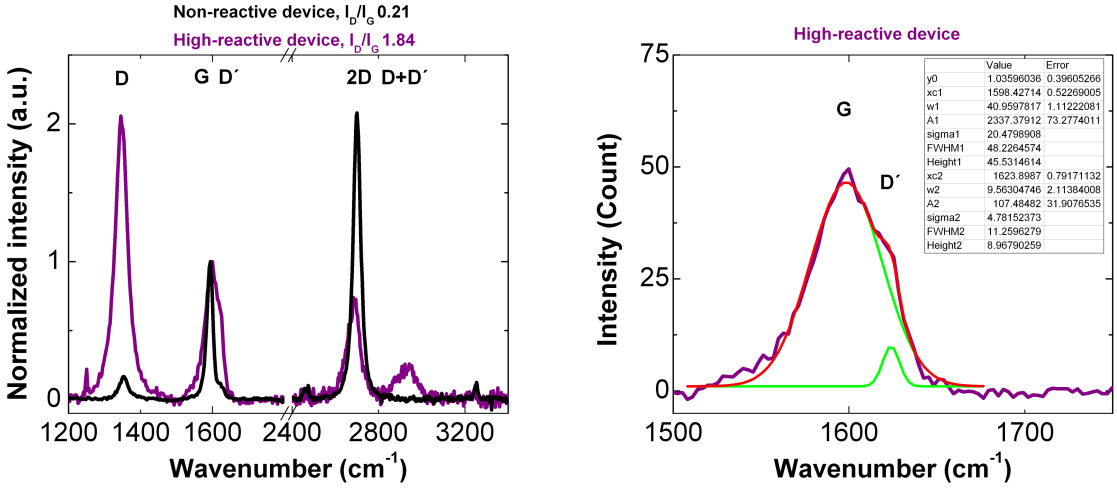

Figure B.22 – (a) Raman results after spontaneous functionalization for a non-reactive and a high-reactive devices, (b) Representative example of the deconvolution of G and D' bands for the high-reactive device.

Raman spectroscopy was acquired after 24h incubation in CBDT solution for two representative devices with different degrees of functionalization (Fig. 1c) : a non-reactive device, black line, and a high-reactive device, purple line. We observe a strong increase in the defect-related D, D' and D+D' bands due to the creation of sp^3 defects in the graphene lattice. These bands are much more pronounced for the high-reactive device, indicating a higher level of functionalization, which agrees with the electrical characteristics of the devices after the spontaneous reaction (Fig. 1c). From the raw spectra, we performed background removal, baseline correction and deconvolution of the G and D' bands. A representative example of the latter is shown for the high-reactive device in panel b. The integrated intensity ratios of Raman bands D and G (I_D/I_G) were calculated from parameters extracted from the best fit of the Raman spectra using Gaussian or Lorentzian line shape analysis.